

Development and Applications of Eutectic Liquids



By

Mark William Gilmore, BSc

Presented to the School of Chemistry and Chemical Engineering

The Queen's University of Belfast

in fulfilment of the requirements for the degree of

Doctor of Philosophy

The Queen's University of Belfast

May 2019

Acknowledgements

I would like to extend my sincerest gratitude to the many people who have helped me along the way both in the lab and writing this thesis. The undertaking of a PhD is not a journey you can take on your own and for the valuable inputs from everyone I am very grateful.

I wish to thank my supervisors Gosia Swadźba-Kwaśny and John Holbrey, their excellent knowledge of the field of ionic liquids, their creativity, their friendship and mentoring have been a key factor in why I have been able to reach the end of this PhD. I have learnt so much from them and I am definitely a more well-rounded chemist as a result of their input.

For their valuable contributions and advice on aspects of my work I want to express my gratitude to Eadaoin McCourt and Peter Nockemann.

I would like to thank those friends I have made during my time working in QUB; Lucy, Leila, Emily, Gareth, Keith, Eoghain, Sophie, Marty, Natasha, Oli and Jeni. Not only for the help you have given to me in the lab but for the laughs we have had along the way.

Without funding this PhD would not have been possible and for that I am very thankful to QUILL for providing me with this, and especially to the IAB members who have also imparted invaluable ideas and constructive criticisms throughout my study.

The work of the administrative and technical staff both in QUILL and ASEP is also very deserving of a mention. I am indebted to the efforts of Deborah, Angela, Darren, Donal, Richard and Suzi for all of their assistance.

Finally, I wish to thank my family; to my wife Deárbhla, you encouraged me to start this venture and have supported me from the 1st day to the last, I am very appreciative for all that you do for me. To my Mum, Dad and Brother I want to thank you for the love and support you have given me throughout my life, this has equipped me to be confident in all life decisions that I make.

Abstract

The initial motivation behind this work was inspired by the reports on metal oxide dissolution by deep eutectic solvents. The original aim was to understand the underpinning mechanism of dissolution and, building on this, to derive improved systems for metal recovery from waste streams.

Review of the literature led to a re-examination of thermal properties of the archetypical system of choline chloride:urea, focusing on careful moisture control. The key outcomes, reported in Chapter 2, include an updated phase diagram and conclusive proof that the eutectic composition is thermally unstable even at relatively low temperature of 90 °C. This is consistent with recent literature reports suggesting that oxide dissolution mechanism relies on decomposition products, rather than on the inherent properties of the eutectic mixture.

In parallel, choline chloride:urea and choline chloride:oxalic acid deep eutectic solvents were studied by neutron scattering (Chapter 3), to elucidate the difference in hydrogen bonding between an amide and a carboxylic acid at 338 K. In either case, the -OH group on the choline chloride was found to have less prominent influence on the overall hydrogen bonding within the system, than previously suggested, indicating that the structure of the cholinium cation is not pivotal in the design of deep eutectic solvents. The chapter is concluded with multi-technique studies on zinc oxide speciation in deep eutectic solvents, with the aim to elucidate the dissolution mechanism. Two plausible mechanisms are proposed, but unfortunately these studies remained inconclusive.

Studies described in Chapters 2 and 3 led to the conclusion that the components of the archetypical deep eutectic system, choline chloride and urea, are neither uniquely suited for metal oxide dissolution, nor particularly inclined to form deep eutectic solvents, which motivated the search for alternatives (Chapter 4). Seeking a more thermally stable alternative to urea, with improved affinity to metals, several approaches were investigated, combining choline chloride with various hydrogen bond donors: imidazole (*N*-donor), thioureas (*S*-donors) and various carboxylic acids. However, the most interesting systems given their low viscosity and hydrophobic nature were prepared by completely abandoning choline chloride, and moving onto a non-ionic hydrogen bond acceptor, trioctylphosphine oxide (TOPO).

An in-depth study into the first TOPO-based eutectics is presented in Chapter 5, which combines a physical chemistry investigation into the TOPO-phenol system and preliminary studies into its applications for extraction of uranyl from aqueous media.

Table of contents

1.	Introduction	1
1.1	Eutectics.....	1
1.1.1	Etymology, history and definition	1
1.1.2	Traditional areas of applications for eutectics	3
1.1.3	Ionic liquids and renewed interest in low-melting salts	6
1.1.4	Molecular components in ionic liquids.....	12
1.1.5	Deep eutectic solvents	16
1.2	Physical properties of DESs	21
1.2.1	Melting point	21
1.2.2	Viscosity	23
1.3	Applications of DESs	24
1.3.1	Gas and volatile organic compounds (VOCs) absorption	24
1.3.2	DES as organic reaction medium	25
1.3.3	Nanoparticles	27
1.3.4	Natural product separation.....	28
1.3.5	Dissolution and separation of metals	29
1.3.6	Electrochemistry in DES	31
1.4	Motivation for this work.....	33
2	Choline chloride:Urea DES	34
2.1	Introduction	34
2.2	Experimental.....	37
2.2.1	Materials and methods.....	37
2.2.2	Preparation of ChCl:Ur mixtures.....	37
2.2.3	Water content analysis	37
2.2.4	Solid-liquid phase transitions analysis	38
2.2.5	Thermal stability analysis	39
2.3	Results and discussion	39
2.3.1	Sample preparation and water content analysis.....	39
2.3.2	Phase diagram.....	41
2.3.3	Physical properties.....	45
2.3.4	Thermal stability	48

2.4	Conclusions	50
3	Neutron diffraction determination of intermolecular structure from the ChCl:Ur and Chcl:oxalic acid liquid systems at 338 K	52
3.1	Introduction	52
3.2	Experimental.....	53
3.3	Results and discussion	58
3.3.1	Structure of ChCl:Ur DES	61
3.3.2	Structure of ChCl:Ox DES	65
3.3.3	Spatial density functions.....	67
3.3.4	Validation of EPSR reference potential.....	70
3.4	Conclusions for neat ChCl:Ur/ ChCl:Ox DESs.....	70
3.5	ChCl:Ox with dissolved metal oxides	71
3.5.1	Experimental.....	72
3.5.2	Results and discussion	77
4	Screening Study of Des	90
4.1	ChCl:imidazole	90
4.2	DES containing thioureas	92
4.3	ChCl: carboxylic acid DES.....	100
4.4	TOPO DES	102
5	Hydrophobic DES.....	105
5.1	Current hydrophobic DES	105
5.2	Background.....	105
5.3	Experimental.....	107
5.3.1	Chemicals and methods	107
5.3.2	NMR spectroscopy	107
5.3.3	Density and viscosity	108
5.3.4	Water content.....	108
5.3.5	TOPO/Phenol Solid–Liquid Phase Diagram.....	108
5.3.6	Phenol and TOPO Leaching to Aqueous in l/l Mixtures.....	109
5.3.7	Liquid–Liquid Extraction of Uranyl ([UO ₂] ²⁺) Ions from Aqueous Acid with TOPO: Phenol Eutectic Liquids	109
5.4	Results and discussion	110
5.4.1	Thermal Stability	111
5.4.2	Melting Point and Phase Composition	112
5.4.3	Density and Viscosity.....	117

5.4.4	Miscibility of TOPO:phenol ($\chi_{\text{TOPO}} = 0.50$) with Water.....	120
5.4.5	Liquid–Liquid Extraction Studies	121
5.4.6	Sustainability	124
5.5	Conclusions	125
6	Summary and conclusions	127
7	Bibliography	129
8	Appendix 1	143
8.1	Engineering wastes	143
8.1.1	Red mud.....	143
8.1.2	Coal fly ash.....	143
8.2	Scanning electron microscopy for PFA and red mud samples	144
8.3	Treatment of engineering wastes using DES.....	145
9	Appendix 2	148

List of Figures

Figure 1.1-1 Ideal phase diagram for a binary eutectic mixture.....	2
Figure 1.1-2: Gallium-indium phase diagram showing a eutectic point at 15.7 °C, the left ordinate represents pure gallium with the percentage of indium being increased until the right ordinate is reached, determined by Esten and Elliot, ²³ . Reproduced from ref 23.....	4
Figure 1.1-3: The heptachlorodialuminate salt “red oil” the first ionic liquid described in literature.....	8
Figure 1.1-4: Phase diagram of aluminium chloride-ethyl pyridinium bromide by Hurley and Weir. ⁵¹	9
Figure 1.1-5: The ionic liquid systems of Parshall and Knifton, <i>Ionic liquids in synthesis</i> , eds. Wasserscheid and Welton ³⁷	10
Figure 1.1-6: The main equilibria of LCCs, determined by spectroscopic studies for the key compositions and compared to the equilibria of chlorometallate ionic liquids; M = Al ³⁺ or Ga ³⁺	11
Figure 1.1-7: Walden plot classification diagram for ionic liquids. ³⁹	14
Figure 1.1-8: Choline chloride with hydrogen bond donors Ur, ethylene glycol and malonic acid.....	16
Figure 1.1-9: Number of papers published on deep eutectic solvents per year (Web of Science, date accessed:07/02/2019) ¹²¹	17
Figure 1.3-1: Formation of bisamides from aldehydes and ChCl:Ur DES ¹²³	26
Figure 1.3-2: Synthesis of Z vinyl-selenocyanate using DES ¹⁶⁸	27
Figure 1.3-3: SEM images of star-shaped Au nanoparticles produced in ChCl:Ur DES. ¹⁷³ ..	28
Figure 1.3-4: Reflected light optical microscopy image of electrum before and after reaction with $\chi_{\text{ChCl}} = 0.33$ ChCl:ethylene glycol. ¹⁰⁶	32
Figure 2.3-1: Ur crystals deposited on the neck of the flask after overnight drying at 80 °C, under reduced pressure	40
Figure 2.3-2: Fragments of DSC scans (heating) recorded for: $\chi_{\text{ChCl}} = 0.33$ at 0.1 °C min ⁻¹ (—), 1.0 °C min ⁻¹ (—) and 5 °C min ⁻¹ (—). Scans displayed as exotherm down.	42
Figure 2.3-3: Phase diagram of ChCl:Ur, accompanied by POM images of the $\chi_{\text{ChCl}} = 0.67$ sample, captured at 25, 35 and 80 °C.	44
Figure 2.3-4: Powder XRD patterns, recorded as a function of temperature, for $\chi_{\text{ChCl}} = 0.67$, temperatures 25 °C (—), 65 °C (—) and 95 °C (—) are shown.....	45

Figure 2.3-5: Comparison of density data recorded for the ChCl:Ur eutectic ($\chi_{\text{ChCl}} = 0.33$) as a function of temperature in this work (■), by Abbott <i>et al.</i> (▲), ¹¹⁵ Pandey and Yadav (■), ²⁰⁷ Xie <i>et al.</i> (▲) ²⁰⁸ Shah <i>et al.</i> (▲) ¹⁵⁸ and Su <i>et al.</i> (■). ¹⁵⁷	47
Figure 2.3-6: Literature comparison of \ln viscosity as a function of temperature for the $\chi_{\text{ChCl}} = 0.33$ ChCl:Ur DES, This publication, ■, Abbott <i>et al.</i> , ¹¹⁵ ■, Pandey and Yadav, ²⁰⁷ ■, Xie <i>et al.</i> ²⁰⁸ ■.	48
Figure 2.3-7: Dynamic TGA and DTG curves, recorded at 5 °C min ⁻¹ for two samples of ChCl:Ur, $\chi_{\text{ChCl}} = 0.33$ (-), and $\chi_{\text{ChCl}} = 0.67$ (-), and derived mass loss for $\chi_{\text{ChCl}} = 0.33$ (---) and $\chi_{\text{ChCl}} = 0.67$ (---).	49
Figure 2.3-8: Isothermal TGA curves, recorded at 90 °C for two samples of ChCl:Ur, $\chi_{\text{ChCl}} = 0.33$ (—), and 0.67 (—).	50
Figure 3.2-1: Infra-red spectrum for oxalic acid-H ₂ (—), oxalic acid-D ₂ (pre-drying, —) and oxalic acid-D ₂ (post-drying, —).	54
Figure 3.2-2: Atom types assigned to the choline, Ur, and oxalic acid molecules used in the EPSR simulation of diffraction data.	56
Figure 3.3-1: Structure factors for ChCl:Ur (top) and ChCl:Ox (bottom). For each DES, experimental (symbols) and EPSR modelled (solid) total structure factors (left) and transformations to real space (right) for the isotopically substituted liquid mixtures are shown. Residual differences between the experimental and simulated data are shown by the dashed lines. The curves have been shifted for clarity and are labelled with the isotopic composition of the ChCl:HBD components.	59
Figure 3.3-2: Centre of mass RDFs for ChCl:Ur (top) and ChCl:Ox (bottom).	60
Figure 3.3-3: Atom-centred pRDFs for ChCl:Ur	62
Figure 3.3-4: Atom-centred pRDFs for ChCl:Ox.....	63
Figure 3.3-5: SHARM spatial probability maps for ChCl:Ur (top) and ChCl:Ox (bottom) showing the distributions around choline in the two systems (left) and Ur (top right) or oxalic acid (bottom right) of choline (yellow), chloride (green), and Ur or oxalic acid (cyan) calculated to encompass the first shell peaks from the COM RDFs in Figure 3.3-2. Surfaces were calculated to encompass the top 15% probability within the first peak in the COM RDF around the central molecule.....	68
Figure 3.3-6: Schematic of the most favourable oxalic acid dimer hydrogen- bonding motif (after reference ²³⁸) with two inter-molecular hydrogen-bonds (red) and three intra-molecular hydrogen-bonds (blue) that generate the characteristic pattern in the oxalic acid–oxalic acid SDF.	69
Figure 3.5-1: Stick and ball models of choline (left) and oxalic acid (right)	72
Figure 3.5-2: Ball and stick model of tetrahedral chlorozincate (left) and di(oxalato)zincate (right) anion.	74

Figure 3.5-3: Chlorozincate simulation with 450 components in a 38.85 Å box.....	74
Figure 3.5-4: Oxalatozincate simulation box with 600 components in a 40.70 Å.	76
Figure 3.5-5: Raman spectra of ChCl:Ox (red) and ChCl:Ox with dissolved ZnO (black) ...	79
Figure 3.5-6: S(Q) neutron scattering profiles from ChCl-oxalic acid DES containing dissolved ZnO (Top) and the corresponding transformation of S(Q) scattering into <i>d</i> -space (Angstrom) from ChCl-oxalic acid DES containing dissolved ZnO showing the absence of Bragg diffraction peaks that would signify the presence of crystalline solid particles.	80
Figure 3.5-7: Plot of refinement energy as a function of iteration number for the chlorozincate EPSR model, showing the stability of the equilibrated simulation (top) Corresponding plot of chlorozincate simulation model internal pressure (bottom).	82
Figure 3.5-8: Comparison of F(Q) scattering correlations between the normalised model (dashed lines) and experimental data (solid lines) for the chlorozincate model of the ChCl:Ox + ZnO DES, showing the relatively good fit to the two data sets with the model: .	83
Figure 3.5-9: Comparison of f(r) distance correlations between the normalised model (dashed lines) and experimental data (solid lines) for the chlorozincate model of the ChCl:Ox + ZnO DES, showing a reasonable correlation of the model with the experimental data.....	83
Figure 3.5-10: Centre of Mass (COM) radial distribution functions (average species separations) between choline cations and chlorozincate anions in the EPSR model, showing the first shell choline-zincate (cation-anion) and choline-oxalate (cation-anion) associations at 4.8 Å. These are followed by second shell choline-choline (cation-cation) correlation at 6-7 Å. The zincate anions show a large, defined correlation centred at 8 Å, indicating that this model for the DES has a strong structural correlation.....	84
Figure 3.5-11: Simulation internal energy (top) and pressure plots (bottom).	85
Figure 3.5-12: Comparison of F(Q) scattering correlations between the normalised model and experimental data for the di(oxalato)zincate model, showing the relatively good fit to the two data sets with the model.....	86
Figure 3.5-13: Comparison of f(r) distance correlations between the normalised model and experimental data for bisoxalatozincate model, showing a reasonable correlation of the model with the experimental data.....	87
Figure 3.5-14: Centre of Mass (COM) radial distribution functions (average species separations) between choline cations and oxalatozincate anions in the EPSR model.....	87
Figure 3.5-15: S(Q) scattering from ChCl/oxalic acid DES with dissolved Fe ₃ O ₄ , for the protiated DES (blue) and the deuteriated DES (red).	89
Figure 3.5-16: FT of scattering data into d-space (Å) from ChCl/oxalic acid DES with dissolved Fe ₃ O ₄ . No evidence of diffraction peaks from Fe ₃ O ₄ nanoparticles are evident in the data.....	89

Figure 4.1-1: Phase diagram showing molar fraction of choline chloride (χ_{ChCl}) relative to thermal event temperature ($^{\circ}\text{C}$) for the ChCl:Im system. Thermal event 1 (■) occurs between 45-60 $^{\circ}\text{C}$ and thermal event 2 (■) at approximately 80 $^{\circ}\text{C}$	92
Figure 4.2-1: Chemical structure of studied molecules top left to bottom right: urea, 1,3 dimethylurea, tetramethylurea, thiourea, 1,3 dimethylthiourea and tetramethylurea.....	93
Figure 4.2-2: DSC thermogram for 1:2 ChCl:thiourea.....	93
Figure 4.2-3: DSC thermogram for 1:2 ChCl:DMT.....	95
Figure 4.2-4: phase diagram for ChCl: 1,3 dimethylurea mixtures constructed using pom....	98
Figure 4.2-5: Phase diagram for ChCl:Tu constructed using POM.....	99
Figure 4.4-1: Formation of TOPO:phenol DES	102
Figure 5.2-1: Phenol (left) and TOPO (right).....	107
Figure 5.4-1: The appearance of TOPO:phenol mixtures of different compositions at ambient temperature (left to right $\chi_{\text{TOPO}} = 0.1-0.9$).....	110
Figure 5.4-2: Mass loss profiles under dynamic TGA conditions for phenol (red), TOPO (blue) and TOPO:phenol ($\chi_{\text{TOPO}} = 0.50$, green) heating at 5 $^{\circ}\text{C min}^{-1}$, showing the increased thermal stability (reduced loss of phenol) in the DES compared to neat phenol.	112
Figure 5.4-3: DES second cooling and heating profiles for TOPO:phenol mixtures offset from the baseline by their corresponding compositions (χ_{TOPO}).....	113
Figure 5.4-4: Phase diagram for TOPO:phenol mixture, constructed from observational solidification points (solid-liquid cell, ■), DSC results (■), and solid-liquid cell glass transitions (□).....	115
Figure 5.4-5: ^{31}P NMR spectra of TOPO:phenol liquids (left) and the corresponding chemical shift plotted as a function of liquid composition (right). Chemical shifts ₂₈₂ for TOPO in CDCl_3 (43.66 ppm) and in C_6D_6 (48.48 ppm) are shown at $\chi_{\text{TOPO}} = 1$ (blue squares) for comparison.....	116
Figure 5.4-6: Density of TOPO:phenol liquids at $\chi_{\text{TOPO}} = 0.33$ (blue ○) and 0.50 (red □) showing the linear change in density with temperature, fitted as a function of temperature to $y = 1.1342 - 0.000\ 680\ 67x$ ($\chi_{\text{TOPO}} = 0.33$) and $y = 1.1075 - 0.000\ 673\ 19x$ ($\chi_{\text{TOPO}} = 0.50$). Density of the TOPO:phenol mixtures decreases with increasing TOPO content.	118
Figure 5.4-7: Viscosity of the TOPO:phenol liquids at $\chi_{\text{TOPO}} = 0.33$ (blue) and 0.50 (red) plotted as a function of temperature. Data at $\chi_{\text{TOPO}} = 0.33$ was fitted to the Vogel-Fulcher-Tammann (VFT) equation, $\eta = A \times e^{(B/T-T_0)}$, where η is viscosity (mPa s), T is temperature (K), and T_0 is the ideal glass transition temperature (K) with parameters of $\ln(A) = -5.234$, $B = 435$, and $T_0 = 209\text{ K}$ ($r_2 = 0.994\ 568$).	119
Figure 5.4-8: Transmission spectra (top) from the uranyl feed solution (250 ppm $[\text{UO}_2]_{2+}$) containing Br-PADAP indicator (blue) and the raffinate after contact with TOPO:phenol	

(red). Standard solutions containing 5–50 ppm uranyl in nitric acid are shown as dashed lines for comparison. 122

Figure 5.4-9: UV–vis spectra for 0.05 M uranyl nitrate solutions in 0.30 M TOPO/cyclohexane (black) and $\chi_{\text{TOPO}} = 0.5$ TOPO:phenol (red)..... 124

Figure 8.2-1: SEM image of red mud (left) and PFA (right) 144

Figure 8.2-2: Scanning electron microscopy image of pulverised fly ash (left) and red mud (right) after treatment with 1:2 choline chloride:Ur. 145

List of Tables

Table 1.1-1: Melting points (°C) and thermochemical radii of the anions (Å) for Na ⁺ and [C ₂ mim] ⁺ salts ³⁷	7
Table 1.1-2: General formula for DESs classification proposed by Abbott and co-workers ¹²⁷	19
Table 1.3-1: Vapour–liquid partition coefficients (K) of toluene, acetaldehyde and dichloromethane in water and in seven different solvents at 30 and 60 °C. ¹⁶⁴	25
Table 1.3-2 Metal oxide results from Abbott ¹⁷⁹	31
Table 2.2-1: Molar fraction and masses of ChCl and Ur added to produce samples.	37
Table 2.3-1: Water content and appearance at ambient conditions of ChCl:Ur samples	41
Table 2.3-2: Melting points of ChCl:Ur samples, derived from POM experiments	43
Table 2.3-3: Viscosities and densities of the ChCl:Ur eutectic ($\chi_{\text{ChCl}} = 0.33$) as a function of temperature.	46
Table 2.3-4: TGA analyses of two samples of ChCl: Ur DES: $\chi_{\text{ChCl}} = 0.33$ and 0.67	49
Table 3.2-1: Melting points determined by DSC for isotopomerically substituted ChCl:Ox mixtures.	55
Table 3.2-2: Initial Lennard-Jones (ϵ and σ) and charge (q) parameters used for the reference potential of the Empirical Potential Structure Refinement model for both systems derived from the literature, and OPLS-AA.....	56
Table 3.2-3: Intramolecular bond distance (Å) and bond-angle (°) constraints used to define the basic structure of the components in the initial EPSR simulation model. Oxalic acid was fixed to a planar conformation by defining O-C-C-O dihedral restraints.	57
Table 3.3-1: Position of the first peak in the centre of mass RDFs for 3. Results from Ref. ¹³⁷ for ChCl:Ur are shown in parentheses.....	61
Table 3.3-2: Coordination numbers calculated for the principle partial RDFs shown in Figure 3.3-3 and Figure 3.3-4 for ChCl:Ur (1:2) and ChCl:Ox 1:1 DES. Mean coordination numbers Ncoord were determined to the first minima (rmin) after the primary correlation peak (rmax) in the pRDF	64
Table 3.5-1: Experimental sample compositions, densities and scattering cross sections	73
Table 3.5-2: : Lennard-Jones (ϵ and σ) and charge (q) parameters used for the reference potential of the Empirical Potential Structure Refinement model for both plausible ZnO speciation modes derived from the literature, and OPLS-AA.....	75
Table 3.5-3: Intramolecular bond distance (Å) and bond-angle (°) constraints used to define the basic structure of the components in the initial EPSR simulation model for the ChCl:Ox	

Des with dissolved ZnO. Oxalic acid was fixed to a planar conformation by defining O-C-C-O dihedral restraints.....	75
Table 3.5-4: Starting potential parameters for bisoxalatozincate anion for EPSR refinement	77
Table 3.5-5: Geometry definitions for bisoxalatozincate anion	77
Table 4.2-1: HBD ureas/thioureas with associated melting point °C for the pure components (left) and eutectic formation comment and melting point when in a 1:2 ChCl:HBD mixture (right).	96
Table 4.2-2: T_g for mixtures of ChCl:1,3-dimethylthiourea	98
Table 4.3-1: The pKa values and eutectic formation for a range of carboxylic acids with ChCl. All pKa values taken from “Data compiled by R.Williams”. ²⁴⁸	101
Table 4.4-1: TOPO:carboxylic acid screen, All pKa values taken from “Data compiled by R.Williams”. ²⁴⁸	103
Table 5.4-1: Thermal data from DSC and observation. Temperatures were measured from the peak positions of the first order transitions in the DSC second heating cycle, and the enthalpy of melting determined from integration of the peak.	114
Table 5.4-2: ^{31}P NMR Chemical Shifts (δ ^{31}P /ppm) for TOPO: Phenol Liquids as a Function of Composition (χ_{TOPO})	117
Table 5.4-3: Density and Viscosity of TOPO: Phenol Mixtures at $\chi_{\text{TOPO}} = 0.33$ and 0.50	119
Table 5.4-4: Concentration of Phenol _a Leached to Aqueous Acid after Contacting with an Equal Volume of the TOPO: Phenol Eutectic ($\chi_{\text{TOPO}} = 0.5$) at 25 °C.....	120
Table 5.4-5: Performance of TOPO:phenol ($\chi_{\text{TOPO}} = 0.50$) as a liquid extractant for uranyl nitrate from nitric acid at different acid and uranyl concentration in the aqueous feed.	123
Table 8.3-1: showing the relative % difference in amount of each metal present in the sample with respect to Al between the pulverised fly ash sample and the post treatment 1:2 ChCl Ur sample. % dissolved for each element present in the PFA sample.....	146

Abbreviations

[2-C1Py][citrate] – 2 methylpyridinium citrate	NMR – nuclear magnetic resonance
[C3-mpyr][Ntf2] – N-methyl-N-propylpyrrolidinium bistriflimide	OPLS-AA – optimized potentials for liquid simulations- all atom
Br-PADAP - 2-(5-bromo-2-pyridylazo)-5-(diethylamino)phenol	Ox – oxalic acid
ChCl – choline chloride	p-XRD – powder x-ray diffraction
COM – centre of mass	PFA – pulverized fly ash
DCS – differential cross section	POM – polarized optical microscopy
DES – deep eutectic solvent	PPM – parts per million
DFT – density functional theory	pRDFs – partial radial distribution functions
DMSO – dimethylsulfoxide	QENS – Quasi elastic neutron scattering
DMT – 1,3 dimethylthiourea	RDF – radial distribution function
DSC – differential scanning calorimetry	SDF – spatial density function
DTG – derivative thermogravimetric analysis	S-donor – sulfur donor
EAF – electric arc furnace	SEM – scanning electron microscopy
EPSR – empirical potential structural refinement	TBABR – tetrabutylammonium bromide
ESI – Electrospray ionization	TBPBR – tetrabutylphosphonium bromide
FAB – fast atom bombardment	Tg – glass transition temperature
FT – Fourier transform	TGA – thermogravimetric analysis
GC-MS – gas chromatography-mass spectrometry analysis	THF – tetrahydrofuran
HBA – hydrogen bond acceptor	Tm – melting temperature
HBD – hydrogen bond donor	TOMAC – tri-n-octylmethylammonium chloride
HSAB – hard soft acid base theory	TOP – trioctylphosphine
IL – ionic liquid	TOPO- trioctylphosphine oxide

IM – imidazole

Tu – thiourea

INS – inelastic neutron spectroscopy

Ur – urea

LCC – liquid coordination complex

UV-vis – ultraviolet-visible

LTMS – low transition temperature mixtures

VFT – Vogel-Fulcher-Tammann

Mal – malonic acid

VOC – volatile organic content

N-donor – nitrogen donor

Publications arising from this work

- 1) M. Gilmore, L. M. Moura, A. H. Turner, M. Swadźba-Kwaśny, S. K. Callear, J. A. McCune, O. A. Scherman and J. D. Holbrey, *J. Chem. Phys.*, 2018, **148**, 193823.
- 2) M. Gilmore, E. N. McCourt, F. Connolly, P. Nockemann and J. D. Holbrey, *ACS Sus. Chem. Eng.*, 2018, **6**, 17323.
- 3) L. C. Brown, J. M. Hogg, M. Gilmore, L. Moura, S. Imberti, S. Gartner, H. Q. N. Gunaratne, R. J O'Donnell, N. Artioli, J. D. Holbrey and M. Swadźba-Kwaśny, *Chem. Comm.*, 2018, **54**, 8657.
- 4) Y. M. Delavoux, M. Gilmore, M. P. Atkins, M. Swadzba-Kwasny and J. D. Holbrey, *Phys. Chem. Chem. Phys.*, 2017, **19**, 2867.
- 5) L.Moura, M.Gilmore, S. K. Callear, T. G. A. Youngs and J.D Holbrey, *Mol Phys*, 2019, doi.org/10.1080/00268976.2019.1649495.
- 6) M. Gilmore, J.D Holbrey and M. Swadźba-Kwaśny, *J Chem. Eng. Data*, submitted May 2019.

1. INTRODUCTION

The chapter describes the history of studies on eutectic liquid systems, the several types of eutectics that have been described throughout the scientific and engineering fields, and discusses eutectic mixtures in the context of ionic liquids and deep eutectic solvents (DESs), which were the main inspiration for the work described in this thesis.

1.1 Eutectics

1.1.1 Etymology, history and definition

The word “eutectic” stems from the Greek words $\epsilon\mu$ and $\tau\acute{\eta}\zeta\iota\varsigma$ meaning “easy melting”. This description gives insight into all eutectic mixtures regardless of the species involved, as they all share the common physical feature of having a depressed melting point when compared to their starting components. The term was coined by the British chemist Frederick Guthrie in 1884,¹ in his memoirs “On *Eutexia*” where he describes a eutectic as “*for bodies made up of two or more constituents, which the constituents are in such proportion to one another as to give to the resultant compound body a minimum temperature of liquification - that is, a lower temperature of liquification than that given by any other proportion*”.

The best tool to understand the definition given by Guthrie is a phase diagram, which provides a schematic to describe the interaction between the two or more components as a function of composition, through changes in phases of resulting mixtures. For an ideal binary eutectic system (Figure 1.1-1), A and B represent pure components, whereas values C that lie in between represent mixtures of A and B at different molar fractions. T_a and T_b represent the melting point of the pure components, the lines coming from T_a and T_b represent the liquidus point of each molar fraction.

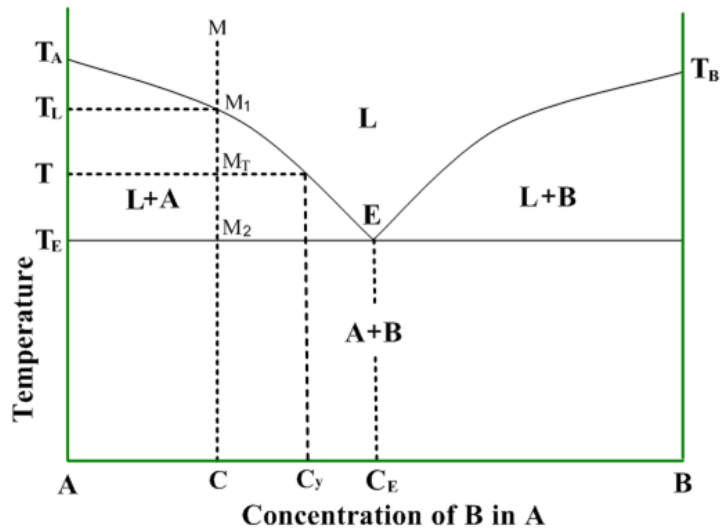


Figure 1.1-1 Ideal phase diagram for a binary eutectic mixture

In this simple phase diagram, the melting points are at their highest point for the pure components and gradually decrease following the solidus/liquidus boundary line towards a liquidus minimum (E). Above the liquidus line each mixture is completely liquefied (L); E represents the eutectic point as it is the minimum melting point across the compositional range of A and B. A horizontal eutectic line (T_E) marks the temperature above which there is partial liquification of the mixture (liquid + solid A, or liquid + solid B), with the exception of pure A (solid), pure B (solid) and E the eutectic point (liquid). M values represent the different melting points of the different phases within the mixtures. Below the eutectic line the mixtures are solid.

Eutectics had practical applications even at the time of Guthrie. One of the first well-known examples is the eutectic formed between water and NaCl; when combined in the specific ratio ($\chi_{\text{NaCl}} = 0.09$, 23.3 wt%), a depression in the melting point occurs, from 0 °C for pure water to -21.12 °C at the eutectic point.² This is due to the formation of a hydrogen bonding network between water (the hydrogen bond donating species in the system), and the chloride, which is the hydrogen bond acceptor. This physical feature is exploited when de-icing roads as the addition of NaCl lowers the melting point of the water, inhibiting ice formation.

The definition given by Guthrie has stood for over a century, and is still valid today, with numerous eutectic mixtures known and implemented for practical uses, exemplified in Section 1.1.2.

1.1.2 Traditional areas of applications for eutectics

1.1.2.1 Pharmaceuticals

Examples of eutectics can be found within the pharmaceutical field where the formation of eutectic systems with enhanced properties plays a key role in overcoming various challenges.³ For example, studies into the transdermal drug delivery of ibuprofen found that the flux (J , $\mu\text{g cm}^{-2} \text{h}^{-1}$) of ibuprofen delivered was significantly increased when applied as a $\chi_{\text{ibuprofen}} = 0.4$ eutectic with thymol, ($T_m = 32^\circ\text{C}$). Thymol was found to have a synergistic effect by liquefying the ibuprofen whilst increasing its transdermal flux. It was found to be approximately 13 times higher than a saturated aqueous solution of ibuprofen and 7 times greater than the same solution, but applied to skin pre-treated with thymol.⁴ Another example is diferuloylmethane, the active ingredient in turmeric, which is of potential pharmaceutical importance due to its anti-inflammatory and anticancer properties,⁶ in addition to stemming off the onset of Alzheimer's disease.⁷ Despite these benefits, it has failed to be widely utilised due to poor aqueous solubility and oral bio-availability. However, when mixed with nicotinamide ($\chi_{\text{diferuloylmethane}} = 0.33$) the resulting eutectic was found to have a ten-fold increase in the intrinsic dissolution rate and a six-fold in the area under curve measurement (an indicator of the bioavailability of a drug comparing to crystalline diferuloylmethane).⁸ The final example presented here is phytoestrogen hormone genistein, which can be found in plants, fruits and wholegrains. It is a biologically active tyrosine inhibitor, and is therefore reported to be an anti-inflammatory, antimicrobial and anticarcinogenic compound.^{9–12} Again, despite vast research, the hydrophobic nature of genistein leads to it having poor aqueous solubility ($3 \cdot 10^{-6} \text{ mol L}^{-1}$),¹³ rendering it unsuitable for the parenteral route of administration and therefore restricting its pharmaceutical benefits. It has been shown that genistein will form a eutectic with PEG 460 with a temperature depression of approximately 60°C , to 0.2°C therefore liquifying the genistein at room temperature which allows for formulation to be developed and administered by injection allowing the pharmaceutical benefits of the drug to be obtained.¹³

1.1.2.2 Alloys

Alloys can be divided into two classes: eutectic and non-eutectic. In a non-eutectic alloy, components have different solidification points upon cooling from a fully liquid state. Eutectic alloys, which have a single solidification point for the system, are superior in certain aspects, and have had commercial importance for centuries.¹⁴ For example, in dentistry, eutectic alloys for metal-ceramic restorations have been found to be highly effective at

minimising the effects of tooth decay,¹⁵ a good example being 83:17 wt% eutectic palladium-gallium alloy ($T_m = 1000\text{ }^{\circ}\text{C}$), which is then spiked with copper, raising the eutectic temperature, resulting in increased strength and hardening of the alloy.¹⁶

Room temperature liquid metals, although known since antiquity, became of great interest during the late 1940s and '50s, as the ideal coolants for early nuclear reactors. They had high thermal conductivities¹⁷ and mercury boilers were already successfully incorporated into industrial processes.¹⁸ However, mercury is the only metal that is a room temperature liquid in its elemental state ($T_m -39\text{ }^{\circ}\text{C}$), which fuelled attempts to produce low-melting metal alloys.¹⁹ The formation of a eutectic between two or more metals, is an ideal strategy to produce liquid metals; by varying the composition other properties can be altered, such as thermal conductivity and electrical resistivity.²⁰ Metals with near-room temperature melting points include francium ($T_m 30.0\text{ }^{\circ}\text{C}$),²¹ caesium ($T_m 28.4\text{ }^{\circ}\text{C}$) and gallium ($T_m 29.8\text{ }^{\circ}\text{C}$),²² however the reactivity of Group 1 alkali metals prohibits them from being useful heat transfer fluids. Consequently, efforts focused on the liquification of gallium given its comparative stability. A popular binary eutectic alloy comprises of gallium in a concentration of 76 wt%, indium 24 wt%, the resulting mixtures are reported to have a wide liquid range from 15 to 1800 $^{\circ}\text{C}$,²³ which represents a depression in melting point of approximately 15 $^{\circ}\text{C}$ from elemental gallium, most importantly making the mixture a room temperature liquid (Figure 1.1-2).

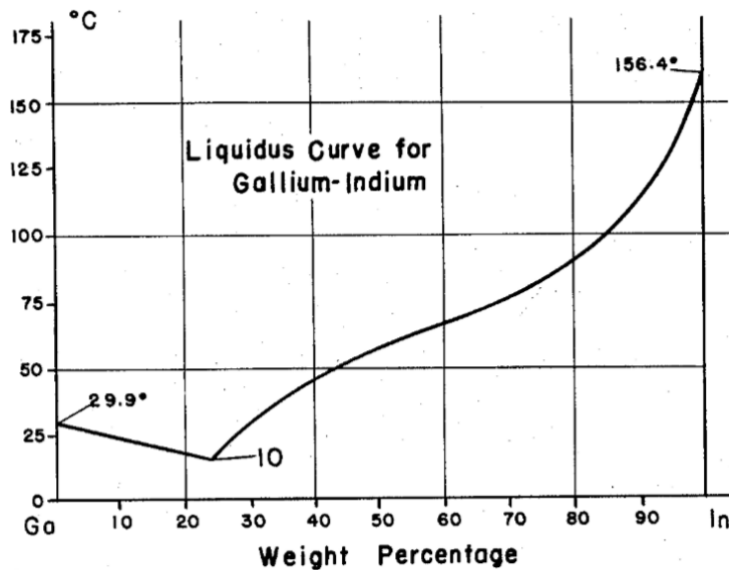


Figure 1.1-2: Gallium-indium phase diagram showing a eutectic point at 15.7 °C, the left ordinate represents pure gallium with the percentage of indium being increased until the right ordinate is reached, determined by Esten and Elliot,²³. Reproduced from ref 23.

The addition of 0-10 wt% of tin to form a ternary eutectic causes a further decrease in the melting point temperature of the mixture to -15 °C, trace amounts of antimony can be added to improve oxidative resistance and bismuth, to increase fluidity of the mixture.²⁰ A commercial form of the **gallium, indium, and tin (stanium)** ternary eutectic Galinstan®, produced by and registered to Geratherm Medical AG, has been explored as an alternative to the toxic liquid metal mercury in microdevices as it is non-toxic and has exceptionally low vapor pressure (<10⁻⁶ Pa at 500 °C).²⁴ Galinstan® has already been incorporated into microelectromechanical systems successfully with a microrelays,²⁵ patch antennas²⁶ and microvalves²⁷ having been developed. Whilst Galinstan® is a promising liquid metal, a major drawback is that it undergoes oxidation in a normal atmosphere, resulting in the solidification of the liquid therefore current use is limited to an inert atmosphere or a sealed system.²⁴

Given that eutectic alloys have a defined *solidus/liquidus* point, they are valuable in soldering processes for electronics, as the solder will undergo even melting and solidification ensuring a good electrical connection. It is advantageous to have solders in a homogenised state when applied onto an electrical circuit, as this ensures a good electrical connection: a eutectic alloy is ideal for this purpose, having a single melting point. The common eutectic alloy used as a solder for electronics during the last century was a tin-lead based solder (T_m 183 °C) due to it having a low melting point, excellent wettability and improved ductility.²⁸

However, with lead's well known toxicity, legislation has been introduced within the EU to phase out the use of solders with high lead content, with exception only given for military and extra-terrestrial purposes.²⁹ In the late 90s, Lee³⁰ set out a number of criteria such as low toxicity, a narrow plastic range and good fatigue resistance, which should be met for any newly developed solders. Replacement solders have been developed and used in new electronic systems, although they have several shortcomings including reliability, fatigue and drop resistance still exist.³¹ The near-eutectic Sn-Ag-Cu SAC alloy appears to be the most promising replacement for Sn-Pb, with similar physical properties to its predecessor. Unfortunately, the use of silver in SAC drives up its price, and cheaper alternatives are required for non-surface mount technology application, such as eutectic Sn-0.7Cu, popular due to its high availability and low price.³² These examples show that the physical phenomena of eutectic formation between metals have been key for designing the original Sn-Pb solder systems and will be crucial for developing new Pb-free solders.³³

1.1.3 Ionic liquids and renewed interest in low-melting salts

Ionic liquids are defined as salts with melting temperatures below 100 °C,^{34,35} although this is an arbitrary value, and there are many systems that melt slightly higher that are incredibly useful. Whilst “ionic liquids” is now the accepted nomenclature, in the 20th century a wider range of terminologies were used as descriptors for such systems, including non-aqueous ionic liquid, molten salt, liquid organic salt, and fused salt (to name a few)³⁶ - all these definitions describing the same class of low melting salts, with the focus on studying their molten state. Salts that are molten at room temperature, aptly known as room temperature ionic liquids, are of special interest. In some cases, they can directly replace common organic solvents, whilst having the advantage of low vapour pressures, making them virtually non-flammable and more containable (less likely to enter the environment as vapours).

Why are ionic liquids liquid (at relatively low temperatures)? Conceptually, the simplest cases are ionic liquids that are organic salts, with well-defined cation and anion. Parameters that govern the lattice energy of an ionic crystal as defined in the Kaputinskii equation are (i) the product of the net ion charges, (ii) ion-ion separation, and (iii) packing efficiency of the ions.³⁷ To produce a low melting ionic system, net charges on ions should be kept low (preferably ± 1) and the ion-ion separation should be high, hence the ions should be large and unsymmetrical (to disrupt organised packing). Table 1.1-1 exemplifies that increasing the atomic radius of an anion results in a depression in melting point of the corresponding sodium salts, due to weakened Coulombic interactions in the crystal lattice; comparing

sodium chloride to sodium tetrachloroaluminate(III), a melting point depression of over 600 °C is recorded as a result of increasing the atomic radius of the anions. A similar effect is observed also when altering a cation, which is why lithium salts tend to have a higher melting points than their corresponding sodium or potassium salts. Comparing the melting point data for the Na⁺ and [C₂mim]⁺ (1-ethyl-3-methylimidazolium) salts in Table 1.1-1, we observe that replacing a small cation like sodium (charged localised on the single atom) with a large unsymmetrical cation like [C₂mim]⁺ (charge delocalised around the aromatic ring) causes the melting point to decrease from 801 to 87 °C for the corresponding chloride salts. These principles form the basis of designing room temperature ionic liquids from single cation-anion combinations, without necessarily resorting to eutectic strategies.

Table 1.1-1: Melting points (°C) and thermochemical radii of the anions (Å) for Na⁺ and [C₂mim]⁺ salts³⁷

X ⁻	R (Å)	Melting point	
		NaX	[C ₂ mim]X
Cl ⁻	1.7	801	87
[BF ₄] ⁻	2.2	384	6
[PF ₆] ⁻	2.4	>200	60
[AlCl ₄] ⁻	2.8	185	7

It is important to note that the speciation of many ionic liquid systems is more complicated than that of [C₂mim][NTf₂]. Long-known protic ionic liquids are in dynamic equilibria with their neutral conjugate acids and bases,^{38,39,40} in consequence comprising both ionic and molecular species, which makes them complex mixtures. Halometallate ionic liquids are prepared by combining two components: metal halide and an organic halide salt,⁴¹ which may exhibit a eutectic behaviour at certain molar fractions; as a matter of fact, this strategy had been used to access low melting temperatures in chlorometallate molten salts (early ionic liquids).^{42,43} Recently developed liquid Lewis acids; liquid coordination complexes and borenium ionic liquids, all are characterised by complex equilibria, which in many cases involve charge-neutral species. Finally, through 4th evolution of ionic liquids, MacFarlane and co-workers⁴⁴ postulate that the definition of ionic liquid should be expanded to complex mixtures of ionic liquids doped with molecular solvents, but retaining some core physico-chemical properties of ionic liquids. Deep eutectic solvents (DESs) stem from this “mixture design” strategy in ionic liquids; most DESs are made up of organic salts combined with organic non-ionic compound such as amides, alcohols and acids, which was intended to improve their physical properties for certain applications, delivering “next generation” of ionic liquid-like materials.⁴⁵ However, the distinction between ionic liquids and deep eutectic solvents is anything but clear; rather, they are a part of continuum of functional liquid materials. The following sections are an attempt to trace the history of selected “complex mixtures” in the realm of ionic liquids, and subsequently to frame our current understanding of DESs against this backdrop.

1.1.3.1 Halometallate ionic liquids

The first documented observation of a chlorometallate ionic liquid was in the 19th century where chemists noted the formation of a red oil as a by-product of the Friedel-Crafts process,

however it was not until the invention of NMR spectroscopy in the 20th century that the red oil was determined to be a heptachlorodialuminate salt (Figure 1.1-3).⁴⁶

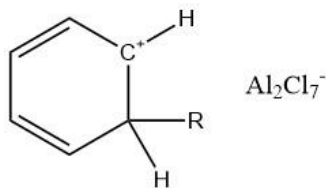


Figure 1.1-3: The heptachlorodialuminate salt “red oil” the first ionic liquid described in literature.

The first ionic liquid mentioned in the literature was, unknowingly to himself, reported in 1887 by Ramsey.⁴⁷ He commented that, when 2-methylpyridine was reacted with citric acid, an uncrystallisable syrup formed. What he was observing was the formation of the first (protic) ionic liquid, [2-C₁py][citrate] *via* proton transfer. He subsequently went on to win the 1904 Nobel prize in chemistry for the discovery of Noble gases and their position on the periodic table, however if understood at the time this would have been another significant discovery accredited to Ramsey. The first room temperature molten salt, to be actually designed and identified as such, was ethyl ammonium nitrate with a melting point of 12 °C reported by Walden⁴⁸⁻⁵⁰ in 1914 for use as a solvent in electrochemistry. However, it took several more decades for these solvents to emerge from scattered reports and curiosities to the mainstream of chemistry. The birth year of modern ionic liquid chemistry is probably 1951, when Hurley and Weir presented a Lewis acidic halogenoaluminate forming a room temperature liquid that could be used for the electrodeposition of metals.⁵¹ Comprising of aluminium (III) chloride (AlCl₃) with 1-ethylpyridinium bromide ([C₂py]Br), phase analysis of the mixtures yielded two eutectic points at $\chi_{\text{AlCl}_3} = 0.33$ and 0.67. The $\chi_{\text{AlCl}_3} = 0.67$ mixture was found to have a melting point of -40 °C, however this composition represented the only mixture to form a room temperature liquid.³⁶ This represents a depression in melting point from the two pure components AlCl₃ ($T_m = 190$ °C)⁵² and [C₂py]Br ($T_m = 120$ °C) of over 150 °C.

The phase diagram of [C₂py]Br with AlCl₃, shown in Figure 1.1-4, contains two eutectic depressions at $\chi_{\text{AlCl}_3} = 0.33$ and 0.67 and a congruent point at $\chi_{\text{AlCl}_3} = 0.50$, which the authors ascribed to the formation of a new compound, [C₂py][AlCl₃Br].

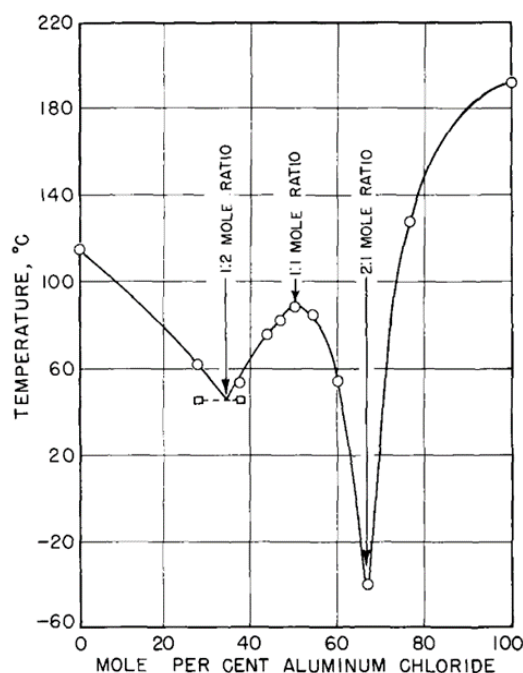
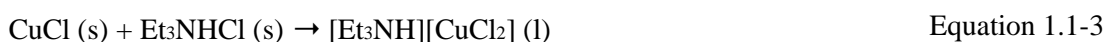


Figure 1.1-4: Phase diagram of aluminium chloride-ethyl pyridinium bromide by Hurley and Weir.⁵¹

Following on from this original work, different components were added to AlCl₃ to increase the liquid range of the mixtures, driven by a demand for new battery electrolytes. Seeking for liquids that were conductive and did not require a pre-heating step,⁴⁹ gave rise to the *N*-butylpyridinium chloroaluminate^{53,54} and 1-ethyl-3-methylimidazolium chloroaluminate⁵⁵ systems, which were the archetypal ionic liquids systems at the end of the 20th century.^{36,56} Speciation of the systems has been extensively studied,⁵⁷ showing that the species present is dependent on the molar fraction of the AlCl₃ present and that Columbic and hydrogen bonding interactions dominate the liquid structure.



The same history could be told from another perspective. As early as 1962, Yoke had reported that mixtures of CuCl with triethylammonium was forming near to room temperature chlorocuprate liquids (Equation 1.1-3).⁵⁸



Parshall used tetraethylammonium chloride salts combined with GeCl₃, and SnCl₃ earlier proposed by Jones⁵⁹ as a solvent for the homogenous catalysis of olefins (Figure 1.1-5).⁶⁰

Realising that these molten salts had the high thermal stability required for the reaction, olefins had high solubility in these solvents and probably most importantly could be easily separated from the organic final product, Parshall took advantage of these solvent properties for carrying out his catalysed olefin conversions. A sentence that should not be overlooked in his 1972 publication is “*An approach that seems to have been under-utilized is the use of molten salts as stable, non-volatile solvents*” As Parshall alluded to, certainly one of the underused and greatest features of ionic liquids are their low vapor pressures allowing in a practical sense for ease of separation of more volatile compounds and from a green perspective making the solvents more containable and less likely to leach into the atmosphere. Parshall may not have fully comprehended the magnitude and potential reach of the statement he made, when one considers how popular ionic liquids later became, but it does give insight to the thinking at the time that the potential of these solvents was beginning to be realised.

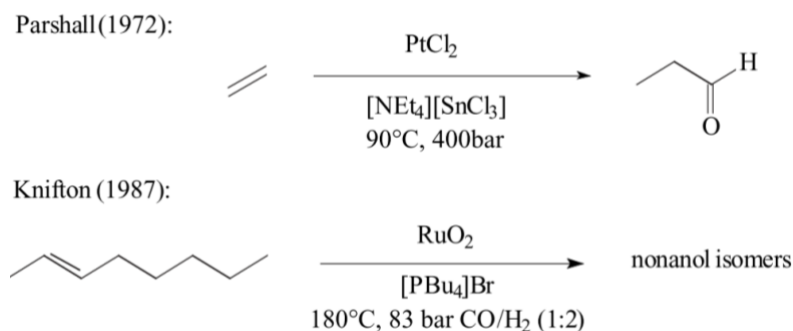


Figure 1.1-5: The ionic liquid systems of Parshall and Knifton, *Ionic liquids in synthesis*, eds. Wasserscheid and Welton³⁷

In 1987 Knifton published a paper on the oxonation of internal olefins using a RuO_2 catalyst in a $[\text{PBU}_4]\text{Br}$ (Figure 1.1-5) an ionic liquid by today's definition, providing an early example of an ionic liquid phosphonium salt.⁶¹ He noted that the quaternary phosphonium salt matrix, $[\text{PBU}_4]\text{Br}$, stabilised the ruthenium carbonyl catalyst.

Despite insights demonstrated by Yoke, Parshall and Knifton amongst others, it was the research on chloroaluminate ionic liquids that reached the critical mass and attracted the attention of a wider scientific community. Nevertheless, despite their increasing popularity, working with chloroaluminate ionic liquids was not without its challenges. They are highly sensitive to moisture requiring preparation in Schlenk or inert (glovebox) conditions, which is not surprising given that their main starting component is AlCl_3 - a strong Lewis acid, which upon contact with water forms the hexahydrate $\text{Al}(\text{H}_2\text{O})_6\text{Cl}_3$, which when heated produces $\text{Al}(\text{OH})_3$ releasing 3 molar equivalents of HCl and water.⁶² On the wave of interest

in chloroaluminate chemistry, studies on other metallate systems gained renewed attention. Ionic liquids containing other Group 13 metals InCl_3 ^{63–65} and GaCl_3 ^{66–69} were synthesised and their speciation studied. The former were moisture stable, but only weakly acidic, the latter were strong acids, but very prone to hydrolysis. Chlorozincate systems, with very complicated speciation of doubly-charged chlorozincate anions, were relatively inexpensive and moderately Lewis acidic, but had very high viscosity due to double charge on all anionic species.⁷⁰ A search for more industry-friendly alternative led to the incorporation of molecular organic compounds into ionic liquids.

Combining ionic components with molecular to gain more favourable properties, liquid coordination complexes (LCCs) were developed.⁷¹ By incorporating a strategy to suppress the melting points similar to that employed for ionic liquids,^{72,73} Swadźba-Kwaśny and co-workers combined the neat metal salts GaCl_3 or AlCl_3 with sub-stoichiometric amounts of the donor molecules including *O*-donors (Ur, acetamide, TOPO), an *S*-donor (thiourea) and a *P*-donor trioctylphosphine (TOP) to form room temperature liquids, they found the key liquids compositions to have a molar fraction of $\chi_{\text{MCl}_3} = 0.5\text{--}0.67$, the group were able to determine that the LCCs speciation showing that the systems were in dynamic equilibrium and were influenced by stoichiometry as shown in the schematic below (Figure 1.1-6). The group then went on to demonstrate applications using LCCs,^{74–77} including LCCs as catalysts for the synthesis of polysilpholefins⁷⁶ and the Friedel-Crafts alkylation of benzene.⁷⁷

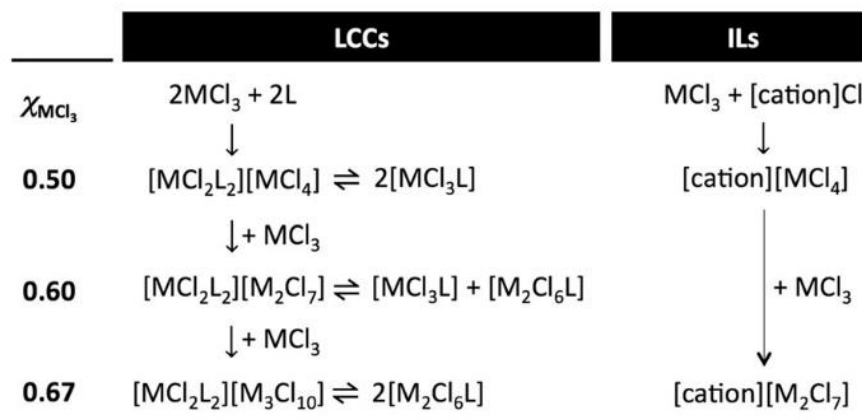
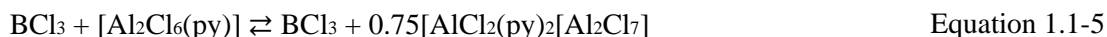


Figure 1.1-6: The main equilibria of LCCs, determined by spectroscopic studies for the key compositions and compared to the equilibria of chlorometallate ionic liquids; $\text{M} = \text{Al}^{3+}$ or Ga^{3+}

The same group published another class of ionic liquids with molecular components based on combinations of tetracoordinate boron adducts $[\text{BX}_3\text{L}]$ with an excess of an abstracting agent as shown in Equation 1.1-5 and Equation 1.1-6.⁷⁸ The systems are extremely Lewis

acidic recording some of the highest acceptor numbers for Lewis acids to date. The systems have been applied for the Diels-Alder cycloaddition of cyclopentadiene to ethyl acrylate.⁷⁹



It should be noted, that LCCs were preceded by decades of research into ‘accidentally’ liquid coordination complexes. The group of Atwood were developing unusual salt based liquids called “liquid clathrates”.^{80,81} They combined salts with aluminium alkyl giving the ionic formula $\text{M}[\text{Al}_2\text{R}_6\text{X}]$ (M= alkali metal or a tetra-alkylammonium cation; R = Me, Et, Prⁿ, Buⁿ, X = halide, N₃⁻, SCN⁻),⁸² then combined this with aromatic compounds to form $\text{M}[\text{Al}_2\text{R}_6\text{X}] \cdot \text{Aromatic}$, with the anion from the salt forming an Al-X-Al bridging anion with the alkylaluminium, then an inclusion compound forms with an aromatic guest.^{81,82} In 2011, Abood *et al.* described liquid mixtures composed of AlCl_3 and amides, including acetamide and *N,N*-dimethylUr,⁸³ they postulated that the ionic liquids $[\text{AlCl}_2(n\text{Amide})][\text{AlCl}_4]$ (n=1 or 2) were forming. However, these systems are more accurately described as LCCs where the AlCl_3 is heterolytically cleaved by the amide.⁸⁴ An example of speciation in LCCs is described in detail in Figure 1.1-6.

1.1.4 Molecular components in ionic liquids

According to the classical definition of ionic liquids must have a glass transition or melting temperature of less 100 °C and, importantly, should be formed solely of ions, with purities of 99% or greater⁸⁵ to be considered a true ionic liquid. However, there is a prominent class of ionic liquids that falls short of this definition: **protic ionic liquids formed via proton transfer**. They often contain both ions and molecular components, which does not make them less interesting or valuable. For example, Greaves *et al.* conducted a detailed physico-chemical properties study of 25 protic ionic liquids, emphasising that, although they are “poor” ionicity, they have promising properties in terms of future applications.⁸⁶ The same group authored authoritative reviews of the area.⁸⁷

Protic ionic liquids⁸⁷ were one of the first systems to challenge the classical ionic liquid definition.⁸⁵ The first known recording of a protic ionic liquids were by Ramsey in 1887⁴⁷ and Gabriel and Werner in 1888.⁸⁸ These are ionic liquids formed by proton transfer from a Brønsted acid to a Brønsted base.⁸⁶ Similarly to halometallate ionic liquids,⁴¹ they have been

studied across a compositional range. A general formula for the formation of a stoichiometric protic ionic liquids is set out in Equation 1.1-6.



The equation represents the charge-neutral Brønsted base (B) and Brønsted acid (A) reacting to form the conjugate acid and base hence forming the ionic liquid, such as $[CH_3NH_3][HCOO]$.⁸⁷ However, these systems are not classed as “pure” ionic liquids due to the reaction equilibrium: for strong Brønsted acids and bases these are likely to dissociate completely forming a fully ionic system (meeting the criteria for a fully ionised ionic liquid). However, a weak acid and/or weak base will only partially dissociate, producing a liquid with partly molecular character, of lower ionicity. Therefore, the community that studies ionic liquid by proton transfer have taken a more flexible approach, postulating that ionic liquids have a *degree* of ionicity, which can vary significantly between different ionic liquids depending on their structure.⁸⁹ Angell and co-workers developed a qualitative method for comparing the ionicity of ionic liquids called a Walden plot.^{39,90,91} They developed a method derived from the Walden rule (Equation 1.1-7):

$$\Lambda\eta = k \quad \text{Equation 1.1-7}$$

Where Λ is the molar conductivity ($S\ cm^2\ mol^{-1}$), η is the viscosity ($Poise^{-1}$) and k is a temperature-dependent constant. The Walden rule was originally developed from observing dilute aqueous solutions of salts, but was found to be applicable to non-aqueous electrolytes⁹² and molten salts.⁹³ Plotting $\log \Lambda$ vs. $\log \eta$, the Walden rule predicts a straight line through the origin, this is now known as a “Walden plot”.

Figure 1.1-7 shows a Walden plot with regions of the plot annotated with the type of ionic liquid expected to be found in that region. 0.1 M KCl is often used as a calibration solution,³⁹ it allows for estimation of k and forms the reference line on the plot.

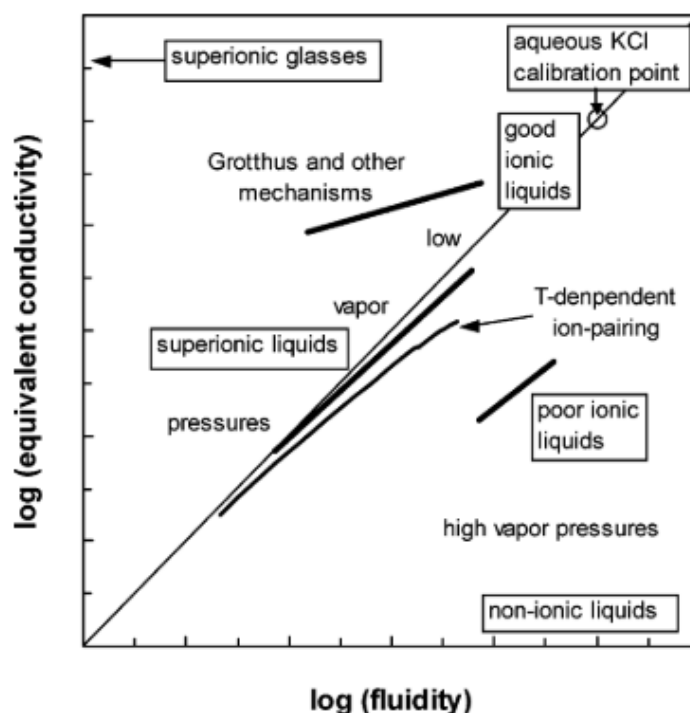


Figure 1.1-7: Walden plot classification diagram for ionic liquids.³⁹

Generally, ionic liquids have poorer ionicities than 0.1 M KCl, so called “good” ionic liquids will lie close too but below the 0.1M KCl reference line. Protic ionic liquids tend to lie well below the reference line,^{39,94} classed as “poor” ionic liquids due to incomplete proton transfer between their constituent acid and base.

There were a number of attempts in trying to predict what acid-base combination would make a “good” ionic liquid. Angell and co-workers postulated the required pK_a difference between the acid and the base must be at least 10.⁹⁵ More complexity was added to this picture by MacFarlane and co-workers, who demonstrated that ionicity, and the degree of proton transfer, depend on acid:base stoichiometric ratio and on hydrogen bonding ability of both components, delivering highly ionic systems with pK_a differences as low as 4.^{96,97} On the other hand, an interesting picture of a liquid that is molecular rather than ionic came out of neutron scattering studies of pyridine and acetic by McCune *et al.*, probed as a function of acid:base ratio.⁹⁸ Using a “free proton” empirical structural refinement (EPSR) model, they revealed the existence of hydrogen-bonded acetic acid chains with free pyridine inclusions, rather than the formation of an ionic liquid by proton transfer, even with significant excess of acid.

Another iteration of molecular components included in ionic liquids are systems, typically used as electrolytes, where an organic molecule is added in small amount to otherwise fully ionic liquid, retaining most of its properties, but alleviating some issues, such as high viscosity. The deliberate doping of an ionic liquid with molecular components results in the reduction in both conductivity and viscosity of an ionic liquid, hence the liquid would be shifted closer towards the bottom right quadrant of the Walden plot. MacFarlane *et al.* have heralded this incorporation of molecular components into ionic liquids as the **4th evolution of ionic liquids**.⁴⁴ One such system they describe is the doping of *N*-methyl-*N*-propylpyrrolidinium *bis*(trifluoro-methylsulfonyl)amide, [C₃mpyr][NTf₂], with the coordinating and non-coordinating solvents toluene and THF for electrochemistry.⁹⁹ The addition of these molecular solvents led to the enhancement of the conductivity of the [C₃mpyr][NTf₂]/LiNTf₂ electrolyte versus the neat electrolyte system with enhancement of the anion and lithium self-diffusivity. Whilst the group were adding molecular solvents to ionic liquids to gain advantage for electrochemical reasons and not for the purpose of depression melting points, it is also likely they were simultaneously forming a eutectic between the [C₃mpyr][NTf₂] and molecular solvent.

The group highlighted that whilst these new systems fall foul of the strictest of ionic liquid definitions, these in no way limits their usefulness. The addition of molecular liquids into ionic liquids can lead to enhanced properties such as lower viscosity. Which in turn has led to molecular containing ionic liquids being successfully applied for protein dissolution and fixing,^{100,101} anti-microbial coatings¹⁰² and as electrolytes.¹⁰³ The likely success of these mixtures for the different applications is that the ion have a tendency to form pairs or aggregates as opposed to being insoluble or forming micelles in the molecular liquid which would render them ineffective.⁴⁴

Another iteration of solvents that stem from the ionic liquid realm are deep eutectic solvents, that were inspiration for work in this thesis, and are discussed in detail in the next section.

1.1.5 Deep eutectic solvents

1.1.5.1 History

The term deep eutectic solvent (DES)^{43,104,105} is most commonly used to describe low melting liquids formed by combining organic salts such as ChCl with Ur or other hydrogen-bond donor components including carboxylic acids and alcohols. DESs were initially popularized⁴⁵ as lower cost and more environmentally benign (greener) variants of non-volatile ionic liquids. Their uses as nonaqueous electrolyte solutions,¹⁰⁶ and media for nanoparticle and materials synthesis,^{107–110} solvents for catalysis,¹¹¹ and as vehicles for delivery of active pharmaceutical ingredients^{112,113} have been extensively investigated in recent years.

To improve the “greenness” of electroplating processes in line with the “12 green principles” set out by Warner and Anastas,¹¹⁴ Abbott and co-workers set out to design inexpensive, environmentally benign solvents that could be produced on scale.¹¹⁵ Looking to replace the current toxic precursors such as hexavalent chromic acid for the hard chromium plating process,^{116,117} They realised that when ChCl, the quaternary ammonium salt inducing the largest melting point depression in their earlier work,¹¹⁸ and the Brønsted acid Ur (which had been shown previously to form eutectic liquids with metal salts)^{119,120} were mixed in a $\chi_{\text{ChCl}} = 0.33$ ratio, a near room temperature liquid formed.¹¹⁵ This was the birth of the archetypal choline chloride:urea (ChCl:Ur) DES. Both starting components are shown in Figure 1.1-8.

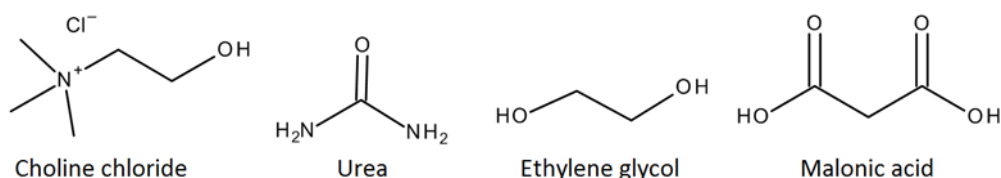


Figure 1.1-8: Choline chloride with hydrogen bond donors Ur, ethylene glycol and malonic acid.

In the same paper “deep eutectic” was used to describe these liquid forming mixtures and now is the widely accepted terminology for these solvent systems.¹¹⁵ Brønsted acid and base DES formation was not limited to the ureas, the group followed up this work by showing that ChCl could form DESs with many environmentally benign and inexpensive carboxylic acids.⁴⁵

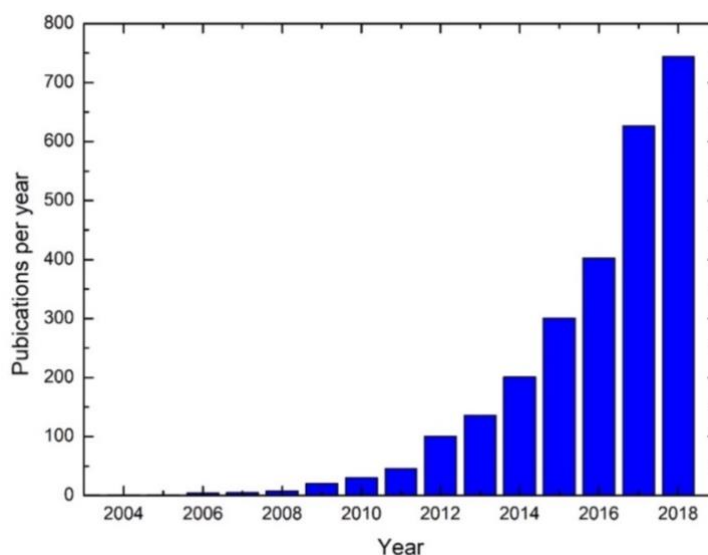


Figure 1.1-9: Number of papers published on deep eutectic solvents per year (Web of Science, date accessed:07/02/2019)¹²¹

DES liquid systems with their straightforward synthetic procedures, low cost and the potential to be environmentally inert, stimulated great interest as new solvent systems.^{43,105,122,123} The scientific community quickly grasped on to these solvents as the next wave of neoteric solvents, spun out from their ionic liquid predecessors. The graph in Figure 1.1-9 shows the exponential rise in deep eutectic solvent popularity from 2003 when Abbott coined the term,¹¹⁵ from only a handful of publications, the turn of the decade saw a significant uplift in publications to level of over 650 per year a figure which is continuing to rise. The reason for their likely success is because they offer the tunability or designer nature of ionic liquids however require no lengthy synthetic procedure therefore reducing their initial cost allowing them to be more economically viable than some ionic liquids whilst still being able to carry out the same functions, thus may be more suitable for scale up operations.

1.1.5.2 Definition

The term “deep eutectic solvent” was initially introduced by Abbott and colleagues in 2003,¹¹⁵ to describe the formation of the ChCl:Ur near room temperature liquid. The term was rapidly accepted as the nomenclature to describe these liquids, with little thought given to what the term DES actually means. As a matter of fact, there is no consistent definition in the literature, that would accurately describe the many systems that currently get published under the DES umbrella. Adding to the confusion is the fact that a number of these early DESs were given new commercialised names for example, Reline (ChCl:Ur) and Ethaline

(ChCl: ethylene glycol), these elude to a new compound having been formed not just mixtures of known compounds. In contrast to ionic liquids, where the term is regularly discussed/argued and re-defined, there is very limited discussion about terminology in the DES community. An attempt was made by Rogers and Gurau,¹²⁴ who highlight that some authors¹²⁵ use the terms ionic liquid and DES interchangeably, to describe the same species. They argue for the need for thorough speciation studies of each system and determination of the ionicity, to distinguish between the two, to avoid confusion to readers of the work. At the same time, as discussed in Section 1.1.4, molecular species have been prevalent in ionic liquids since their naissance, and such revisionism would call to change terminology in papers of Angell, MacFarlane, Johnson and others reducing the matter *ad absurdum*. What then constitutes a viable DES definition?

The word “eutectic” describes a well-defined physical phenomenon, discussed in detail in Chapter 1.1.1, but what does the term “deep” refer to? In theory, it is the ΔT between the actual experimentally measured eutectic point in a system and the theoretical eutectic point of the ideal liquid mixture of the pure starting components; in other words, a DES should have a eutectic point that is below the theoretical thermal limits of the mixture. However, in practice, most systems that are described by authors as DES do not actually live up to the physico-chemical scrutiny that is tied to this word. Phase diagrams, which are indispensable to accurately define whether a liquid mixture is, or is not, a DES, are oftentimes not investigated at all. Even if phase diagram is measured, many of these systems fail to crystallise due to the disruption of the crystal lattice of the starting components and are glass forming, hence, again fail to meet the criteria to be defined as a DES. Furthermore, it is not always beneficial to work at the eutectic point; working at a composition away from the eutectic point may be beneficial if a particular component in a mixture is more useful for the given application. Finally, often what it comes down to is that many authors simply do not care about physical chemistry of the systems they are using; most DES work centres around applications and not physico-chemical scrutiny, therefore as long as their liquid forming mixtures are suitable for the application, the authors are not concerned with underlying terminology. All these points are addressed in a publication by Coutinho *et al.*, who have made a commendable attempt to accurately define DESs and provide clarity to many misconceptions about the systems.¹²⁶ At the same time, this publication fails to deliver a robust solution to addressing the problem of what DESs actually are.

After coining the term,¹¹⁵ Abbott *et al.* gave a general formula to define DESs in 2007.¹²⁷ The formula $[N_{R1}R2R3R4]X \cdot Y$ was proposed by where R represents the substituents on the

quaternary ammonium salt, it was later updated to [Cat]X·Y to recognise that not only ammonium, but phosphonium¹²⁸ and sulfonium¹²⁹ cations can form DESs. X– represented the anionic halide and Y is typically a Lewis or Brønsted acid. Later on, Abbott attempted to generalise their approach to designing DESs, as per Table 1.1-2.¹²⁷

Table 1.1-2: General formula for DESs classification proposed by Abbott and co-workers¹²⁷

Type	General formula	Terms
Type I eutectic	$Y = MCl_x,$	$M = Zn, Sn, Fe, Al, Ga$
Type II eutectic	$Y = MCl_x \cdot yH_2O$	$M = Cr, Co, Cu, Ni, Fe$
Type III eutectic	$Y = R_5Z$	$Z = CONH_2, COOH, OH$
Type IV eutectic	$MCl_x + RZ = MCl_{x-1} + \cdot RZ + MCl_{x+1}$	$M = Al, Zn$ and $Z = CONH_2, OH$

Table 1.1-2 sets out the different types of deep eutectic systems, as proposed by Abbott in trying to define DESs. General formulas and definitions are useful as in general, it allows for better understanding of chemical systems.

An obvious problem with classifying these so-called DESs is that many of the systems are already well defined elsewhere in the realm of chemical sciences, and their behaviour well understood. To add to this, components that form “DES types I, II and IV” are indeed undergoing a chemical reaction, which often results in complex chemical speciation of the products – these phenomena should not be interpreted simply by eutectic formation.

A pitfall in this description of DESs can be seen in the **type I** DESs, described when considering one of the earliest reported ionic liquid systems by Hurley and Weir namely the aluminium chloride-ethyl pyridinium bromide ionic liquid.⁵¹ Figure 1.1-4 shows the phase diagram for that system and when compared to the ideal phase diagram for a binary eutectic system (Figure 1.1-1) we see that the ionic liquid is more complex as not only does it contain two eutectic depressions at $\chi_{AlCl_3} = 0.33$ and 0.67 but a congruent point at $\chi_{AlCl_3} = 0.50$, which as the authors reported signals the formation of a new compound $[C_2py][AlCl_3Br]$, the new compound with increased stability as expected has a higher melting point than the eutectic compositions hence the melting point spike seen in the phase diagram (Figure 1.1-4). Describing these systems with a blanket term such as DESs as seen in the definition by Abbott is short-sighted, as they are dynamic systems and very dependent on concentration of each component. **Type II** can be seen as an extension of the type I halometallate ionic liquids, the only difference being the inclusion of water which may enhance the properties of the liquid, much like 4th evolution of ionic liquids described by MacFarlane and co-

workers.⁴⁴ In terms of physical chemistry, instead of binary mixtures, these are ternary mixtures of metal halide, organic salt and water.

Type III are the most recognisable as DESs, and the first that were described by the term.¹¹⁵ They are classed as those eutectics formed between ammonium, sulfonium or phosphonium salts and alcohols/amides/carboxylic acids,⁴³ including the archetypal DES ChCl:Ur. These systems do not have the complex speciation as a function of composition (resulting from dynamic equilibria) as is seen in types I, II and IV. Liquid formation results from depression in melting point is attributed to various interactions including columbic and hydrogen bonding.^{130,131} The popularity of these type III DES systems can be accredited to Abbott and co-workers. They appreciated the potential of ionic liquids, but needed an alternative: an inexpensive, environmentally benign and scalable solvent to carry out electroplating. They realised such solvents were accessible by the mixing of two or more inexpensive components, already produced at scale, in certain ratios - originally a quaternary ammonium salt with an amide.¹¹⁵

Type IV DESs were differentiated from the others described in the general formula table (Table 1.1-2) by Abbott *et al.*, stating that “*These eutectics mixtures are distinctly different from type I and III eutectics and hence we propose to classify them as a type IV eutectic*”¹²⁷ with justification given as ZnCl₂ formed DESs with only a “*limited number of amides and dialcohols*” and the inability of Ur to form room temperature liquids with AlCl₃. As it has been highlighted,¹³² the same group then later went on to produce room temperature liquid AlCl₃-Ur/acetamide mixtures. What Type IV appear to be, are coordination complexes of a metal, by simple undergraduate chemistry standards, which for some reason happens to be a liquid. These have even more complex speciation than halometallate ionic liquids, and were later described as LCCs by Swadźba-Kwaśny and co-workers.⁷¹ Several groups carried out in-depth studies of LCCs, and an impressive variety of cationic, anionic and neutral species were revealed.^{75,133,134} In contrast, although Abbott and co-workers state that it was important to understand the speciation of the specific mixtures, they used FAB mass spectrometry as the sole speciation technique – even though it has been explicitly shown to be inadequate for the study of chlorometallate ionic liquids, with the exemplar system being a chlorozincate system.^{41,135}

On the other hand, despite its breadth, the definition does not encompass all useful mixtures developed under the DES umbrella – in particular, non-ionic mixtures that demonstrate eutectic behaviour are not included - such as those produced by Paiva *et al.*¹²² and those described in chapter 4 Hydrophobic DESs in this thesis. Paiva’s work show initially how

mixtures of citric acid with naturally occurring simple sugars (glucose and fructose) yielded room-temperature liquids, highlighting that DESs can form without the need for discrete ions to be present in the mixture. In my work, trioctylphosphine oxide (TOPO) has been combined with a series of alcohols and carboxylic acids - again showing melting point depression, forming ion-free room temperature liquid.

In conclusion, the numerous applications^{43,104,105,123} show that there is great interest in tailoring ILs past their classical definition; however, the term “DES” does not cater for the vast array of liquids being generated. At the same time, there is a well-founded, application-driven merit in developing such liquids, and they present interesting fundamental research opportunities. For practical reasons, it would be useful to have a definition that encompasses all of the room temperature liquid or near room temperature liquid mixtures, including mixtures that have a defined T_m , those that are glass-forming (given that like ionic liquids many of these DES type systems contain long alkyl chains which tend to inhibit crystallisation) and liquids that are being used at non-eutectic compositions. Currently, a definition within the literature which is broader/an alternative to DES and better describes many of these systems is Low Transition Temperature Mixtures (LTTMs) proposed by Francisco *et al.*¹⁰⁴ The definition aims to cover not only DES with defined eutectic points but also glass forming liquid mixtures. This is a step in the right direction; however, a publication that explicitly states that the definition proposed covers all of the liquid forming mixtures would likely be hugely beneficial to unifying the field.

In this work, following the literature *status quo*, the term “DES” is used to describe Type III mixtures.

1.2 Physical properties of DESs

Understanding the physical properties of ionic liquids and DESs is extremely useful for assessing whether systems are suitable for applications.¹³⁶ Engineering operations such as mixing and separations require an in-depth understanding of the physical parameters of the solvents, *e.g.* density and viscosity. However, measurement of physical properties of the DES is often overlooked.

1.2.1 Melting point

Conforming to the definition of a eutectic system given in 1.1.1, the melting point of DESs is significantly depressed compared to that of their starting components, due to a number of bonding interactions^{130,131,137} which disrupt the crystal lattice of the pure components.

Recording of the melting point of a DES or any solvent in fact is valuable as it dictates the liquid and hence operating range of the solvent. However, production of complete phase diagrams is often overlooked, as researchers are more focused on the benefits of application for a DES.

Numerous techniques can be employed to measure the melting point of DES including Differential Scanning Calorimetry (DSC),¹³⁸ hot stage Polarisable Optical Microscopy (POM) as seen in 2.3.2 and solid-liquid cell analysis.¹³⁸ The advantages of DSC over the other techniques is that scan rates can be fully controlled, as DSC records heat flow (W g^{-1}) enthalpy of melting can be determined and there is no aspect of the measurement that requires human influence, therefore error is reduced, conversely as seen in Figure 2.3-2 thermal events may be missed using DSC at higher scan rates. POM is advantageous as it allows for an optical observation to changes in the sample and the polarisable filters on the microscope allow for the detection of birefringence, hence indicate crystallinity of the sample. In solid-liquid cell analysis you observe the bulk sample, it is useful for samples that do not have a T_m but instead are glass forming, as you can observe when the DES vitrifies and no longer behaves as a liquid, therefore work out an accurate T_g temperature.

Identifying a consistent approach to determine what and how it is measured is an issue. For example, in the work of Abbott and co-workers, freezing points rather than melting points are reported for the original ChCl:Ur DES.¹¹⁵ Given that DESs and ionic liquids have a tendency to supercool,^{40,136,139,140} it is highly probable that the group would have recorded a higher melting point. This leads to confusion, with many authors stating that Abbott's data in his original ChCl:Ur paper report on melting points, when in fact they record freezing points.^{43,105} As highlighted by Andanson and colleagues,¹⁴¹ many liquids can exhibit supercooling,¹⁴² with ionic liquids systems and DESs being no exception,¹⁴⁰ leading to disparities between melting and freezing points. Furthermore, melting is a thermodynamic phenomenon, independent of experimental conditions, whereas freezing is influenced by kinetic factors. The seemingly interchangeable use of freezing and melting points in DESs literature is therefore incorrect.

Another issue pertains to water content in studied samples. High viscosities of DESs and their hydrophilic nature makes them particularly challenging to completely dry and maintain low water levels. This has led to disparity in data sets when measuring physical phenomena such as melting point especially for the ChCl:Ur DES as discussed in section 2.3.2, with even the most conscientious of practitioners, who followed rigorous drying routines recording water levels in the order of thousands of ppm.¹⁴¹ The neglect of understanding of

water content of the DES can lead to issues with recording physical measurements and also effect outcomes of reactions for application.

Finally, the formation of DESs occurs by disrupting crystal lattice formation of a pure compound by mixing it with another compound this will inherently lead to some DESs failing to crystallise under any conditions therefore in these circumstances it is important to record glass transition temperatures, T_g in place of melting points.¹⁴³ Understanding that these systems are not DES in the pure physical chemistry sense as they do not have a defined melting point, hence eutectic point but yet are no less valuable for application.

1.2.2 Viscosity

The viscosities of DESs tend to be high, and generally a lot higher than common organic solvents at room temperature, and higher than those of many common ionic liquids.⁴³ The viscosity, in essence the resistance to flow, is determined by varying interactions including hydrogen bonding and Coulombic interactions that dominate these liquids.^{130,131,137} With stronger donor/acceptor interaction likely leading to an increase in viscosity. The low free volumes in these solvents have also been attributed to their high viscosities¹⁴⁴ and this theory has been applied to produce DESs with lower viscosity and higher conductivities by using smaller cations and fluorinated hydrogen bond donors.¹⁴⁵ The viscosity of the ChCl:Ur system was recorded in this work was 2110 mPa S at 20 °C, which is considerably viscous given that neat glycerol has the viscosity of 1412 mPa S at 20 °C.¹⁴⁶ ChCl: ethylene glycol is often reported as a DES with low viscosity (30.9 mPa S at 25 °C)¹⁴⁷ although the stability of the DES is low: when left to settle, ChCl will precipitate from the liquid. With many DESs having high viscosities at low temperatures, they tend to be used at high temperatures to reduce viscosity, aiding mass transfer. There are many examples in the literature of the solvents being prepared and used at 100 °C and above.^{148–150} The problem concerning the use of these solvents at high temperatures is that small organic hydrogen bond donors such as Ur and oxalic acid have relatively high vapour pressures for room temperature solids, and relatively low decomposition points.^{151–154}

The original hydrophobic DES systems formed from long chain quaternary ammonium salts and decanoic acid also suffered from high viscosities.¹⁵⁵ This can be attributed to the charged polar centres present in the quaternary ammonium salts and the long alkyl chains. A strategy for reducing viscosity of hydrophobic DES is to include components that are non-ionic^{138,156}

therefore more of the bonding interactions are distributed throughout the molecular moieties which in turn leads to lower viscosities.

Comparable to T_m of DES, the absorption (given their hygroscopic nature) or addition of water to a DES will generally lead to a reduction in viscosity.^{157,158} Caution should be taken to ensure samples are prepared and viscosity measured in water-free conditions.

1.3 Applications of DESs

Like ionic liquids a decade earlier, DESs have enjoyed huge popularity as solvent systems, likely driven by factors including a clearly thought out rationale that using a eutectic system as a solvent is likely to lead to an improvement in a chemical system. However, equally that DESs being new and intriguing solvent systems trying any reaction in these solvents is justifiable and post use of the DES unforeseen benefits may be determined. Applications of DESs have been widespread, however, whilst many of the applications that have been published are valid and ground-breaking in their own right, there are examples where the advantage of using a DES is not clear or may be not suitable. Furthermore, in some cases, the actual role of DES in the process studied is somehow superficially explained.

1.3.1 Gas and volatile organic compounds (VOCs) absorption

DES have the ability to potentially absorb CO_2 ^{159,160} similarly to ionic liquids,¹⁶¹ this was demonstrated by Han and colleagues,¹⁶² who calculated the solubility of the gas across different ChCl:Ur mixtures, pressures and temperatures concluding that the $\chi_{\text{ChCl}} = 0.33$ eutectic mixture had the highest solubility for CO_2 , with solubility increasing with higher pressures and lower temperatures, with the highest amount of CO_2 being solubilised in any of the systems tested having a value of $\chi_{\text{CO}_2} = 0.309$ for the eutectic ratio at a pressure of 12.5 MPa and temperature of 40 °C. The solubility of the CO_2 could be due to the basicity of the DES which was calculated using the Hammett function (H).

$$H = \text{p}K(\text{HI}) + \log\left(\frac{[\text{I}^-]}{[\text{HI}]}\right) \quad \text{Equation 1.3-1}$$

Where $\text{p}K(\text{HI})$ represents the thermodynamic ionisation constant of the chosen indicator in water, $[\text{HI}]$ and $[\text{I}^-]$ represent the neutral and anionic forms of the indicator. The larger the H the more basic the medium is.

When 4-nitrobenzylcyanide was used as the indicator the Hammett function (Equation 1.3-1) for $\chi_{\text{ChCl}} = 0.33$ ChCl:Ur was calculated as 10.86 meaning the DES is weakly basic. Thus, has the ability to absorb an acidic gas such as CO_2 . Upon the uptake of CO_2 (1 atm) this value

decreased to 6.25 indicating that as expected the addition of CO₂ led to a decrease in Hammett function value and an increase in acidity of the system, as similarly to CO₂ dissolved in water, it is presumed carbonic acid formation occurs as well in the DES.¹⁶³

Moura *et al.* studied the effectiveness of DESs as green alternatives for volatile organic compounds absorption.¹⁶⁴ They determined the absorption capacities and vapour-liquid partition coefficients (*K*) (Table 1.3-1) of three VOCs in DESs where a lower value of *K* indicated a greater amount of VOC is solubilised in the solvent. Four ChCl, two tetrabutylphosphonium bromide (TBPBr) and one tetrabutylammonium bromide (TBABr) based DESs were tested.

Table 1.3-1: Vapour-liquid partition coefficients (*K*) of toluene, acetaldehyde and dichloromethane in water and in seven different solvents at 30 and 60 °C.¹⁶⁴

	Toluene		Acetaldehyde		Dichloromethane	
	30 °C	60 °C	30 °C	60 °C	30 °C	60 °C
Water	0.251	0.654	0.005	0.017	0.139	0.260
ChCl:Ur	0.096	0.180	<0.001	<0.001	0.124	0.143
ChCl:ethylene glycol	0.022	0.005	<0.001	<0.001	0.034	0.010
ChCl:glycerol	0.054	0.185	<0.001	<0.001	0.037	0.121
ChCl:levulinic acid	0.004	0.025	<0.001	<0.001	0.008	0.028
TBPBr:glycerol	0.004	0.005	<0.001	<0.001	0.005	0.002
TBPBr:levulinic acid	0.001	0.005	<0.001	0.001	0.006	0.015
TBABr:decanoic acid	0.001	0.001	<0.001	0.001	0.005	0.007

They concluded that the vapour-liquid coefficients of the DES systems were significantly lower than the corresponding VOCs in water as can be seen in Table 1.3-1 and these DES were identified as promising solvents for VOC capture. The enhance partition coefficients are likely due to the moieties in the DESs being similar to the present in the VOCs meaning they have high affinities for each other and the higher viscosity of the DESs decreasing the mobility of the VOCs out of the DES. The TBABr:decanoic acid DES was found to be the most effective sorbent for toluene 251-fold better than water at 30 °C, the same system was also the most effective sorbent for dichloromethane (28-fold, 30 °C) and for acetaldehyde, ChCl:Ur was found to be most effective likely due to hydrogen bonding effects and the similarities between acetaldehyde and Ur.

1.3.2 DES as organic reaction medium

DES have been used as a reaction medium for many organic syntheses in some cases not only acting as a solvent but as a catalyst given their potential acidity and being a reaction

component. These have been extensively reviewed by Alonso¹²³, García-Álvarez¹⁶⁵ and Liu¹⁶⁶. They offer an attractive alternative to common organic solvents given their potentially favourable properties which can include ease of synthesis, catalytic activity and being environmentally benign,⁴³ competing with traditional ILs and other systems such as supercritical CO₂ as solvent systems of the future. Their potential drawbacks include high viscosities, low thermal stability and being highly hygroscopic.

Azizi and Alipour demonstrated the formation of bisamides by adding aldehydes to ChCl:Ur DES heating the mixture to 80 °C (Figure 1.3-1).¹⁶⁷

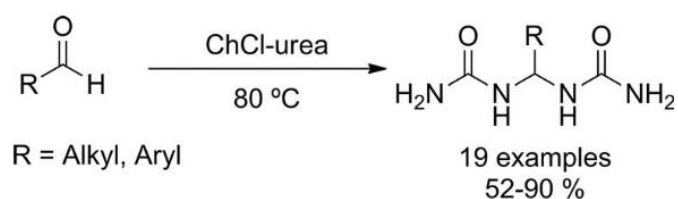


Figure 1.3-1: Formation of bisamides from aldehydes and ChCl:Ur DES¹²³

The aldehydes combining directly with the Ur in the DES forming the gem-bisamide product, a total of 19 different aldehydes were tested. They initially carried out a reaction optimisation procedure by combining benzaldehyde with Ur to form a bisamide in a number of different solvents, the ChCl:Ur DES was found to outperform the common solvent systems water, ethyl acetate, acetonitrile and toluene. They then went on to examine 19 different aldehydes in the DES finding that all of the aldehydes gave reasonable yields of 52% or more with 4-(trifluoromethyl)benzaldehyde giving the highest yield of 90 %.

DESs have been applied more recently in early 2019 for the catalysed selenocyanation of activated alkynes *via* an intermolecular H-bonding activation process.¹⁶⁸ The synthesis used the inexpensive and naturally biodegradable DES ChCl:glycolic acid as a reaction medium and a catalyst for the selenocyanation of activated alkynes. A desired amount of the activated alkyne starting material was added to 1 mol equivalent of water, 1.2 mol of potassium selenocyanate and 5 equivalents of the DES (Figure 1.3-2), the reaction mixture was then subjected to ultrasonic radiation for 35 minutes upon completion of the reaction the mixture was purified using column chromatography.

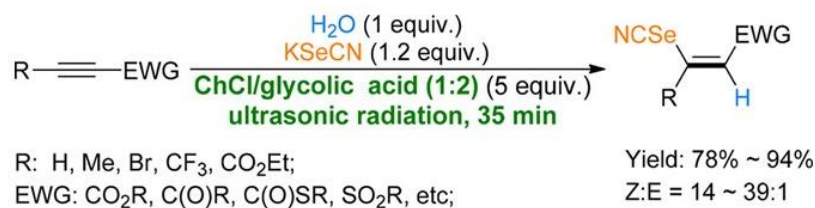


Figure 1.3-2: Synthesis of Z vinyl-selenocyanate using DES₁₆₈

The reaction conditions and solvents used were probed with a conclusion being drawn that the ChCl:glycolic acid systems gave higher yields and excellent selectivity, superior to those achieved in traditional organic solvents including THF₁₆₉ and anhydrous DMSO.₁₇₀ The authors cite that the dual role of the DES as medium and catalyst led to the simplification of this multicomponent reaction. This is an example of a DES playing an “active” role in promoting selective Michael addition reactions.

1.3.3 Nanoparticles

DESs have been used to mediate the nucleation and growth of nanoparticles,₁₇₁ Sun and co-workers showed how ~200 nm platinum nanoflowers with sharp single crystalline particles could be produced electrochemically onto glassy carbon in chloroplatinic acid (H₂PtCl₆) in ChCl:Ur at 80 °C. The platinum nanoflowers were found to have approximately double the electrocatalytic activity for ethanol oxidation compared to commercial platinum black.

Nanostructured ceria (cerium (IV) oxide) has also been synthesised in ChCl:Ur at temperatures between 100-180 °C.₁₁₀ This gave significant control over morphology and porosity producing ceria nanorods. The mechanism for the formation was probed using wide *Q*-range liquid neutron diffraction, Hammond *et al.* concluded that the DES acted as a supramolecular catalyst, where an increase in reaction rate induced by solvent-driven pre-organization of the reactants was the most significant factor. The degradation of the Ur component in the DES, which then went onto react with the cerium salt precursor and the strong interaction of Ur with the cerium metal ion facilitated the reaction pathway.

Discovering that CO oxidation could be achieved using gold catalysts at low temperatures, even as low as -70 °C,₁₇₂ sparked a huge interest in the use of gold as a catalyst. Following on from this Liao *et al.* synthesised gold nanoparticles in ChCl:Ur;₁₇₃ HAuCl₄·4H₂O and added to L-ascorbic acid were added separately into separate portions of the DES and stirred at 30 °C until the materials had dissolved in the DES. The solutions were then added together and allowed to react for a few hours, with a colour change from yellow to dark

purple indicating a successful reduction of Au(III) to Au(0). The nanoparticles formed were then examined using SEM and it was found that over 40 % of the particles had regular pentagonal symmetry, with the resembling a star (Figure 1.3-3).

The shape of the resulting nanoparticles could be altered by increasing or decreasing the amount of water present in the DES. The star shaped nanoparticles shown in Figure 1.3-3 exhibited high catalytic activity toward the electrocatalytic reduction of H_2O_2 which examined as a probe reaction.

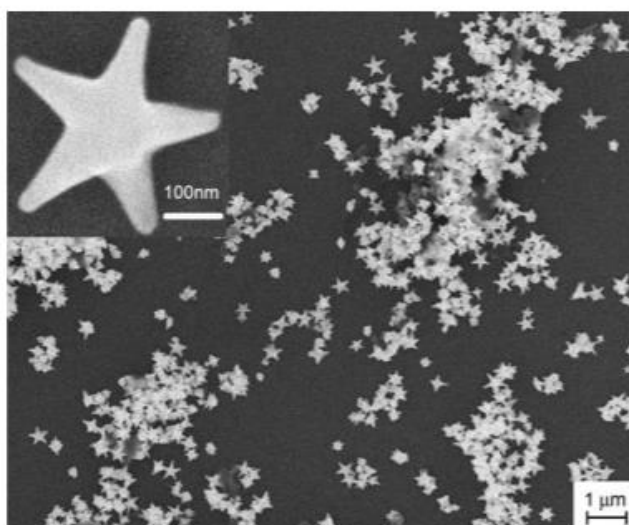


Figure 1.3-3: SEM images of star-shaped Au nanoparticles produced in $\text{ChCl}:\text{Ur}$ DES.¹⁷³

1.3.4 Natural product separation

As DESs themselves are inherently good hydrogen bond donors and acceptors they have a high affinity for hydroxyl and carboxyl groups, features that are commonly present in natural products such as sugars. This feature allows DESs to extract natural products with remarkable efficiency.¹⁷⁴ DESs can be tailored to be environmentally benign and have low volatilities making them an attractive alternative to common solvents for the extraction of natural products.

Nam and colleagues generated a lot of interest in the field of separations when they demonstrated how bioactive flavonoids could be extracted from the flowers of *Flos Sophorae*, a well-known source of Chinese herbal medicines, by a tailor-made L-proline:glycerol DES.¹⁷⁵ The DES extracted (50 mg quercetin, kaempferol, and isorhamnetin glycosides more efficiently than methanol using an ultrasound assisted

extraction technique. Recovery of the flavonoids from the DES was 75% using water as an anti-solvent, this increased to 92% when using C₁₈ solid phase extraction.

Vanilla is one of the most popular flavours globally and is present in food, beverages and perfumes. The volatile component of vanilla that is responsible for the characteristic aroma is vanillin (4-hydroxy-3-methoxybenzaldehyde), currently 12,000 tonnes are used annually with only 1% being derived from natural vanilla.¹⁷⁶ Extraction and isolation of vanillin is a non-trivial procedure and requires the use of organic solvents, currently ethanol is one of the only acceptable solvents for vanillin extraction as it is non-toxic making it suitable to be used in a flavouring product, however vanillin solubility in ethanol is limited. Gonzalez *et al.*¹⁷⁶ compared the extractability of vanillin from dried vanilla pods using DES made from nature components and alcohols to compare. Methanol extracted 18.0 mg g⁻¹ dried weight this dropped significantly for ethanol which extracted 4.4 mg g⁻¹ dried weight. Both systems were outperformed by a lactic acid:fructose DES which extracted 21.8 mg g⁻¹ dried weight of vanillin almost a five-fold increase when compared with the non-toxic alcohol ethanol, the current flavour and fragrance industry standard solvent. The results presented were very encouraging as a non-toxic DES which would be fit for human consumption, significantly outperformed the current standard solvent (ethanol) for the extraction of vanillin and may offer an alternative solvent which could be used for application which require high concentrations of vanillin, but 0% ethanol content is required.

1.3.5 Dissolution and separation of metals

DESs are thought to have great potential for metal extraction, and it has been reported that a number of DES can effectively dissolve metal oxides^{177–182} including ZnO, PbO₂, Cu₂O and V₂O₅, these can also be selectively extracted.¹⁷⁸ This opens up an opportunity for secondary mining from engineering waste and can be hugely beneficial, as it offsets both economic and environmental impact of engineering wastes such as red mud and fly ash. Ionic liquids have previously been used for metal oxide dissolution.¹⁸³ However, they have a number of drawbacks primarily in terms of their production costs, availability at scale and their own potential environmental impact.^{184,185}

Deep eutectic solvents potentially could be suitable for larger scale application as they are cost effective due to their main constituents already being produced in large quantities. Using the most studied DES as an example, ChCl:Ur, both are used heavily in the agricultural industry with ChCl an additive in chicken feed and Ur a main component in fertiliser, DESs can be tailored to be environmentally friendly as well as non-toxic, the

examples show they are already currently used in food production. This allows DES to be put into strong consideration as a possible solvent for metal extraction from waste on an industrial scale.

As solvents, largely water-free DESs have a distinct advantage over aqueous based solvents for metal coordination and extraction when due attention is taken to ensure their dry storage and absence of atmospheric conditions during metal oxide processing. The absence of water, which tends to combine with metals to form oxides and hydroxides,¹⁷⁸ should allow higher concentrations of metal ions to be extracted without, for example, using concentrated acid leachants. The properties of DES can also be tailored in a number of ways, to alter properties such as density¹⁸⁶ and melting point.

Research into metal coordination using DESs has been carried out using systems with a quaternary ammonium salt mixed with a hydrogen bond donor such as Ur.¹¹⁵ These Brønsted acid type DESs are advantageous for metal coordination due to the lack of metal ions already present in the solvent. The hydrogen bond donors (Ur *etc.*) are also currently produced in large quantities and are relatively inexpensive which make these DESs an attractive for large scale applications such as metal extraction.

Altering the hydrogen bond donor of the DESs has a marked effect on the affinity of the solvent for different metal ions. Abbott *et al.*¹⁷⁹ compared the ability of three different DES to dissolve a range of different metal oxides. The DESs studied were all based on ChCl and contained three different hydrogen bond donors; Ur, malonic acid and ethylene glycol.

Alongside the three DESs, control dissolution tests using NaCl solutions showed that dissolution of the metal oxides was not due only to the presence of chloride ions. Acidic HCl solution was also used as a comparison, due to it being the industry standard for dissolving metal oxides. The results from the study are presented in Table 1.3-2.

While the HCl solution overall outperformed the DESs, the malonic acid-choline eutectic results compared favourably, it is thought that the protons available in malonic acid act as oxygen acceptors allowing the DES to dissolve most of the metal oxides.¹⁷⁹ However it was only the Ur DES that outperformed HCl on any individual result, this was for CrO₃, showing that there are instances when DESs are potentially more suited for dissolution of metal oxides than even a strong acid such as HCl. The NaCl control solution performed poorly as expected with only showing reasonable solubility for CrO₃, however in general it was greatly outperformed by the malonic acid DES showing that solubility is not only down to the presence of the chloride ion and that there are other factors in play. All of the reactions were

carried out at 50 °C for 2 days, a number of the metal oxides that were being dissolved in the Ur DES were also carried out at 70 °C for 2 days, the 20 °C increase temperature led to a large increase in the yield of the dissolved metal oxide for Cu₂O it caused an increase by a factor of over 100 from 219 ppm dissolved in solution to 22,888 ppm, temperature is clearly critical for dissolution of certain metals such as Cu₂O in DES. This study shows that DES have the potential to be a viable solvent for dissolution of metal oxide.

Table 1.3-2 Metal oxide results from Abbott¹⁷⁹

Metal oxide	Malonic acid	Ur (50 °C)	Ethylene glycol	NaCl	HCl	Ur (70 °C)
TiO ₂	4	0.5	12	0.8	36	
V ₂ O ₃	365	148	7.5	3616	4686	
V ₂ O ₅	5809	4593	0.6	479	10995	
Cr ₂ O ₃	4	3	2	13	17	
CrO ₃	6415	10840	7	12069	2658	
MnO	6816	0	12	0	28124	
Mn ₂ O ₃	5380	0	7.5	0	25962	
MnO ₂	114	0.6	0.6	0	4445	
FeO	5010	0.3	2	2.8	27053	
Fe ₂ O ₃	376	0	0.7	11.7	10523	3.7
Fe ₃ O ₄	2314	6.7	15	4.5	22403	
CoO	3626	13.6	16	22	166260	
Co ₃ O ₄	5992	30	18.6	4.0	142865	
NiO	151	5	9.0	3.3	6109	21
Cu ₂ O	18337	219	394	0.1	53942	22888
CuO	14008	4.8	4.6	0.1	52047	234
ZnO	16217	1894	469	5.9	63896	90019

^a Solubilities/ppm were measured at 50 °C except for last column, which was obtained at 70 °C.

1.3.6 Electrochemistry in DES

For metal oxide treatment, dissolution in the DES is crucial, however, effective extraction techniques both to obtain selective extraction and to enable recovery of the desired precious metals are also vital for successful application. The complexity of this challenge is only increased by the fact that these engineering wastes contain a cocktail of different metal oxides, with a lot of them potentially being dissolved in the DES. Current research has shown successful, selective separation of a metal oxides using electrodeposition.¹⁷⁸ Initially 3 cm³ of $\chi_{\text{ChCl}} = 0.33$ ChCl:ethylene glycol with 0.1 mol dm⁻³ iodine was used to dissolve 90

mg of electrum (Au/Ag alloy), the mixture was left to stir for 2 days at 50 °C until all of the electrum had dissolved (Figure 1.3-4). Electrolysis was then performed on the electrum solubilised in the DES. Electroplating on to a nickel cathode yielded a deposit which was found to contain only Au and Ag while the remaining dissolved species stayed in solution. Proving that metals can be successfully recovered from a DES by electrolysis when using iodine as an oxidising agent.¹⁰⁶ The research gives supporting evidence that when an element with a relatively high reduction potential such as iodine is present it is possible to recover precious metals. An aspect of using electrolysis as a method of recovery of precious metals from DES that may prove challenging will be the ability to separate metals with similar redox potentials. An electrochemical series has been developed with $\chi_{\text{ChCl}} = 0.33$ ChCl:ethylene glycol being used as the solvent this was then compared to the redox potentials of the same metals in an aqueous solution.¹⁵⁰

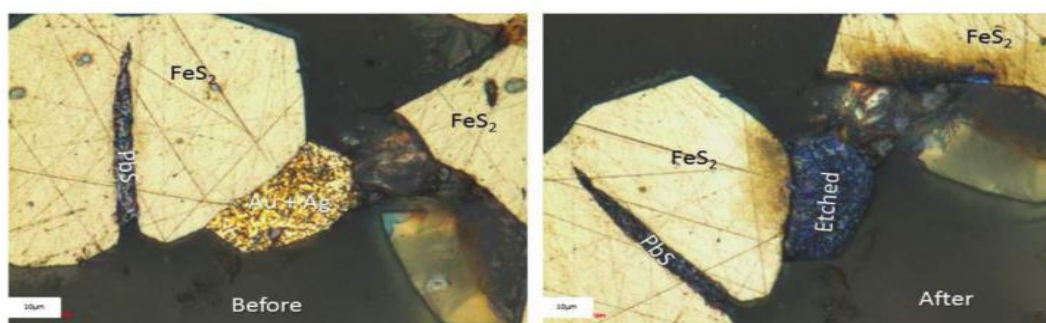


Figure 1.3-4: Reflected light optical microscopy image of electrum before and after reaction with $\chi_{\text{ChCl}} = 0.33$ ChCl:ethylene glycol.¹⁰⁶

The main industrial process for removing precious metal from engineering wastes is removal by acid leaching.¹⁸⁷ While in principle the acid leaching is effective, the leaching process is relatively slow¹⁸⁸ as it is carried out at low temperatures. Acidic leaching suffers from a lack of selectivity when leaching from waste¹⁸⁹ therefore the leachate potentially contains a variety of metal oxides which could make extraction of the valuable metals more difficult. An interesting method to increase efficiency and yield of acid leaching has been developed to recover vanadium and gallium.¹⁹⁰ Initially a sulfuric acid leach stage was implemented, yielding 2.8 mg/l of gallium, 35 mg/l vanadium and 4800 mg/l silicon. This gave a 2.4% yield for the extraction of Ga^{3+} , a similar result for the silicon and a slightly improved yield of 23% for vanadium. A chelating resin UNICELLEX^{®191} was then used to selectively absorb the metal ions increasing their concentration, finally solvent extraction was implemented to remove the valuable metal gallium and vanadium from the leachate. Tri-n-octylmethylammonium chloride (TOMAC) a quaternary ammonium salt was used as

the solvent extractant and was found to be very effective at removing gallium under acidic conditions, TOMAC was found to be highly selective in removing the Ga^{3+} , with none of the Al^{3+} that was present in the solution being extracted. Due to there being such a large concentration of aluminium oxide present in red mud, an extractant that shows selectivity towards gallium a target precious metal over aluminium which is in high concentration in waste samples is encouraging, more so an extractant that is a quaternary ammonium salt that has been included in the synthesis of DESs previously.¹⁵⁵ Once again it is shown that metal extraction tends to favour acidic conditions this was discussed previously, when Abbott *et al.*¹⁷⁹ dissolved metal oxides using DESs those that contained a high concentration of protons tended to be more effective at dissolving metal oxides than a more basic DES.

A scaled up reaction using DES to extract metal oxides from electric arc furnace (EAF) waste has been conducted.¹⁸² With a $\text{ChCl}:\text{Ur}$ 1:2 DES, efficient dissolution of the target Pb and Zn oxides was achieved, however the viscosity of the DES was too high to allow scale up. Changing the DES HBD component from pure Ur to ethylene glycol/Ur mixtures in a hybrid DES reduced the viscosity and, for the $\text{ChCl}:\text{Ur}:\text{ethylene glycol}$ 1:0.5:1.5 DES, there was only a small effect on the solubility of lead and zinc oxides. The new composition had a reduced viscosity of 56 cP from 800 cP which was more practical for the scaled-up reaction. It was noted that the addition of 1 wt% of the EAF dust waste caused a reduction in viscosity of up to 50% in the eutectic, this feature should be taken into consideration as a method to overcome high viscosity in DES that usually would be deemed unsuitable for industrial application. Conveniently it was also reported that the $\text{ChCl}:\text{Ur}$ DES was poor at dissolving both aluminium and iron oxides,¹⁸⁰ this larger scale experiment using EAF dust once again came to the same conclusion finding that only Zn and Pb were extracted, an initial smaller scale study found the extraction to be in the ratio 6:1,¹⁸² this is a desirable property for DES participating in metal extraction from matrices containing high percentages of both Al and Fe oxides allowing for the selective extraction of more valuable metals.

1.4 Motivation for this work

The aims of this work were two-fold: Firstly, to conduct fundamental studies to address questions about the nature and stability of DES, and secondly, to develop innovative metal recovery systems to reduce solvent impact in valorisation of industrial waste streams.

2 CHOLINE CHLORIDE:UREA DES

The very initial stage of this research probed known DES systems that would be suitable to solubilise metal oxides in engineering wastes. Interestingly, lack of fundamental research underpinning DESs' applications quickly became apparent, as most research groups drove to produce DESs for a wide range of uses, without appreciating the need for fundamental physical chemistry studies. Without this fundamental knowledge, it is likely that a DES may not be fit for its destined application, as a limiting physical parameter may be overlooked. In an attempt to deepen the current understanding of DESs, the archetypal ChCl:Ur DES was selected for an in-depth physical and fundamental structural study which is described in this chapter and in Chapter 3.

Physical chemistry of ChCl:Ur was studied using dried components, under moisture-free conditions. The phase diagram reveals that the eutectic melting point is 31.8 °C (higher than any of the previously reported values to date), and a previously-unrecognised phase region in the solid-liquid phase diagram, corresponding to a C1→C2 transition from α -choline chloride to β -choline chloride. Viscosities and densities, measured for the eutectic composition as a function of temperature, were compared with all data available in the literature, and discrepancies are discussed. Thermal stability studies reveal that the eutectic composition undergoes a thermal decomposition at temperatures as low as 90 °C (mass loss rate of 0.411 wt% h⁻¹), which calls for a careful consideration when using these solvents at elevated temperatures.

2.1 Introduction

The term deep eutectic solvent (DES) was introduced in 2003 by Abbott and co-workers.¹¹⁵ to describe low temperature liquids formed from mixtures of ChCl with Ur. Although a formal definition has not been provided, DESs are typically mixtures of simple organic salts acting as hydrogen-bond acceptors (*e.g.* ChCl) and small organic molecules acting as hydrogen bond donors (Ur), which have the capacity to form a eutectic mixture, preferably liquid at room temperature. Using low-toxicity, off-the-shelf components, DESs provided an attractive low-cost and low-toxicity alternative to traditional ionic liquids, with a promising potential for industrial uses.¹²³

The archetypal DES is the mixture of ChCl and Ur in 1:2 molar ratio ($\chi_{\text{ChCl}} = 0.33$) and has been used in a wide range of applications,¹⁰⁵ from metal electrodeposition,¹⁹² metal-catalysed

organic synthesis¹⁶⁵ and nanomaterial preparation¹⁷¹ to separations and extraction applications.^{193–195}

Considering the breadth of applications, and the very specific meaning of the term “eutectic” in reference to physical chemistry, the key thermal analytical data for ChCl:Ur mixtures are surprisingly inconsistently reported across the literature.^{113,115,141,158} In particular, the melting points used to construct the phase diagram vary between papers, including the eutectic melting point. Furthermore, solid thermal stability data are scarce, and estimates of the thermal stability of this system are vastly different across the literature and, because ChCl:Ur mixtures are often used at elevated temperature to overcome their relatively high viscosities, understanding of its long-term stability is of key importance for practical application.

With respect to the eutectic composition ($\chi_{\text{ChCl}} = 0.33$), in the first paper on ChCl:Ur DES,¹¹⁵ the eutectic prepared by mixing at 80 °C was found to freeze at 12 °C. The phase diagram was prepared using off-the-shelf components, without pre-drying, and the mixtures were reported to contain <1 wt% water, determined by ¹H NMR spectroscopy. Considering the molecular weight differential between ChCl:2Ur (259.76 g mol⁻¹) and H₂O (18.01 g mol⁻¹), this corresponds to one H₂O molecule for about seven ChCl:2Ur clusters, which is likely to have significant influence on properties. Another early phase diagram, constructed by Morrison *et al.*,¹¹³ for ChCl:Ur mixtures synthesised by solventless mixing at 100–150 °C. In contrast to Abbott *et al.*,¹ using differential scanning calorimetry (DSC) measuring from -60 °C to 125 °C with a temperature gradient of 1 °C min⁻¹, the melting point of the eutectic, determined from the DSC peak onset point, was found to be 17 °C.

Looking specifically at the influence of water on the ChCl:Ur DES, Shah *et al.*¹⁵⁸ prepared the $\chi_{\text{ChCl}} = 0.33$ mixture from ChCl and Ur dried overnight in a vacuum oven (under unspecified conditions) adding both components to a vial (with no reference to the exclusion moisture) followed by mixing in a sealed vial at 80 °C for 1 h. This composition was assumed to be absolutely dry (literally described as having zero molecules of water present), although no analytical data were provided for water content, and reported to have a melting point of exactly 12.00 °C from DSC measurement.

In the most rigorous study reported to date,¹⁴¹ described preparation of DES using starting materials dried under vacuum (0.1 mbar, 24 h, room temperature) and then allowed to react at 80 °C (no exclusion of moisture mentioned at this stage) to give residual water contents below 2000 ppm, and typically around 1000 ppm, measured by Karl-Fisher coulometry. The

solidus temperature of the eutectic point was measured using a thermostatic bath, with cooling rates of 0.025 or 0.25 °C min⁻¹, were reported as 28.3 and 29.7 °C, respectively. The liquidus temperature, determined by observation using heated-stage polarised optical microscopy at the same ramp rates were 30.1 and 28.5 °C, respectively. Using DSC, only solidus transitions were observed at 23.5 and 24.5 °C (for cooling rates of 0.025 or 0.25 °C min⁻¹, respectively) that were at lower temperatures than from the optical observations.

Strikingly, although most studies mention hygroscopic nature of this DES, there are no examples which have explicitly addressed the exclusion of moisture throughout the entire preparation and testing.

The viscosity of the ChCl:Ur eutectic ($\chi_{\text{ChCl}} = 0.33$) is 2.1 Pa s at 20 °C, which is far greater than viscosities of many ionic liquids (for example, 1-ethyl-3-methylimidazolium triflate has viscosity of 0.05 Pa s at 20 °C¹⁹⁶), which additionally contributes to this DES being used at elevated temperatures, commonly above 100 °C.¹⁴⁸ Solventless synthesis of the ChCl:Ur system at 100-150 °C have been reported¹¹³ and examples of high-temperature applications^{148,149,197} ranging from pre-treatment for the nanofibrillation of wood cellulose,¹⁴⁹ as catalysts for chemical fixation of CO₂ as cyclic carbonates,¹⁴⁸ to ionothermal syntheses^{110,198–200} have been described.

As such, these DES are often described as having high thermal stability,^{201–203} in analogy to ionic liquids. However, on the other hand, the thermal stability of pure Ur is rather low: whereas thermogravimetric studies with relatively higher heating rates place the T_g close to the melting point (130-135 °C),¹⁵³ TGA studies at more moderate heating rates of 1 °C min⁻¹ show thermal decomposition from 105 °C. Although the thermal stability of ammonium halide:Ur melts has been reported to be superior to that of pure Ur, ascribed to formation of strong, stabilising hydrogen bonds,²⁰⁴ it should be evident that high-temperature applications must be approached with caution. Interestingly, this low thermal stability of ChCl:Ur DES has been acknowledged in some cases and uses to advantage – *viz.* ceria syntheses at 80-100 °C, where Ur decomposition is used to rationalise the reaction mechanism and outcome.¹¹⁰

In this contribution, we set out to report thermal analysis data for the ChCl:Ur system, with carefully controlled water content, adopting best practice in drying and moisture-free handling of the studied samples.

2.2 Experimental

2.2.1 Materials and methods

ChCl (98%) and Ur (99-101%) were purchased from Sigma-Aldrich and used as received. Methanol was purchased from Fisher Scientific (99.8 % purity) and used as received.

2.2.2 Preparation of ChCl:Ur mixtures

Appropriate quantities of each component (Table 2.2-1) were combined in a 50 cm³ round-bottomed flask with a small quantity of methanol, then stirred at ambient temperature (500 rpm) until a homogenous, colourless liquid formed. Methanol and traces of water were removed by evaporation *in vacuo* (overnight, 40 °C, 10⁻² bar). Products were closed under argon, moved to a glovebox (MBraun LabMaster dp, <0.6 ppm O₂ and H₂O), and stored there until used.

Table 2.2-1: Molar fraction and masses of ChCl and Ur added to produce samples.

χ_{ChCl}	χ_{Ur}	ChCl mass/ g	Ur mass/ g
0.10	0.90	0.287	1.097
0.20	0.80	0.407	0.687
0.30	0.70	0.403	0.402
0.33	0.67	3.003	2.576
0.35	0.65	0.100	0.791
0.40	0.60	1.011	0.645
0.45	0.55	1.012	0.626
0.50	0.50	0.804	0.343
0.60	0.40	0.803	0.230
0.67	0.33	0.810	0.170
0.70	0.30	0.806	0.146
0.80	0.20	1.007	0.100
0.90	0.10	1.001	0.041

2.2.3 Water content analysis

Water content was measured for samples that were liquid near ambient temperature, using a coulometric Karl Fisher titrator (Metrohm 899).

In the glovebox, *ca.* 0.5 cm³ of each were drawn up into a 1 cm³ syringe, the tip of which was sealed with parafilm, and removed from the glovebox. Immediately before the

measurement, the parafilm was removed and a needle was placed on the tip of the syringe. The sample-containing syringe was weighed, then 2-3 drops of the sample were injected into the Karl-Fisher titrator, and immediately after - the syringe was re-weighed to find the mass of added drops. This mass was then entered into the titrator, to enable the water content to be determined as a mass fraction (in ppm).

2.2.4 Solid-liquid phase transitions analysis

Phase transitions were studied using differential scanning calorimetry (DSC) and polarised optical microscope (POM).

DSC experiments were performed using a TA Instruments DSC Q2000 fitted with RCS 90 cooling system. In the glovebox, samples were loaded into TA Tzero aluminium pans with TA Tzero hermetic lids. The sealed and removed from the glovebox. Masses of empty and filled pans were recorded (± 0.0002 g), from which masses of samples were calculated. In a typical DSC experiment, minimum two scans were recorded, cycling the temperature between -40 and 80 °C, at 0.1 to 5 °C min⁻¹. All DSC thermograms presented in this chapter and throughout the whole work show the 2nd scan unless otherwise stated.

POM studies were carried out using an Olympus BX50 microscope fitted with Cannon 500D digital camera. Microscope slides containing DESs samples were prepared in the glovebox and sealed using high-vacuum silicone grease (Dow Corning). The samples were removed from the glovebox and placed on a Peltier stage, fitted with a thermocouple, heating, and liquid nitrogen cooling. The samples were cooled to 0 °C, at *ca.* 5 °C min⁻¹, held at this temperature for 5 min, then heated at 1 °C min⁻¹, until completely liquefied. Upon heating, the samples were observed through the microscope and digital images of the sample were periodically captured, with temperature noted for each image. The polarisable lenses on the microscope were used to detect birefringence in the sample (indicative of crystalline species). The onset of melting and liquidus points were recorded in duplicate.

Densities were measured using a vibrating tube densitometer Mettler Toledo DM40. In the glovebox, samples were taken up into a 5 cm³ syringe and sealed with parafilm, then the syringe was removed from the glovebox. Immediately before the sample was injected into the density meter the parafilm was removed. The syringe remained in the inlet during the measurement and the outlet was capped to ensure no atmospheric moisture could contact the

sample during the measurement. Densities were measured within the temperature range of 20–90 °C, at 10 °C increments and 25 °C.

Viscosities were measured using a Bohlin Gemini cone and plate rotational rheometer. In the glovebox, samples were taken up into a 5 cm³ syringe and sealed with parafilm, then the syringe was removed from the glovebox. Immediately before the sample was placed onto the viscometer plate and covered with a cone, the parafilm was removed. Viscosities were measured within the temperature range of 20–95 °C, at approximately 6 °C increments.

2.2.5 Thermal stability analysis

Thermal stability was investigated by thermogravimetric analysis (TGA), and the decomposition products characterised using headspace GC-MS.

TGA curves were recorded using TA Instruments TGA Q5000. The masses of single-use TA aluminium cup and a TA aluminium lid were recorded using the TGA microbalance (± 0.0000001 g), which was then tared. The pans were transferred into the glovebox, filled with ChCl:Ur samples and sealed. Once removed from the glovebox, the pans were placed in the TGA autosampler carousel. The lid of each pan was pierced individually, 30 s before use. All measurements were carried out under a stream of dry nitrogen (20 cm³ min⁻¹) at a rate of 5 °C min⁻¹.

Dynamic TGA curves were recorded once heating a sample from 25 to 400 °C, at 5 °C min⁻¹. Isothermal TGA curves were recorded by heating each sample to 90 °C (5 °C min⁻¹) and holding at this temperature for 6 h.

GC-MS analyses were recorded using a Perkin Elmer Clarus 500. In the glovebox, the sample of the eutectic was placed in a GC vial and crimped. Then, it was placed in a sand bath standing on a hotplate in the glovebox and held at 90 °C for 24 h. Finally, the vial was removed from the glovebox and the headspace gases were analysed using the GC-MS.

2.3 Results and discussion

2.3.1 Sample preparation and water content analysis

In the case of DES, solventless syntheses are without a doubt a more sustainable route than those using a solvent. However, for the purpose of thermal analyses, it was decided to use small amount of methanol to solubilise components of the ChCl:Ur mixtures, thereby eliminating the need for excessive heat. Initially overnight drying of samples under reduced pressure at 80 °C, resulted in deposition of white crystals around the top of round-bottomed flasks used (Figure 2.3-1). The solid was identified as Ur by NMR spectroscopy. Consequently, the lower drying temperature of 40 °C was subsequently used. ¹H NMR spectra and TGA curves of the products dried at 40 °C showed no traces of methanol.



Figure 2.3-1: Ur crystals deposited on the neck of the flask after overnight drying at 80 °C, under reduced pressure

Thirteen samples were prepared, of which the four compositions between $\chi_{\text{ChCl}} = 0.33\text{-}0.45$ were homogenous liquids at ambient conditions, and a further three readily melted forming homogenous liquids at slightly elevated temperature (Table 2.3-1). Moisture contents of these sample compositions were measured in duplicate, using a Karl-Fisher coulometer. Water contents ranged from 100 to 500 ppm (<300 ppm on average, with a variance of 10-1400 ppm between replicate measurements on the same samples) and did not appear to correlate with DES composition (χ_{ChCl}). In general, water content was an order of magnitude lower than that reported by Meng *et al.*¹⁴¹

Table 2.3-1: Water content and appearance at ambient conditions of ChCl:Ur samples

χ_{ChCl}	Appearance	Karl-Fisher results /ppm water		
		Run 1	Run 2	Average
0.20	Solid	260	-	260
0.30	Solid/liquid suspension	500	440	470
0.33	Liquid	60	170	115
0.35	Liquid	310	460	385
0.40	Liquid	120	220	170
0.45	Liquid	450	440	445
0.50	Gelatinous solid	70	140	105

2.3.2 Phase diagram

DSC scans for two ChCl:Ur compositions, $\chi_{\text{ChCl}} = 0.33$ and 0.67, were recorded at three different scan rates: 0.1, 1.0 and 5.0 °C min⁻¹. At the highest rate of 5 °C min⁻¹ no phase transitions were detected for the eutectic composition. This was ascribed to supercooling and subsequent glass formation (Figure 2.3-1). Reducing the scan rate to 1 °C min⁻¹ resulted in a broad feature during the heating cycle associated with cold-crystallisation (the crystallisation observed upon heating a sample that had been previously cooled rapidly and did not have sufficient time to crystallise) followed by melting. On further reduction of the temperature scan rate to 0.1 °C min⁻¹, a two-step melting event for the $\chi_{\text{ChCl}} = 0.33$ composition was observed; however, this slow scan rate significantly increases the experiment time to the point of impracticability (33 h for a single cooling/heating cycle). It seems likely that the very low water contents present in the DES under examination here result in the increased viscosity and decreased molecular mobility, making it less likely to rearrange into a crystalline form, and more likely to undergo glass formation on cooling.

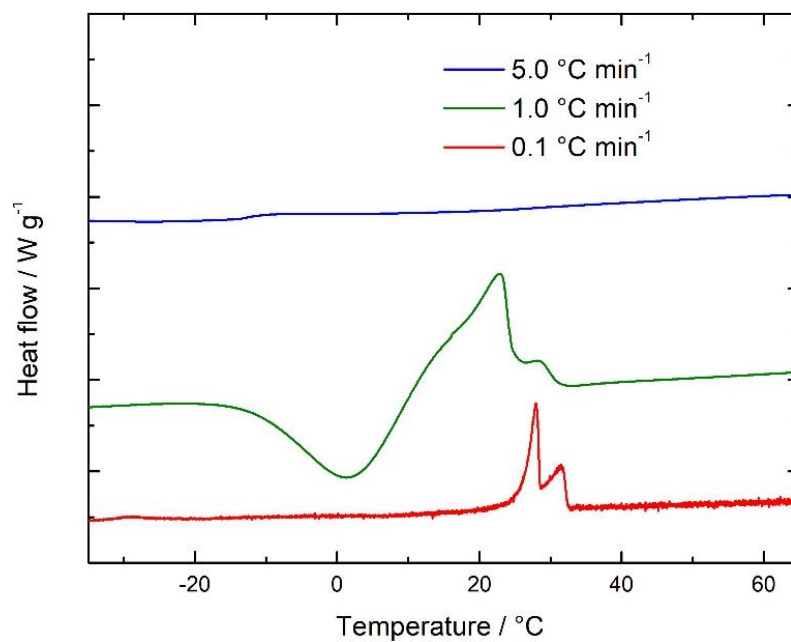


Figure 2.3-2: Fragments of DSC scans (heating) recorded for: $\chi_{\text{ChCl}} = 0.33$ at $0.1\text{ }^{\circ}\text{C min}^{-1}$ (—), $1.0\text{ }^{\circ}\text{C min}^{-1}$ (—) and $5\text{ }^{\circ}\text{C min}^{-1}$ (—). Scans displayed as exotherm down.

Since DSC was unsuitable to identify the transition points necessary for construction of the phase diagram, it was decided to use POM instead. Melting events, marked as temperatures at which melting of a crystalline phase (birefringent solid) to an isotropic liquid was complete (typically within $2\text{ }^{\circ}\text{C}$ from the event onset) are listed in Table 2.3-2 and were used to plot a phase diagram shown in Figure 2.3-2.

Table 2.3-2: Melting points of ChCl:Ur samples, derived from POM experiments

χ_{ChCl}	melting events / °C	
	eutectic phase melting	melting event 2
0.10	-	125.1
0.20	-	103.8
0.30	32.2	77.6
0.33	-	32.7
0.35	30.8	41.4
0.40	30.1	68.6
0.45	30.6	79.3
0.50	34.8	78.6
0.60	34.3	79.1
0.67	32.0	76.4
0.70	-	77.9
0.80	-	78.4
0.90	-	79.6

The literature reported melting points of ChCl (302 °C) and Ur (134°C),^{115,141} fit well with the data recorded here. The eutectic point was found at $\chi_{\text{ChCl}} = 0.33$, in agreement with previous studies of this DES.^{113,115,141,158} However, the eutectic composition was found to melt at 31.8 °C (T_1 , Figure 2.3-3), which is higher than values previously reported. Furthermore, a previously unreported solid-solid transition in the choline-rich side ($\chi_{\text{ChCl}} = 0.45$ -0.90) of the phase diagram was observed, with a melting point of 78 °C (T_2 , Figure 2.3-3) which was previously unreported.

The Ur-rich samples ($\chi_{\text{ChCl}} < 0.30$) are mixtures which contain an amorphous liquid phase and a crystalline solid, and exhibit a single melting at elevated temperatures. Within the composition range $\chi_{\text{ChCl}} = 0.30$ to 0.45, two phase transitions are observed as expected, the initial melting of the eutectic and the subsequent clearing of the solid + liquid mixtures with the exception of the eutectic point at $\chi_{\text{ChCl}} = 0.33$ (single melting point at $T_1 = 31.8$ °C). At temperatures above the respective second phase transition, all samples formed homogenous liquids. In the third region, $\chi_{\text{ChCl}} = 0.50$ to 0.67, there were three crystalline phases: the eutectic melting slightly below 32 °C; the α -ChCl phase, transitioning at *ca.* 78 °C to β -ChCl;²⁰⁵ and β -ChCl in the form of weakly crystalline powder, co-existing with a liquid phase. As expected, β -ChCl crystals did not melt until thermal decomposition was observed

under the microscope in the form of bubbles of gas (reaching complete decomposition *ca.* 260 °C).

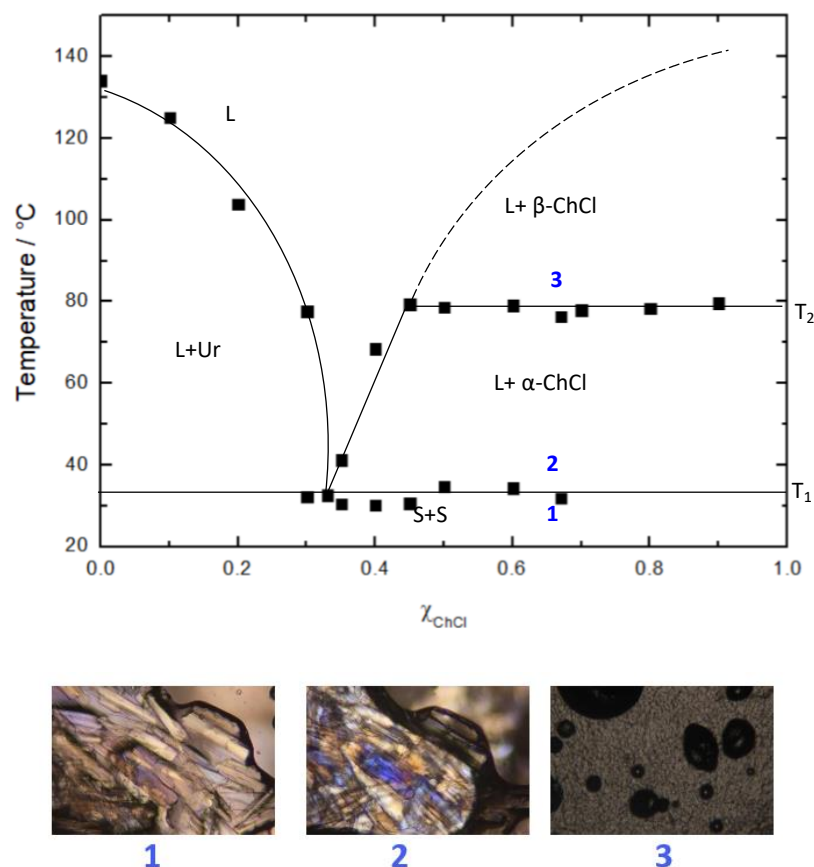


Figure 2.3-3: Phase diagram of ChCl:Ur, accompanied by POM images of the $\chi_{\text{ChCl}} = 0.67$ sample, captured at 25, 35 and 80 °C.

POM images of the three phases observed in the $\chi_{\text{ChCl}} = 0.67$ sample are shown in Figure 2.3-3. At 25 °C, the sample appears as a single solid phase (image 1). When the temperature of is increased to 35 °C, melting of the eutectic portion of the sample occurs at T_1 , and the sample contains a liquid and crystalline birefringent α -ChCl₂₀₅ particles under crossed polarisers (image 2). Upon heating to 80 °C, the crystalline portion of the solid + liquid mixture at T_2 undergoes a solid-solid transformation generating a new phase (β -ChCl)₂₀₅ dispersed in a liquid (image 3).

P-XRD data was collected at three temperatures (25, 35 and 95 °C) for the χ_{ChCl} (Figure 2.3-4), to examine changes in crystallinity of the samples as a result of the phase changes that were determined by POM (Figure 2.3-3). Comparing between the 25 °C (black) and 35 °C patterns (blue), an increase in the crystallinity of the sample can be seen (Figure

2.3-4), likely due to the melting of the eutectic portion of the mixture to reveal a crystalline α -ChCl. The addition of peaks between the 35 °C (blue) and 95 °C (red) patterns are due to the solid-solid transformation of α -ChCl forming β -ChCl.²⁰⁵

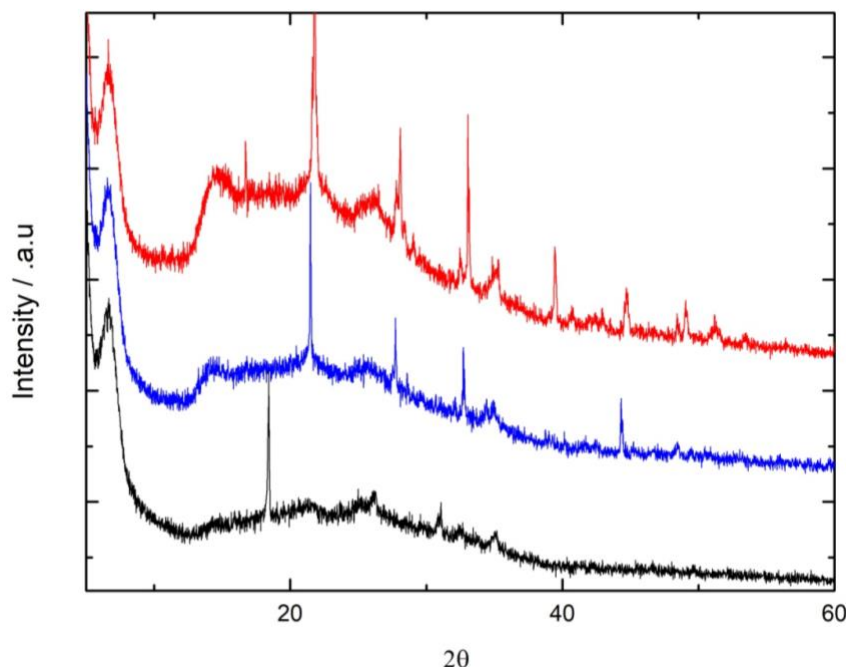


Figure 2.3-4: Powder XRD patterns, recorded as a function of temperature, for $\chi_{\text{ChCl}} = 0.67$, temperatures 25 °C (—), 65 °C (—) and 95 °C (—) are shown.

2.3.3 Physical properties

The ChCl:Ur system is extremely hygroscopic and it has been shown that the eutectic composition exposed directly to the atmosphere will eventually absorb up to 19% of water (by mass).¹⁴¹ As with ionic liquids, lack of control over water content will affect physical properties, with viscosity being much more susceptible to variation than density.²⁰⁶

Viscosity and density of the ChCl:Ur eutectic ($\chi_{\text{ChCl}} = 0.33$) were measured here with rigorous exclusion of moisture. The results are shown in Table 2.3-3 and are compared to the literature.^{158,207,208,115} Densities measured in this work fit to the linear relationship in Equation 2.3-1, where $a = -5.486 \text{ g cm}^{-1} \text{ }^{\circ}\text{C}^{-1}$ and $b = 1.213 \text{ g cm}^{-1}$, $R_2 = 1.000$.

$$d = aT + b \quad \text{Equation 2.3-1}$$

These results are in a general agreement with those reported by Pandey and Yadav,²⁰⁷ Xie *et al.*,²⁰⁸ and Su *et al.*,¹⁵⁷ with the average density at 30 °C being $1.196 \pm 0.001 \text{ g cm}^{-1}$. In

contrast, densities reported by Shah *et al.* (1.216 g cm⁻³ at 30 °C) and Abbott and co-workers¹ (Figure 2.3-5) are substantially higher. This coincides with their report of the eutectic melting/freezing point at about 12 °C, which could be related to the high water content in these samples at the time of the measurement. However, doping the DES with water has been reported to lower density rather than causing an increase,¹⁵⁸ therefore the origin of such discrepancies remain unclear.

Table 2.3-3: Viscosities and densities of the ChCl:Ur eutectic ($\chi_{\text{ChCl}} = 0.33$) as a function of temperature.

t / °C	viscosity / Pa s	t / °C	density / g cm⁻³
20.1	2.11	20	1.203
26.3	1.29	30	1.197
32.7	0.73	40	1.192
39.0	0.43	50	1.186
45.2	0.27	60	1.180
51.4	0.17	70	1.175
57.8	0.12	80	1.170
64.0	0.08	90	1.164
70.2	0.06	-	-
76.4	0.05	-	-
82.7	0.04	-	-
88.9	0.02	-	-
95.1	0.02	-	-

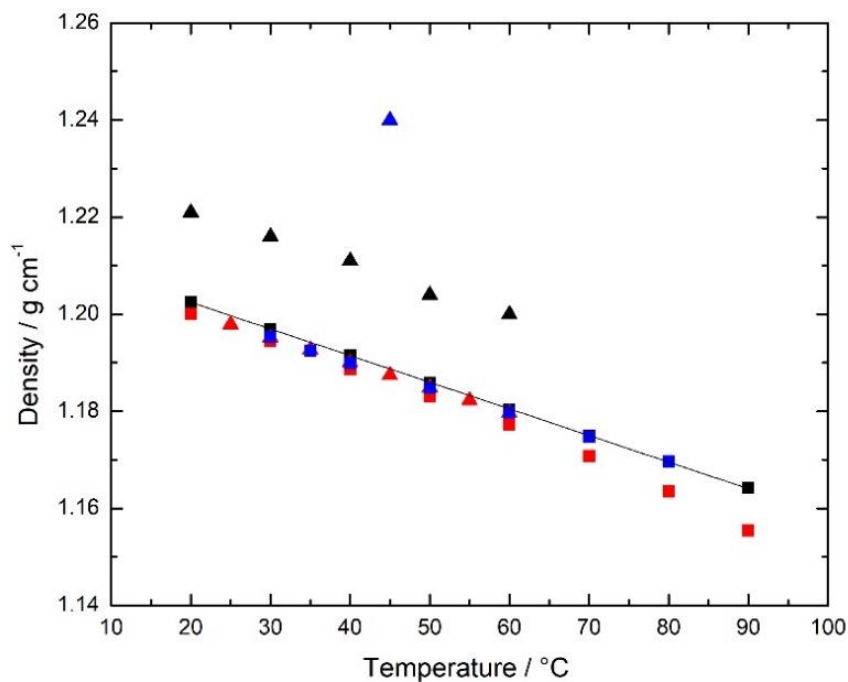


Figure 2.3-5: Comparison of density data recorded for the ChCl:Ur eutectic ($\chi_{\text{ChCl}} = 0.33$) as a function of temperature in this work (■), by Abbott *et al.* (▲),¹¹⁵ Pandey and Yadav (■),²⁰⁷ Xie *et al.* (▲),²⁰⁸ Shah *et al.* (▲)¹⁵⁸ and Su *et al.* (■).¹⁵⁷

Viscosities were fitted with a modified VFT Equation 2.3-2, where $C = 6.792$, $K = 1372.087$, $T_0 = 218.3$ K, $R_2 = 0.998$.

$$\eta = CT^{1/2} \exp\left(\frac{K}{T - T_0}\right) \quad \text{Equation 2.3-2}$$

The viscosities measured here are comparable to the results reported by Xie *et al.*,²⁰⁸ and are higher than those previously reported by Pandey *et al.*²⁰⁷ and Abbott and co-workers¹ (Figure 2.3-6). This is consistent with reduced viscosities associated with the presence of water in the latter materials.

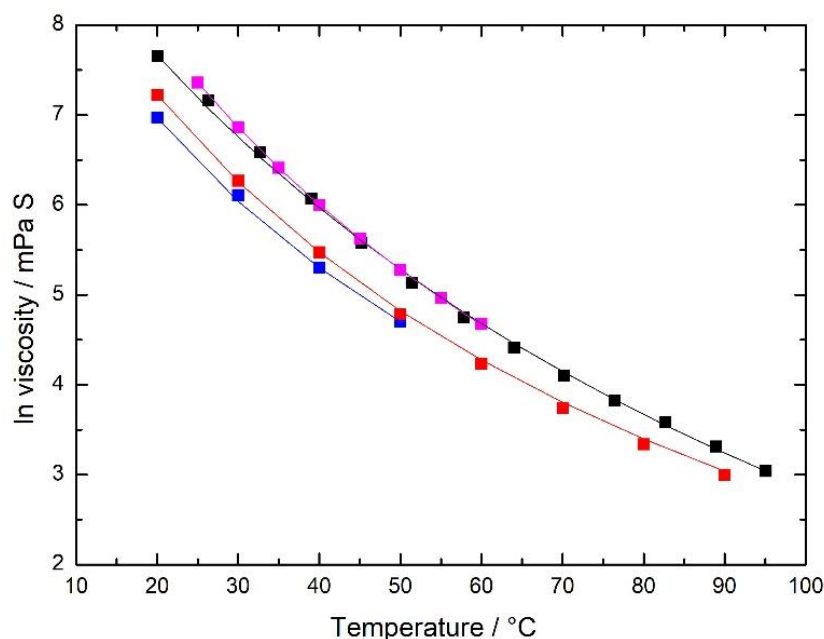


Figure 2.3-6: Literature comparison of \ln viscosity as a function of temperature for the $\chi_{\text{ChCl}} = 0.33$ ChCl:Ur DES, This publication, ■, Abbott *et al.*,¹¹⁵ ■, Pandey and Yadav,²⁰⁷ ■, Xie *et al.*²⁰⁸ ■.

2.3.4 Thermal stability

Samples of ChCl:Ur exposed to elevated temperatures (80-90 °C) for prolonged periods of time have a strong ammoniacal odour, and crystalline solids deposit around the tops of vessels that the materials are stored in. These observations formed the basis of the initial assumption that ChCl:Ur DES have poor thermal stability. This was studied in detail using TGA for two ChCl:Ur compositions, $\chi_{\text{ChCl}} = 0.33$ and 0.67 (Figure 2.3-7).

The eutectic composition ($\chi_{\text{ChCl}} = 0.33$), with the higher Ur content, exhibits lower thermal stability. Thermal decomposition follows a two-step decomposition pathway, with DTG maxima at 194 and 237 °C, starting with an onset attributed to decomposition of Ur ($T_d = 85$ °C). The ChCl-rich sample ($\chi_{\text{ChCl}} = 0.67$) appears to contain only a single stage to decomposition, and this has a slightly higher decomposition onset ($T_d = 110$ °C), which was lower than the extrapolated T_m for the composition (Figure 2.3-3). The DTG maximum of 242 °C, which is close to the second maximum in the eutectic composition. These results are in keeping with reports that Ur has greater thermal stability in quaternary ammonium salt/Ur mixtures.²⁰⁹ A comparative summary of thermal data derived from both curves is given in Table 2.3-4.

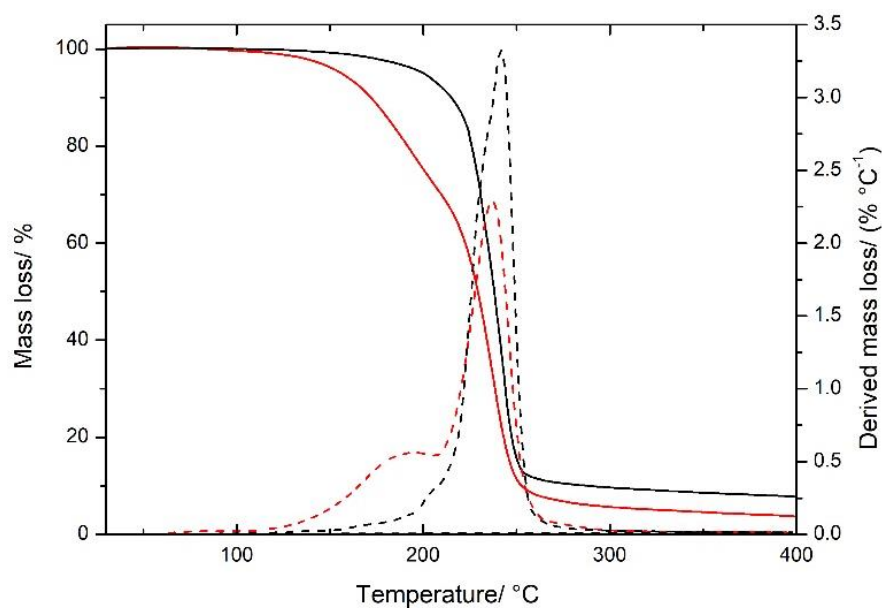


Figure 2.3-7: Dynamic TGA and DTG curves, recorded at 5 °C min⁻¹ for two samples of ChCl:Ur, $\chi_{\text{ChCl}} = 0.33$ (-), and $\chi_{\text{ChCl}} = 0.67$ (-), and derived mass loss for $\chi_{\text{ChCl}} = 0.33$ (---) and $\chi_{\text{ChCl}} = 0.67$ (---).

Table 2.3-4: TGA analyses of two samples of ChCl: Ur DES: $\chi_{\text{ChCl}} = 0.33$ and 0.67

Thermal event	$\chi_{\text{ChCl}} = 0.33$	$\chi_{\text{ChCl}} = 0.67$
<i>Dynamic heating (5 °C min⁻¹)</i>		
Onset of decomposition (°C)	85	110
5% mass loss (°C)	156	200
DTG maxima (°C)	194, 237	242
Final temperature (°C)	240	250
<i>Isothermal scan (90 °C)</i>		
Decomposition rate (% h ⁻¹)	0.411	0.067
Time to full decomposition (days)	10	62

Subsequently, isothermal TGA experiments were carried out to determine the stability of ChCl:Ur at 90 °C over 6 h (Figure 2.3-8). Decomposition rates were calculated based the mass loss in the linear components of the thermal analysis curves (Table 2.3-4). Mass loss from the eutectic composition was an order of magnitude faster than that from the ChCl-rich sample and could be extrapolated to complete decomposition over only 10 days. Both

samples show poor thermal stability at 90 °C, which is limiting in terms of practical applications.

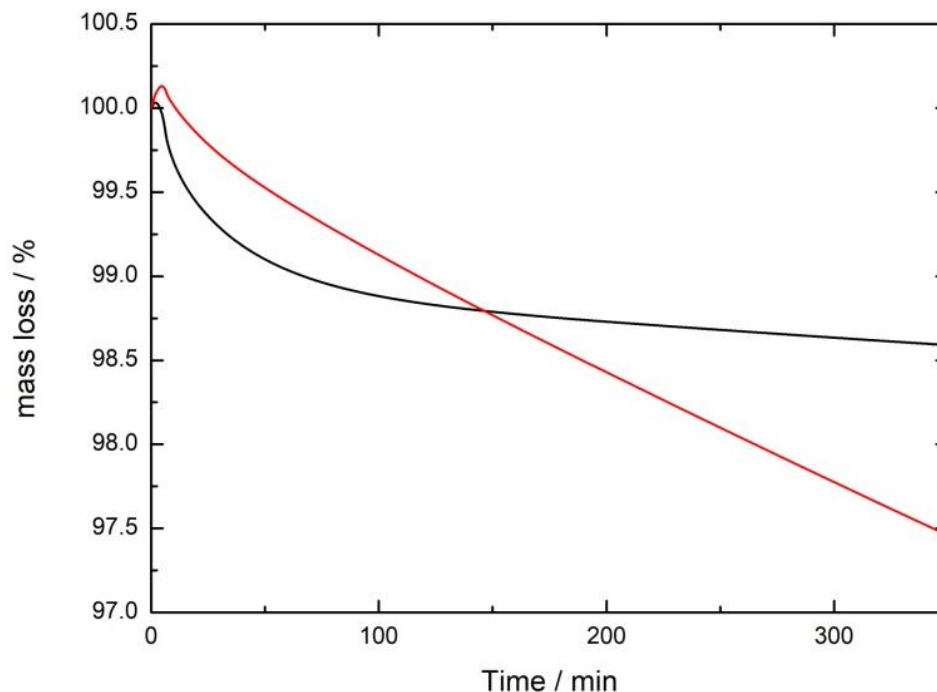


Figure 2.3-8: Isothermal TGA curves, recorded at 90 °C for two samples of ChCl:Ur, $\chi_{\text{ChCl}} = 0.33$ (—), and 0.67 (—).

The thermal decomposition of Ur to ammonia and biuret is firmly established in the literature.¹⁵⁴ Similarly, ammonia generation from aqueous Ur solutions has also been reported.¹⁵³ Both of these results appear consistent with the first step of decomposition pathway suggested for the ChCl:Ur eutectic, which is marked by ammoniacal odour. In order to confirm this, the gasses evolved from a sealed sample of ChCl:Ur eutectic ($\chi_{\text{ChCl}} = 0.33$) heated at 90 °C for 24 h, were analysed by GC-MS. The main component of the gaseous decomposition products was found to be ammonia ($m/z = 17$).

2.4 Conclusions

A phase diagram for the low-moisture content ChCl:Ur system was constructed across the full compositional range using DSC and POM to characterise the transitions. DSC gave very limited insight into the phase behaviour, but more informative results were recorded using POM. The eutectic melting point was found at 31.8 °C, and a second phase transition,

occurring at 78 °C, was observed in the ChCl-rich composition space and assigned as a crystal-crystal transformation from α -ChCl to β -ChCl.²⁰⁵

Viscosities and densities, measured for the eutectic composition as a function of temperature, were consistent with some literature reports,^{208,157} but were at odds with studies carried out on samples that were not dried.^{115,158,207}

Thermal stabilities of two ChCl:Ur compositions: the eutectic ($\chi_{\text{ChCl}} = 0.33$), and a ChCl-rich sample ($\chi_{\text{ChCl}} = 0.67$), were studied using TGA. Dynamic studies at 5 °C min⁻¹ revealed low decomposition onset in both samples, 85 and 110 °C, respectively. Isothermal studies have further confirmed thermal instability of both samples, with decomposition rates at 90 °C of 0.411 and 0.067 mass % per hour.

The overall applicative aim of this PhD research was the recovery of metals from waste engineering sources. One of the key strategies for this is the ionothermal dissolution of metal oxides in DESs, which had been previously demonstrated in the literature^{177–182} and in early work of this research (Appendix 1). After probing the physico-chemical properties of the ChCl:Ur DES, the conclusion can be drawn that it's higher-than-room-temperature melting point (31.8 °C), combined with a high viscosity (Figure 2.3-6), calls for higher temperatures for effective mass transfer of metal oxide in the solvent. However, this does not seem to be a sustainable strategy for industrial use (where long-term stability and recycling are required), as the eutectic composition is thermally unstable at temperatures below 100 °C (Figure 2.3-8), in-keeping with the literature for urea decomposition in both aqueous systems²¹⁰ and in DESs.^{209,211}

Careful consideration must be given when selecting a reaction temperature not only for metal oxide dissolution in DES but any reaction in these solvents due to their rather low thermal stability. Thought should also be given to the methods of formation of the DES, techniques such as twin-screw extrusion²¹² may be more suitable for making DESs at scale. Equipped with this knowledge, DES still remain an extremely interesting family of solvents.

3 Neutron diffraction determination of intermolecular structure from the ChCl:Ur and ChCl:oxalic acid liquid systems at 338 K

Experimental neutron scattering data performed at 338 K with empirical potential structure refinement (EPSR) structure analysis to compare ChCl:Ur and ChCl:oxalic acid $\chi_{\text{ChCl}} = 0.50$ (ChCl:Ox) in order to (i) evaluate thermal effects compared to the structure of ChCl:Ur reported at 303 K¹³⁷ and (ii) to investigate ChCl:Ox which is crystalline at room temperature⁴⁵ and is of interest for metal oxide dissolution.

Experiments were conducted using liquid-phase neutron diffraction with H/D isotopic substitution to investigate the liquid structures of 1:2 ChCl:Ur and 1:1 ChCl:oxalic acid deep eutectic solvents at 338 K. Differential neutron scattering cross sections were obtained and the experimental data were fitted to models using Empirical Potential Structure Refinement. In comparison to the previously reported study of ChCl:Ur at 303 K, a significant weakening and lengthening of choline–OH...Cl⁻ and choline–OH...hydrogen-bond acceptor correlations between the choline cation and both anion and HBA molecules was found suggesting that these interactions are less important to the liquid structure that had been previously assigned.

3.1 Introduction

The melting point depressions present in choline-based DES,^{43,104} as exemplified by the ChCl:Ur $\chi_{\text{ChCl}} = 0.33$ DES with a melting point 178 K lower than that of the two components, was first considered to be due to the formation of complex anions, for example $[(\text{Ur})_2\text{Cl}]^-$, through hydrogen bond donor (HBD) to anion hydrogen-bonding as the driving force for liquid formation.^{104,213,214}

However, recent neutron scattering studies^{137,215–217} and simulation^{218–222} have revealed that the interactions between the different components present in these DES is much more complex,¹⁰⁵ with competing strong and weak Coulombic and hydrogen-bonding interactions between all the liquid components. However, the details of the relative contributions of different interactions to the structure and experimental data on which to build this understanding is only slowly being developed. Notably, Ashworth *et al.*²²⁰ have discussed the need to consider the complete range of hydrogen-bonding and Coulombic interactions

possible, highlighting the potential to form both complex anions: *e.g.* Ur[Cl]⁻, and cations, such as Ur[choline]⁺.

Most recently, using inelastic neutron spectroscopy (INS) and vibration spectroscopy, Araujo *et al.*²²³ have argued that the interplay of soft and strong interactions in ChCl:Ur confers flexibility to newly formed hydrogen-bonding networks allowing the ensemble to remain liquid at room temperature. It was noted that short choline–OH...Cl correlations (at 2.1 Å) reported by Hammond, Bowron, and Edler¹³⁷ with similar separations to those found in the crystal structure of ChCl are contrary to expectation. Furthermore, vibrational analysis revealed that choline exists predominantly in the *gauche* conformer in the DES with a small *trans* population that is indicative of freer but still restricted rotation of the C–C bond in the liquid state than in the solid and that Ur moves from the solid state sp² planar structure to one with the nitrogen sites adopting a partially pyramidal sp³ conformation. This loss of planarity is a direct response to the fluctuating and flexible hydrogen bond network in the DES with the Ur engaging in a wide number of intermolecular contacts with varying strengths.

Examining the $\chi_{\text{ChCl}} = 0.50$ choline:malic acid (ChCl:Mal) DES, the chloride ion environment was been described as being more robust than that in ChCl:Ur with respect to dissociation forming acid–acid clusters.²¹⁷ This was rationalised in terms of stronger chelation of chloride by malic acid and appears consistent with quasielastic neutron scattering (QENS)^{216,217} measurements that show lower chloride anion mobility compared to choline cations suggesting greater involvement of chloride in hydrogen-bonding networks.

These descriptions of the DES liquid network, with correlations between all the components, are analogous to those also found mixtures containing ionic liquids, for example, ionic liquid:phenol (1:1)²²⁴ and 1-methylnaphthalene (1:1)²²⁵ systems, although the ionic liquid:phenol systems form a eutectic mixture whereas the ionic liquid:polyaromatic systems formed a stable peritectic 1:1 complex with π - π stacking between imidazolium cations and the aromatic naphthalenes. As interest in DES-forming systems continues to increase, there is a need to obtain additional experimental structural data to understand how changes in the nature of the HBD components affects structure and properties, especially the effect of temperature, taking into account the growing interest in using DES for ionothermal materials synthesis.^{110,226,227}

3.2 Experimental

Hydrogenated ChCl, anhydrous oxalic acid, Ur, and Ur-D4 were purchased from Sigma-Aldrich. ChCl-D9 ([¹³C(²H₅)₃N(CH₂)₂OH]Cl) was purchased from CDN Isotopes (QMX

Laboratories, Thaxted, UK) and Cambridge Isotopes (Goss Scientific Instruments Limited, Crewe, UK). Anhydrous oxalic acid-D₂ was prepared by H/D exchange from oxalic acid with D₂O (3×) followed by freeze-drying under vacuum.

Infra-red spectroscopy (Figure 3.2-1) was used to compare hydrogenated oxalic acid with prepared deuterated oxalic acid pre/post drying to confirm successful isotopic exchange. We see a shift in the peak caused by the O-H bonds present in oxalic acid-H₂ (black line) from 3200 to approximately 2100-2300 cm⁻¹ in the dry deuterated oxalic acid (blue line), this confirms that the molecule has been deuterated with the shift to a lower wavenumber being due to the increased mass of deuterium compared to hydrogen, similar to the reduction in wavenumber of the O-H band between H₂O and D₂O when examined by infra-red spectroscopy.²²⁸

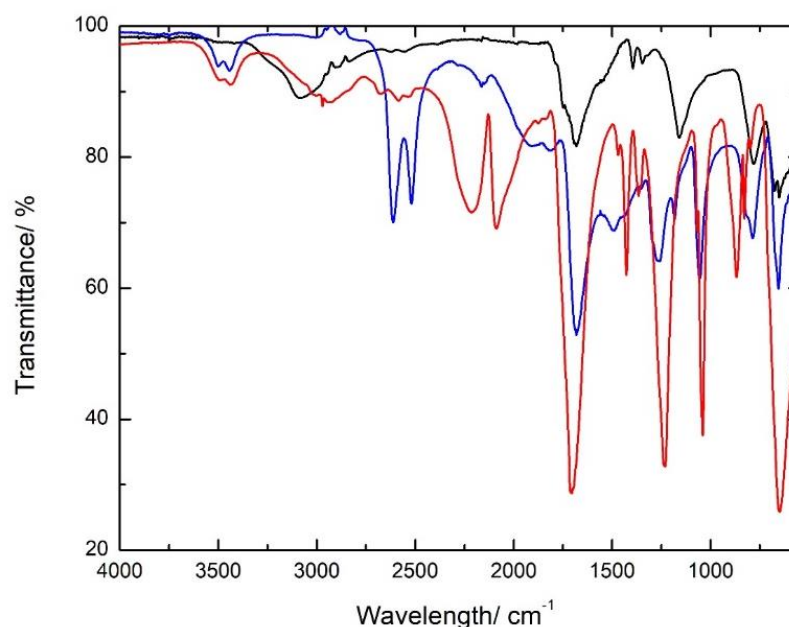


Figure 3.2-1: Infra-red spectrum for oxalic acid-H₂ (—), oxalic acid-D₂ (pre-drying, —) and oxalic acid-D₂ (post-drying, —).

Comparing the pre-drying and post drying oxalic-D₂ samples we see that the double peak at 2500 cm⁻¹ in the pre-drying sample is no longer present in the post drying sample, this was due to the excess D₂O,²²⁸ which was present in the undried sample once subjected to the freeze drying process this peak was no longer present confirming that that only trace levels (if any) of D₂O were left in the oxalic acid.

Isotopically substituted samples were made by mixing the appropriate deuteriated or protiated ChCl with Ur (1:2 molar ratio) and oxalic acid (1:1 molar ratio). Samples were

prepared under an inert atmosphere, heating at 333 K until homogeneous liquids were produced. On cooling to room temperature all the DES samples solidified. The ChCl:Ur DES melted at 304 K, consistent with the literature reported range for ChCl:Ur DES.¹⁴¹ Melting points for the crystalline ChCl:Ox DES ranged from ca. 323-333 K (Table 3.2-1) depending on the isotopomeric substitution and contrast with the reported solidification temperature of 307 K.⁴⁵

Table 3.2-1: Melting points determined by DSC for isotopomerically substituted ChCl:Ox mixtures.

Sample	Melting point/ K		
	Initial	Peak maximum	Final
ChCl-H:Ox-H	No Melting or Tg observed		
ChCl-D:Ox-D	284.3	326.0	334.2
ChCl-D:Ox-H	299.3	333.9	342.1
ChCl-H:Ox-D	308.3	336.2	344.4
ChCl-H/D:Ox-D	299.0	321.4	341.7
ChCl-D:Ox-H/D	297.4	331.4	338.6
ChCl-H/D:Ox-H/D	No Melting or Tg observed		

Seven isotopic contrast samples were prepared for ChCl:Ox with compositions of H:D, D:H, H:H, D:D, H/D:H/D, H/D:D, and D:H/D (ChCl:hydrogen bond donor), where H/D signifies equimolar mixtures of the hydrogenation and deuteriated components. For ChCl:Ur, four compositions (H:H, D:D, H:D, and D:H) were examined.

Neutron scattering data were collected at the ISIS pulsed neutron and muon source at the Rutherford Appleton Laboratory, UK, using the SANDALS (ChCl:Ox) and NIMROD (ChCl:Ur) spectrometers. Each sample was contained in “null scattering” Ti_{0.68}Zr_{0.32} flat plate cells with internal geometries of 1 × 35 × 35 mm, with a wall thickness of 1 mm. During measurements, the cell was maintained at a temperature of 338 K using a recirculating heater (Julabo FP50). Measurements were made on each of the empty sample holders, the empty spectrometer, and a 3.1 mm thick vanadium standard sample for the purposes of instrument calibration and data normalisation.

Data reduction was performed using GUDRUN²²⁹ to produce a differential scattering cross section for each experimental sample. The experimental sample densities and scattering levels were consistent with the actual isotopic compositions of the samples. Calibration and background subtraction for single atom scattering was made to produce a differential scattering cross section for each sample. Data from the neutron diffraction experiments was

kindly fitted and analysed by Prof J.D. Holbrey using the Empirical Potential Structure Refinement (EPSR) program.^{230,231}

The experimental total structure factors, $F(Q)$, were extracted from the neutron scattering data for each of the isotopically distinct samples at each composition. These were used to build and refine three dimensional models of the liquid structure consistent with the experimental data using EPSR for each DES. By comparing the differences between calculated and experimental structure factors in Q -space for data sets, an empirical perturbation potential is determined. This is combined with the reference potential and used as the new potential for simulations, iteratively driving the simulation model towards agreement with experimental data.

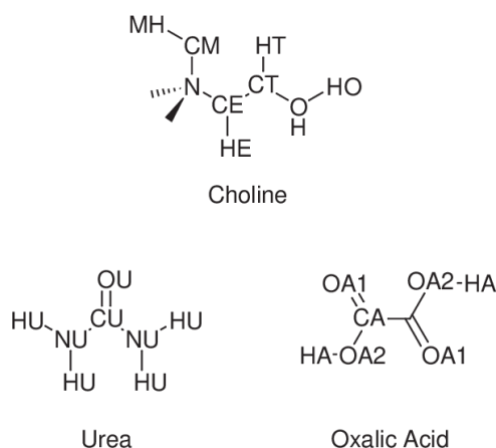


Figure 3.2-2: Atom types assigned to the choline, Ur, and oxalic acid molecules used in the EPSR simulation of diffraction data.

Table 3.2-2: Initial Lennard-Jones (ϵ and σ) and charge (q) parameters used for the reference potential of the Empirical Potential Structure Refinement model for both systems derived from the literature, and OPLS-AA.

Atom type	ϵ /kJ mol	σ /Å	q /e
Choline Chloride			
Cl	0.80	4.0	-1.0000
N	0.70	3.2	-0.15456
CM	0.80	3.7	0.10974
CE	0.80	3.7	0.07411
HM	0.00	0.0	0.05244
CT	0.80	3.7	0.16201
HE	0.00	0.0	0.05244
HT	0.00	0.0	0.05244
OH	0.65	3.1	-0.3126

HO	0.00	0.0	0.22008
Oxalic acid			
CA	0.80	3.7	0.68306
OA1	0.65	3.1	-0.53552
OA2	0.65	3.1	-0.54506
HA	0.00	0.0	0.44452
Ur			
CU	0.80	3.7	0.40060
OU	0.65	3.1	-0.41760
NU	0.70	3.2	-0.45240
HU	0.00	0.0	0.23045

Table 3.2-3: Intramolecular bond distance (Å) and bond-angle (°) constraints used to define the basic structure of the components in the initial EPSR simulation model. Oxalic acid was fixed to a planar conformation by defining O-C-C-O dihedral restraints.

Bond (Å)		Bond Angle (°)	
Choline Chloride			
CM-HM	1.08	HM-CM-HM	108.5
CM-N	1.51	HM-CM-N	108.5
N-CE	1.56	CM-N-CM	108.5
CE-HE	1.08	CM-N-CE	110.0
CE-CT	1.46	N-CE-HE	108.5
CT-HT	1.08	N-CE-CT	114.6
CT-OH	1.44	HE-CE-HE	108.5
OH-HO	0.97	HE-CE-CT	108.5
		CE-CT-HT	108.5
		CE-CT-OH	112.6
		HT-CT-HT	108.5
		OH-CT-HT	108.5
		CT-OH-HO	118.0
Oxalic acid			
OA1-CA	1.22	OA1-CA-OA2	119.5
OA2-CA	1.35	CA-OA2-HA	115.6
CA-CA	1.54	OA1-CA-CA	124.3
OA2-HA	0.95	OA2-CA-CA	116.3
Ur			
OU-CU	1.26	OU-CU-NU	119.9
NU-CU	1.39	CU-NU-HU	120.1
NU-HU	0.99	HU-NU-HU	119.7

The EPSR refinements were performed using 400 ChCls and 800 Ur molecules (ChCl:Ur 1:2), and 500 ChCl; ion pairs and 500 oxalic acid molecules (ChCl:Ox 1:1). The simulations were performed using cubic boxes of dimension 53.51 and 54.06 Å, respectively. Models were refined against the experimental data over the full data range ($Q = 0.1\text{--}50\text{ Å}^{-1}$). Within the EPSR simulation, initial potentials and interatomic distance constraints used to define the basic molecular geometries were obtained from MOPAC with the AM1 model. Atom types in each system were defined based on their unique positions in the molecular skeletons, as shown in Figure 3.2-2, and full rotational flexibility was enabled in the model. The full parameters of the reference potential used are given in Table 3.2-2 and the interatomic distance and angular constraints used to define the basic molecular geometries are summarised in Table 3.2-3.

Simulations were allowed to equilibrate for at least 2500 cycles before applying the empirical potential, then were equilibrated over *ca.* 10,000 cycles before accumulating and averaging data. The total numeric density of the simulation box corresponded to the experimentally determined molecular densities of the fully protiated materials. Centre of mass radial distribution functions (RDFs) were calculated using the SHARM routines within EPSR.

3.3 Results and discussion

The experimental neutron diffraction data, collected at 338 K for ChCl:Ur (1:2) and ChCl:Ox (1:1), was modelled with EPSR refining against the experimental data from each set of H/D isotopically distinct samples. Data and the corresponding fits from the EPSR simulation (Figure 3.3-1) show good consistency between the experimental and the EPSR derived models. The greatest source of discrepancy between experimental data sets and EPSR fits were found at $Q < 1\text{ Å}^{-1}$ where corrections for inelastic scattering by hydrogen are most difficult.²³² In addition, the poorest convergence of experimental and fitted scattering data was found for the H:D samples containing protiated choline and either deuteriated Ur or oxalic acid.

Centre of mass RDFs for choline, Cl-, and the HBD component (Ur or oxalic acid) in the two DES are shown in Figure 3.3-2 with the corresponding peak maxima for the first shells shown in Table 3.3-1. These correlation distances are comparable to the equivalent site-site partial radial distribution functions (pRDFs) reported at 303 K¹³⁷ and ChCl:Mal²¹⁷ and, in

general, with computational experimental results.^{130,219} Both ChCl:Ur and ChCl:Ox show similar centre of mass RDFs with comparable correlation peak positions and shapes. The notable exceptions are correlations to the HBD sites (Ur or oxalic acid) where the peak in the respective RDFs occur at shorter distances for Ur than oxalic acid. This can be rationalised in terms of the relative sizes of the two HBD. Strong correlations are clearly evident between the HBD molecules and both chloride and other HBD molecules. In both ChCl:Ur and ChCl:Ox, the choline–HBD peak (5.4–6.0 Å) occurs at longer distances than the choline–chloride correlation (4.5–5.0 Å) but at a shorter distance than the corresponding choline–choline correlation (6.3–6.4 Å) indicating that there is intercalation of the molecular HBD components into the ionic lattice.

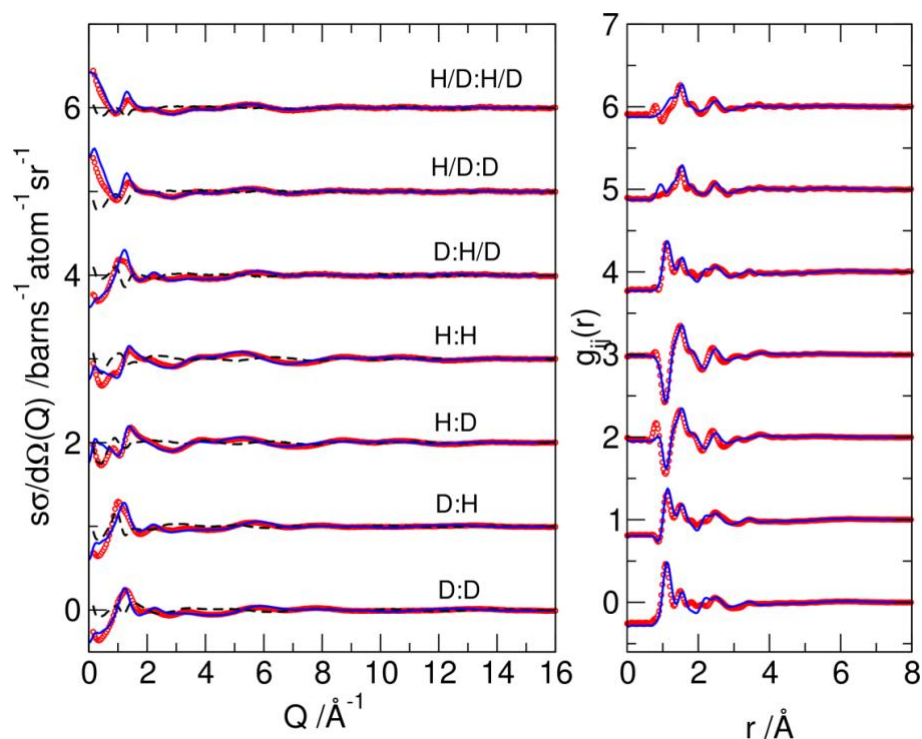


Figure 3.3-1: Structure factors for ChCl:Ur (top) and ChCl:Ox (bottom). For each DES, experimental (symbols) and EPSR modelled (solid) total structure factors (left) and transformations to real space (right) for the isotopically substituted liquid mixtures are shown. Residual differences between the experimental and simulated data are shown by the dashed lines. The curves have been shifted for clarity and are labelled with the isotopic composition of the ChCl:HBD components.

Choline–chloride and choline–choline RDFs for both DES show similar profiles, revealing an alternating lattice arrangement of charged ions that resembles the structure of

imidazolium chloride ionic liquids.²³³ In both DES, the choline–chloride RDF shows a single broad maximum for close contact correlations at 4.5–4.6 Å. This contrasts with the reported room temperature data for ChCl:Ur,¹³⁷ where a double peak feature (sharp maximum at *ca.* 4.0 Å and a broader shoulder around 5.2 Å) was reported. The peak at 4.0 Å was assigned to strong hydrogen-bonding choline–hydroxyl to chloride association and the longer distance component to association of chloride ions with the trimethylammonium region of the choline cation. These differences appear to indicate a merging of the two ambient temperature correlations with broadening due to the higher temperature lattice expansion.

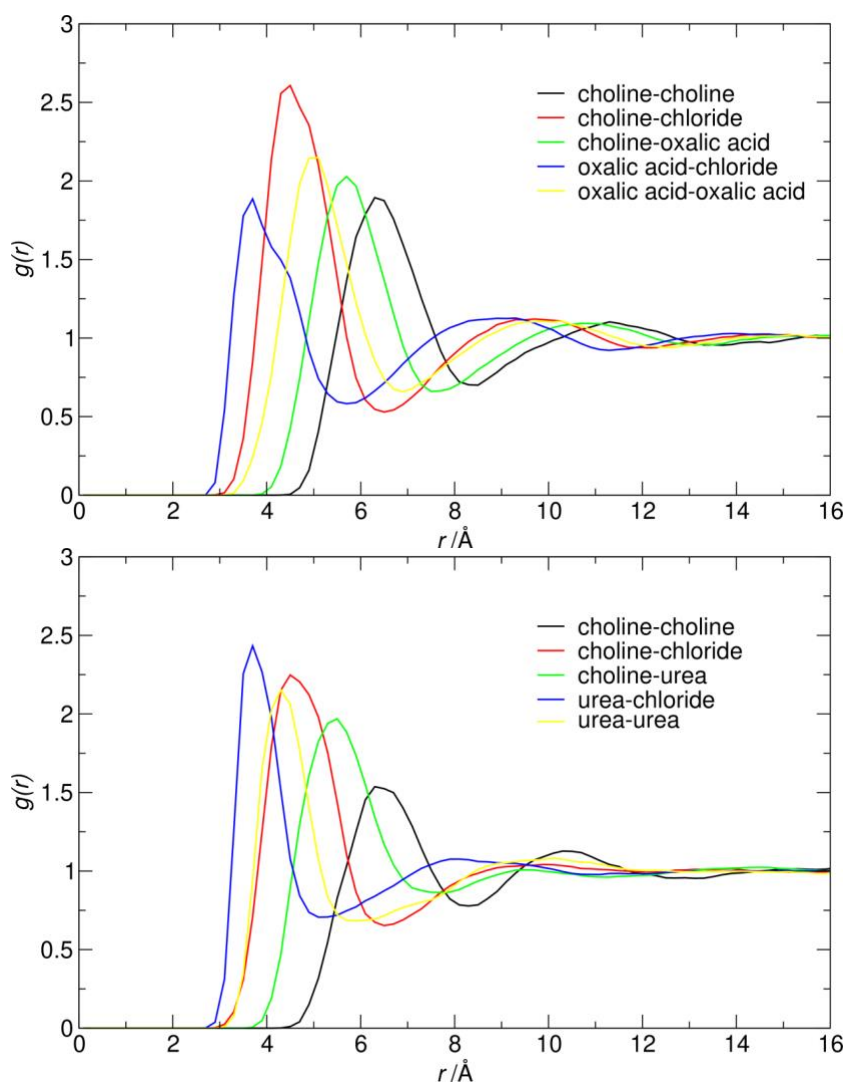


Figure 3.3-2: Centre of mass RDFs for ChCl:Ur (top) and ChCl:Ox (bottom).

Site-site partial radial distribution functions (pRDFs) were extracted from the EPSR refinements in order to further analyse the individual interactions. Principle correlations of

interest are shown in Figure 3.3-3 and Figure 3.3-4. The positions of the first peak (r_{\max}) in the pRDF and corresponding coordination numbers are shown in Table 3.3-2.

Table 3.3-1: Position of the first peak in the centre of mass RDFs for 3. Results from Ref. 137 for ChCl:Ur are shown in parentheses.

Pair	Peak Position /Å	
	ChCl:Ur	ChCl:Ox
Choline–Choline	6.4 (6.3)	6.3
Choline–Cl-	4.6 (4.2)	4.5
Choline–HBD	5.4 (5.5)	5.7
HBD–HBD	4.3 (4.4)	5.0
HBD–Cl-	3.7 (3.9)	3.7

3.3.1 Structure of ChCl:Ur DES

CE–CE and CE–Cl pRDF correlations (Figure 3.3-3 and Figure 3.3-4) have coordination numbers of 6.94 and 3.75 which are of the same order as 6.74 and 4.35 at 303 K, reported in a previous study.¹³⁷ These pRDFs correspond to the choline-choline and choline-chloride centre of mass (COM) RDFs in Figure 3.3-2 and indicate that the general liquid structure of the DES is retained as the temperature is increased. However, as with the choline-chloride COM RDF as noted above, the shapes of the Cl–N and Cl–CE peaks differ.

The N...Cl correlation appears as a peak at 4.7 Å (coordination number 2.40) with a small shoulder at 4.2 Å. This correlation distance is *ca.* 0.5 Å longer than that found by Hammond, Bowron, and Edler¹³⁷ at 303 K and the correlation length of 3.9 Å with a weaker shoulder at 4.8 Å determined from small cluster density functional theory (DFT) calculations.²¹⁹ The longer correlation length found here can be interpreted in terms of increased mobility of the choline cation, however the variations in the correlation profile can only be explained by an overall change in the orientational association between choline and chloride ions. The CE...Cl correlation has a pronounced bimodal distribution, with two peaks at 3.6 Å and 4.7–5.7 Å sitting either side of the N...Cl correlation. Similar profiles are present for all three C(x)...Cl correlations from choline to chloride with a first peak in the range 3.55–3.65 Å and corresponding H...Cl correlations at 2.8 Å.

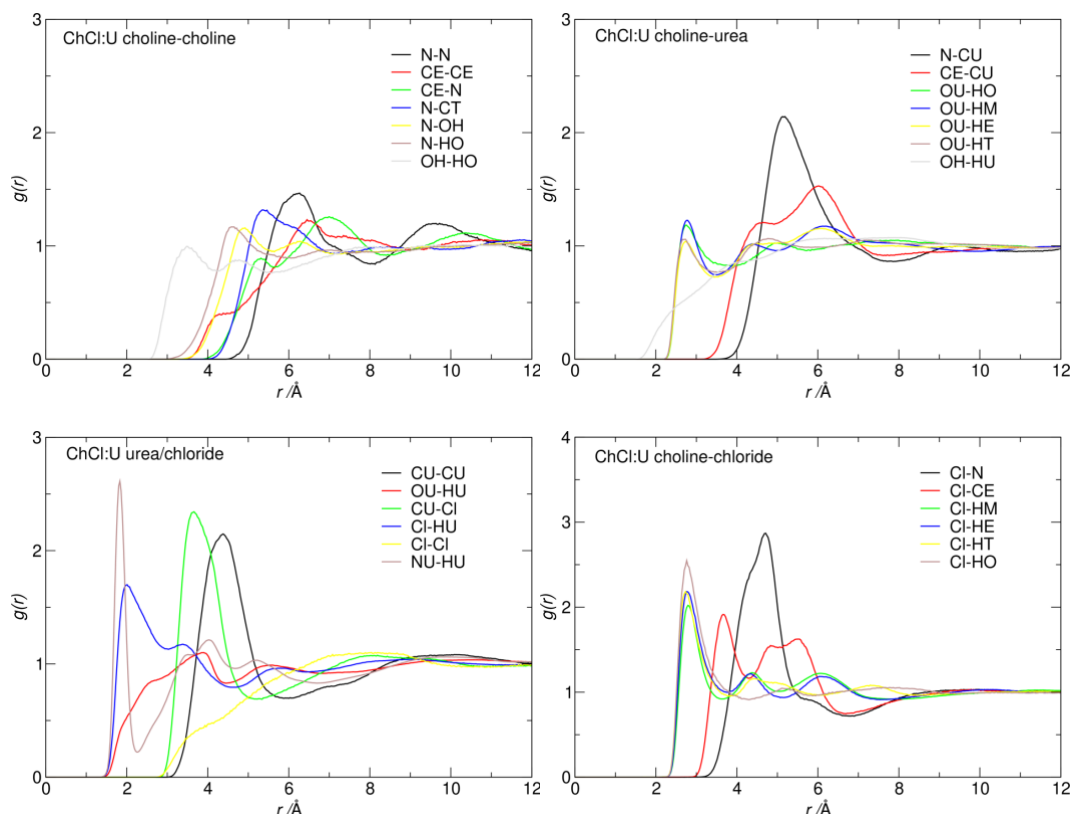


Figure 3.3-3: Atom-centred pRDFs for ChCl:Ur

Two different choline–chloride interaction motifs have been previously reported: strong hydrogen-bonding between the choline–hydroxyl group to chloride and Coulombic charge association of chloride ions with the trimethylammonium cation. Hammond, Bowron, and Edler¹³⁷ identified choline–hydroxyl to chloride association as a significant contributor to structural ordering at 303 K with the Cl...HO correlation distance (2.1 Å, coordination number 0.7) much shorter than that for –CH₃...Cl contacts between ions (observed at 2.8 Å). Stefanovic *et al.*²¹⁹ described correspondingly short Cl–HO distances from simulation, however Wagle, Deakynne, and Baker²²¹ found a longer correlation distance of 2.3 Å.

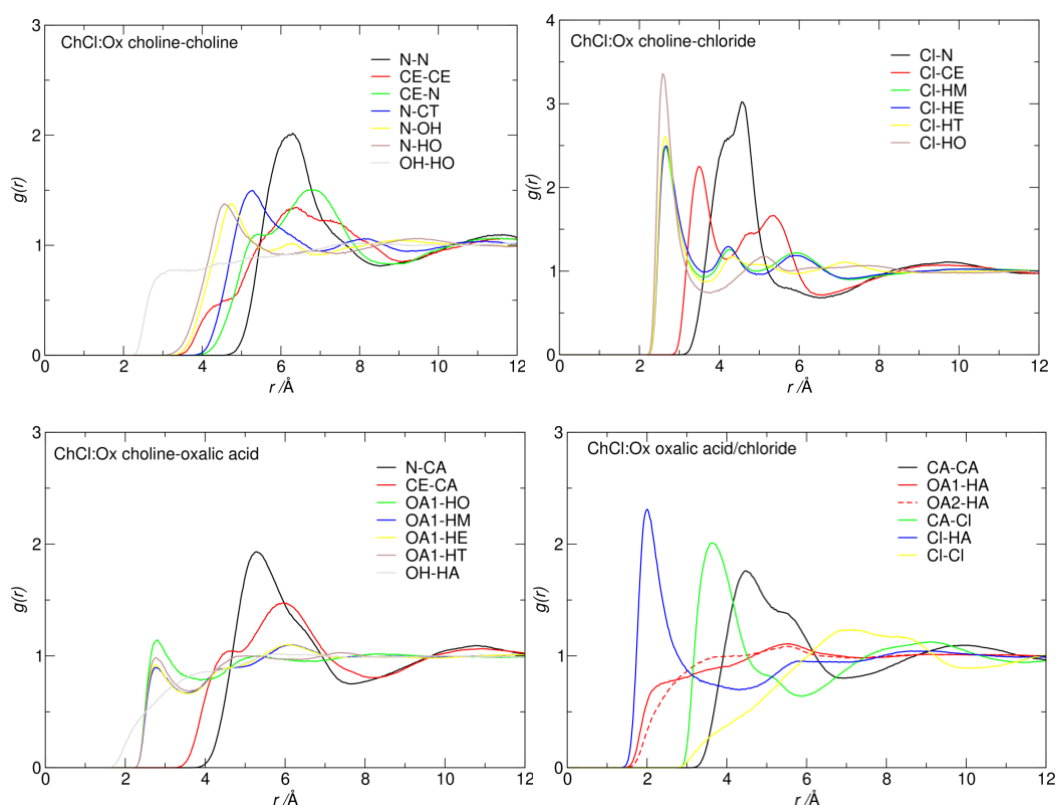


Figure 3.3-4: Atom-centred pRDFs for ChCl:Ox

From these EPSR results, the choline hydroxyl to chloride $\text{Cl}\cdots\text{HO}$ correlation at 338 K is present as a peak with a maximum at 2.8 Å (coordination number of 0.80 ± 0.84), comparable in length to all the other choline $\text{H}\cdots\text{Cl}$ correlations found at 2.9 Å. This is a significant lengthening of the $\text{Cl}\cdots\text{HO}$ correlation distance and indicates a weakening of this structure directing association. A second temperature effect is evident in the Ur–Ur (NU–HU) correlation, where the $\text{N}\cdots\text{H}\cdots\text{N}$ association occurs with a sharp, well defined peak at 1.8 Å ($N_{\text{coord}} = 1.98$). This is not present at 303 K where $\text{N}\cdots\text{H}\cdots\text{OU}$ Ur self-association modes are more dominant.

Table 3.3-2: Coordination numbers calculated for the principle partial RDFs shown in Figure 3.3-3 and Figure 3.3-4 for ChCl:Ur (1:2) and ChCl:Ox 1:1 DES. Mean coordination numbers N_{coord} were determined to the first minima (r_{min}) after the primary correlation peak (r_{max}) in the pRDF

pRDF	$r_{\max}(r_{\min}) / \text{\AA}$		pRDF	$r_{\min} / \text{\AA}$	
ChCl:Ur 1:2			ChCl:Ox 1:1		
Choline–Choline					
N–N	6.2 (8.2)	4.82±1.23		6.1 (8.2)	7.07±1.69
CE–CE	6.4 (9.0)	6.94±1.36		6.3 (9.0)	9.17±1.85
CE–N	5.4 (8.5)	6.69±1.34		5.4 (8.5)	8.68±1.77
N–CT	5.3 (7.0)	3.88±1.38		5.3 (7.0)	4.80±1.51
N–OH	4.9 (5.8)	2.26±1.02		4.8 (5.8)	2.78±1.11
N–HO	4.6 (6.0)	2.64±1.16		4.6 (6.0)	3.16±1.25
OH–HO	3.2 (4.0)	0.67±0.77		3.1 (4.0)	0.80±0.79
Choline-Chloride					
N–Cl	4.7 (5.5)	2.40±0.89		4.7 (5.5)	3.25±1.07
CE–Cl	3.7 (6.8)	3.75±1.00		3.6 (6.8)	4.73±1.21
Cl–HM	2.8 (4.0)	5.75±2.30		2.8 (4.0)	7.85±2.68
Cl–HE	2.8 (4.0)	1.36±1.25		2.8 (4.0)	1.85±1.23
Cl–HT	2.8 (4.0)	1.35±1.24		2.8 (4.0)	1.85±1.19
Cl–HO	2.8 (4.0)	0.80±0.84		2.8 (4.0)	0.92±0.71
Choline–Ur			Choline–Oxalic acid		
N–CU	5.2 (7.8)	10.88±1.94	N–CA	5.2 (7.7)	11.91±.75
N–NU	4.9 (7.5)	19.83±3.71	CE–CA	4.5 (8.2)	14.31±4.73
N–OU	4.7 (5.6)	9.12±2.35	OA1–HO	2.7 (4.0)	0.57±0.74
OU–HO	2.8 (4.0)	0.49±0.66	OA2–HO	2.7 (4.0)	0.59±0.72
OU–HM	2.8 (3.5)	2.75±1.65	OA1–HM	2.7 (4.0)	4.33±2.40
OU–HE	2.8 (3.5)	0.56±0.76	OA2–HM	2.7 (4.0)	4.15±2.33
OU–HT	2.8 (3.5)	0.58±0.82	OA1–HE	2.7 (4.0)	0.97±1.10
OH–HU	2.0 (4.0)	3.37±2.09	OA2–HE	2.7 (4.0)	0.93±1.08
			OA1–HT	2.7 (4.0)	0.93±1.06
			OA2–HT	2.7 (4.0)	0.98±1.06
			OH–HA	2.0 (4.0)	1.04±0.93
Ur–Chloride			Oxalic acid–Chloride		
CU–Cl	3.8 (5.2)	3.22±1.43	CA–Cl	3.3 (5.8)	4.72±2.55
NU–Cl	2.9 (5.8)	8.15±1.50	Cl–HA	2.0 (4.0)	1.67±1.15
HU–Cl	2.0 (4.0)	6.23±3.00	Cl–OA2	2.9 (5.8)	2.23±1.00
Ur–Ur			Oxalic acid–Oxalic acid		
CU–CU	4.5 (6.0)	4.54±1.71	CA–CA	4.5 (6.8)	9.75±3.38
HU–OU	2.9 (3.4)	6.36±1.82	OA1–HA	2.2 (4.0)	3.30±1.03
HU–NU	1.8 (2.3)	1.98±0.98	OA2–HA	3.5 (4.0)	2.18±1.21
			OA1–OA2	3.0 (4.0)	6.93±2.30
Chloride-Chloride					
Cl–Cl	7.5 (10)	10.05±2.77		6.7 (10)	11.73±2.00

Comparing with the literature, Stefanovic *et al.*²¹⁹ reported weaker, and fewer N–H...OU correlations and also a correspondingly larger coordination number for proximal N–H...Cl interactions than found by Hammond, Bowron, and Edler¹³⁷ in their EPSR analysis of

neutron scattering data. Ashworth *et al.*²²⁰ noted the importance of N–H...N hydrogen-bonding in ChCl:Ur, observing that N–H...N interactions are equal to the stronger of the two N–H...O associations in distorted hydrogen-bonded Ur chains. Araujo *et al.*²²³ suggested that Ur–Ur N–H...O interactions were not strengthened in ChCl:Ur, making the point that an increase in the (conventional) hydrogen-bonding interactions between Ur molecules would lead to an increase in melting point. However, they also propose the formation of a centrosymmetric Ur dimer, held by strong hydrogen bonds.

Together, the differences in the choline–OH...chloride and Ur N–H...N pRDFs suggest reorganisation in the liquid leading to a loss of the short distance choline hydroxyl to chloride correlations and a change in Ur–Ur self-association and loss of directional correlations between choline and both Cl⁻ and U.

3.3.2 Structure of ChCl:Ox DES

The ChCl:Ox DES was examined as a potential candidate for metal oxide dissolution, following work from Abbott and co-workers,⁴⁵ in order to examine the influence of changing the HBD component on the DES liquid structure.

Zahn, Kirchner, and Mollenhauer¹³⁰ studied the effects of HBD components on the magnitude of interactions in the DES by DFT modelling, predicting an increase in HBD...chloride hydrogen-bonding from Ur (through ethylene glycol) to oxalic acid as a HBD. This is supported by polarity studies²³⁴ that show DES containing hydroxyl-containing HBD donating components were more polar than those containing Ur.

The Choline C–H...Cl pRDF correlations in ChCl:Ox are shown in Figure 3.3-4. The first shell correlations all cluster around 2.7-2.8 Å, with the N–Cl correlation showing a maxima at 4.7 Å. These results are similar to those found for ChCl:Ur, underlining the similarities observed in the COM RDFs in Figure 3.3-2. In both DES, the N–Cl pRDF shows evidence of two overlapping peaks which reflect the two closest approaches of chloride to the N-centre via the N-ethyl and N-methyl substituents. The choline–OH...Cl correlation is also found with a maximum at 2.8 Å (coordination number 0.94), the same distance as that for the first peaks in the choline C–H...Cl pRDFs indicating that there is a significant reduction in the hydrogen-bonding interactions with the choline hydroxyl group at 338 K.

Similarly, choline–OH...oxalic acid association is only evident as a small shoulder at 3.2 Å (to a minimum at 4.1 Å) in the O1–OA2 correlation. Hydrogen-bonding between the choline hydroxyl site and oxalic acid can occur with either acid acting as the HBD. The HO...OA

correlations to both oxalic acid oxygen sites (choline as HBD) show a peak at 2.8 Å (coordination number *ca.* 0.6) whereas the HA...OH correlation (oxalic acid as HBD) has no distinct peak, but the contact starts from 1.7 Å. The coordination number, calculated to 4 Å to compare with that for the HO...OA correlations, is 1.0.

Strong association of the oxalic acid with chloride anions is evident from the peaks at 2.0 Å and 2.9 Å in the HA–Cl and Cl–OA pRDFs, respectively. This is comparable to the HBD–Cl pRDFs observed previously with peaks around 2.0–2.2 Å in ChCl:Ur and ChCl:Mal.^{137,217} The HA–Cl peak distance found is consistent with the value of 2.95 Å obtained from DFT calculations¹³⁰ and is slightly shorter than the corresponding ChCl:Ur Cl–NU correlation at 3.0 Å. The Cl...X separation (X = hetero-atoms of the HBD, N, or O) decreases from 3.35 Å in ChCl:Ur to 2.95 Å in ChCl:Ox while the choline–OH...Cl distance remained approximately constant at 3.1 Å (O...Cl). An increase in HBD–chloride hydrogen-bond strength on changing the DES components from Ur to polyols and carboxylic acids was also found from QENS²¹⁶ and is supported by polarity studies.²³⁴

Self-association of oxalic acid is evident from the peak at 5.0 Å in the COM RDF in Figure 3.3-2 and by O...O pRDF correlation peaks at 3.0 Å. site-site correlations are evident for the two homo-associations (OA1...OA1 and OA2...OA2) and the anticipated hetero OA1...OA2 association through hydrogen-bonding. One possibility is that the pRDFs incorporates elements of discrete acid–acid hydrogen-bonding and spatial proximity that occurs through interactions of oxalic acids with chloride anions. The OA2...HA acid–acid hydrogen bonding correlation starts at 1.5 Å and extending up to *ca.* 2.2 Å, however there is no distinct peak.

This contrasts with pure acetic and formic acid²³⁵ and also pyridine/acetic acid mixtures⁹⁸ where strong acid...acid hydrogen-bonding is observed. This suggests that a significant proportion of the pRDF represents proximal association rather than specific hydrogen-bonding correlations. In terms of the HBD–chloride and self-association (Ur–Ur or oxalic acid–oxalic acid), there are marked differences in the structure correlations between the two DES. Strong HBD–chloride correlations are apparent at 2.0 Å in both ChCl:Ur and ChCl:Ox. Although the position of these peaks are equivalent in both DES (contrasting with small reduction in separation predicted by Zahn, Kirchner, and Mollenhauer¹³⁰ from ChCl:Ur to ChCl:Ox), the peak is noticeably sharper in ChCl:Ox. The coordination numbers for chloride ions to either Ur–HU or oxalic acid–HA sites are 0.175 and 0.275, respectively, calculated to 2.5 Å, and 0.309 and 0.438 calculated to 3 Å, showing greater solvation of chloride by oxalic acid in ChCl:Ox than by Ur in ChCl:Ur. The hydrogen-bond

donor:chloride ratio in the two DES are 8:1 (ChCl:Ur) and 2:1 (ChCl:Ox) providing evidence for the highly correlated chloride–oxalic acid liquid structure.

3.3.3 Spatial density functions

Spatial density functions (SDFs) of choline, chloride, and either Ur or oxalic acid around both choline and Ur/oxalic acid centres in the two DES are shown in Figure 3.3-5. Both DES show comparable distributions of components around the choline cations using the molecular centres of mass as the point of reference. The choline-centred SDFs reveal that chloride has the closest interaction with choline, ordering at the contact distance (4.6–4.7 Å) with the highest correlation probability as a band around the hydroxyethyl-group. Further association at the same distance to the methyl-groups of the cation can also be seen. The isosurface is large and relatively diffuse covering a large proportion of the available space around choline through ion-ion interactions. The flexibility of the NCH₂CH₂OH group and the large conformational volume that this group can occupy through rotations mean that a detailed assessment of the spatial correlations is necessarily limited by the selection of the reference point for observation.

The Ur and oxalic acid SDFs around choline in the respective DES have similar profiles to those of chloride at slightly longer correlation distances (as indicated in the COM RDFs, Figure 3.3-2) with similar spatial distributions. The choline– choline solvation shell appears at larger distances and are also largely associated with the positions of the chloride (and HBD) in a band about the central choline, demonstrating the radially layering evident from the COM RDFs.

In contrast to the broad, diffuse SDFs around choline, the HBD centred SDFs in Figure 3.3-2 show much greater spatial organisation. The strong Ur...Cl association through the Ur proximal hydrogen positions in ChCl:Ur is anticipated given the role of Ur as an anion receptor.^{236,237} In contrast, Ur–Ur correlations appear through interactions with all four hydrogens. The strong HU–NU correlation in the pRDF (1.8 Å) and Ur–Ur SDF show development of amine– amine hydrogen-bonding networks rather than head-to-tail Ur stacking through association with the Ur–OU position. There is no evidence for correlation density associated with the OU position, at this moderately high probability 15% spatial density function, that would correspond to the NU–HU...OU associations.

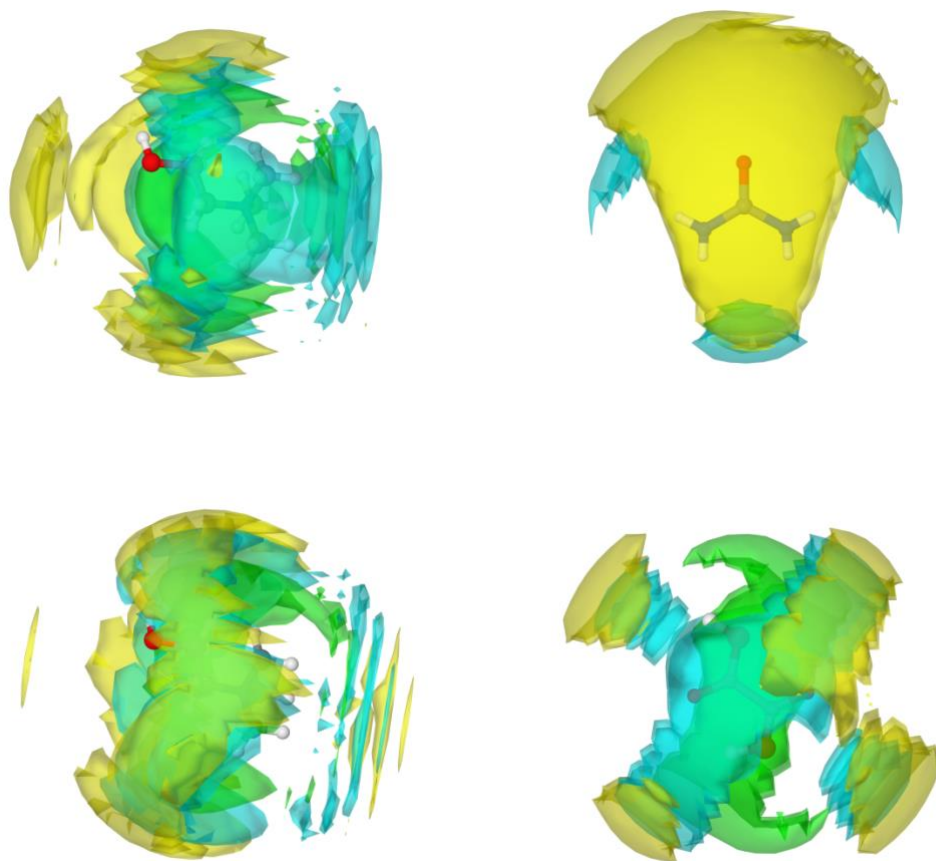


Figure 3.3-5: SHARM spatial probability maps for ChCl:Ur (top) and ChCl:Ox (bottom) showing the distributions around choline in the two systems (left) and Ur (top right) or oxalic acid (bottom right) of choline (yellow), chloride (green), and Ur or oxalic acid (cyan) calculated to encompass the first shell peaks from the COM RDFs in Figure 3.3-2. Surfaces were calculated to encompass the top 15% probability within the first peak in the COM RDF around the central molecule.

These chlorine–Ur and Ur–Ur spatial associations dominate the structure around Ur, with choline cations occupying the remaining vacant space over the Ur face and around the Ur carbonyl group that has a reduced HBA role than that found at 303 K where chloride is associated with both Ur distal and proximal hydrogen positions and Ur–Ur correlations were predominantly found associated with the distal N–H positions.

For ChCl:Ox, SDFs around oxalic acid (Figure 3.3-5) show a highly symmetric distribution forming a band around the CA–CA bond and, in the molecular plane, lobes extending from each –COOH function. The chloride SDF strong correlation as a band around the CA–CA bond with single-site hydrogen-bonding to the two carboxylic acid hydrogen sites (seen as

the vertically arranged lobes in Figure 3.3-5 and bridging “side-on” to the oxalic acid). Asymmetry present in the SDF profile may reflect limitations in the static EPSR reference potential since vibration spectroscopy shows that the two carboxylic acid O-sites are equivalent due to rapid hydrogen- exchange. Similarly, the oxalic acid–oxalic acid SDF presents a band of high correlation probability around the CA–CA bond (without the asymmetry lobes) and two lobes from each –COOH group. When SDFs are calculated using a larger probability sample (not shown) the lobes merge into two concentric bands bisecting the plane of the molecule. This distribution of states appears consistent with the large number of inter- and intra-molecular hydrogen-bonding modes and π - π stacking interactions possible in oxalic acid,²³⁸ with the most stable dimers containing two inter-molecular and three intramolecular hydrogen-bonds (Figure 3.3-6).

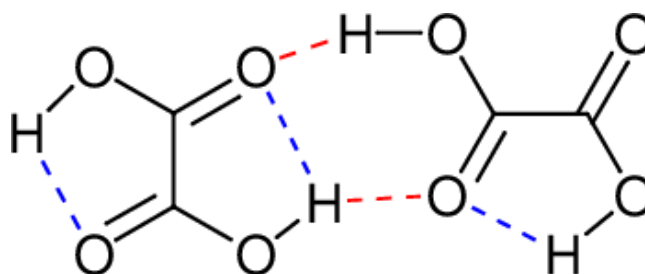


Figure 3.3-6: Schematic of the most favourable oxalic acid dimer hydrogen- bonding motif (after reference ²³⁸) with two inter-molecular hydrogen-bonds (red) and three intra-molecular hydrogen-bonds (blue) that generate the characteristic pattern in the oxalic acid–oxalic acid SDF.

The correlation band surrounding the CA–CA bond is common to both the oxalic acid–oxalic acid and oxalic acid–chloride SDFs and is composed of hydrogen-bonding from intra-molecularly-constrained oxalic acid hydrogen atoms to chloride (in the plane) and to presumably anion- π out-of-plane interactions. Terminal hydrogen-bonds between oxalic acid and chloride result in the asymmetric lobes, whereas the generation of two hydrogen bonds between oxalic acid pairs (each acid as an acceptor and a donor) leads to the linear correlation sites. The choline–oxalic acid SDF also maps to the oxalic acid–oxalic acid correlations, but at a longer separation distance due to the larger size of the cation. The largest structural association around the oxalic acid groups are those arising from purely inter-molecular COOH...Cl bonds producing the chloride-lobes that point to strong and persistent hydrogen-bonding.

Strong choline–OH...Cl hydrogen-bonding was reported as the dominant ordering interaction in ChCl:Mal₂₁₇ with hydrogen bonding to chloride from both the acid and alcohol sites

(coordination numbers 0.62 and 0.51, respectively) and the alcohol-OH...Cl as the preferred interaction at 303 K. In contrast, here at 338 K, with the loss of choline-OH correlations in the DES and the stronger HBD component, ChCl:Ox exhibits a more correlated structure. Charge delocalisation and transfer from chloride to oxalic acid¹³⁰ leads to the hydrogen bonding competition between oxalic acid-chloride and oxalic acid-oxalic acid. A common theme between ChCl:Ox (here) and ChCl:Mal is the presence of carboxylic acid molecules oriented radially in parallel with the long axis of a central acid. However, direct comparisons are hindered by the differences in pKa (1.23 for oxalic acid, 2.83 for malic acid) and the increased conformational flexibility and the presence of an additional -OH group in malic acid.

3.3.4 Validation of EPSR reference potential

The results obtained for ChCl:Ur show some significant differences in the specific site-site correlations present in the DES compared to the structure previously described at 303 K.¹³⁷ In particular, the key loss in choline-chloride structure and changes to the Ur-Ur correlations. It is important to ensure that this accurately reflects reasonable solutions constrained in the refinement by the experimental data rather than being perturbed or defined by the initial reference potential.

Hammond, Bowron, and Edler¹³⁷ used a model for their data refinement that differed from that here by the use of (i) integer ± 1 charges assigned to the N-centre of choline and the chloride anion and (ii) a relatively high +0.6 charge placed on the hydroxyl-hydrogen of choline in the EPSR reference potential. In this work, charge on choline was distributed over the four carbon centres attached to the N-atom and a smaller overall partial charge was assigned to the hydroxyl-group making it less acidic (see Table 3.2-2). To test whether these differences in the reference potential could lead to undesired bias in the final refinement, particularly generating potentially stronger HO-Cl interactions at shorter distances, we re-refined the ChCl:Ur data here using the earlier reference potential. After equilibration, the refined structure model obtained showed no change on either peak positions or coordination numbers associated with RDFs to the choline-OH sites, and we can conclude that the refinement is robust and that the losses in the specific site-site correlations with the choline-OH sites are due to increased thermal motion and, probably, rotation of the choline cation.

3.4 Conclusions for neat ChCl:Ur/ ChCl:Ox DESs

The key observation from the investigation of ChCl:Ur and ChCl:Ox DES at 338K is that the choline-hydroxyl group does not act as a structure directing site in the liquids. All the key

short-length associations of choline; choline–OH...Cl and self-association of choline cations through HO–OH hydrogen bonding, previously reported around 2.0 Å, extended to 2.8 Å (HO...Cl) and 3.0 Å (HO...OH).

Changing the EPSR reference potential to match that from previous studies at 303 K^{137,217} did not produce a better refinement fit, and consequently we can conclude that the models generated are equally consistent with the experimental data at these moderately elevated temperatures and describe liquid structure in both ChCl:Ur and ChCl:Ox DES, in which the choline–OH group plays a more or less prominent role as either a hydrogen-bond donor or acceptor compared to that previously reported at 303 K.

An alternative explanation that the DES all consistently contain water that was not considered in the modelling and could interfere with choline–OH...anion hydrogen bonding is inconsistent with both the physical behaviour of the DES samples (melting points) and the good match of neutron scattering cross section to the anticipated material compositions. Moreover, it has been reported that addition of 1 mole of water in ChCl:Ur DES²³⁹ produced a strengthening of the choline–OH...H₂N hydrogen-bonding interaction in contrast to the reduction in interactions observed here as the temperature is increased.

DFT modelling of ChCl-containing DES with Ur, ethylene glycol, and glycerol, by Stefanovic *et al.*²¹⁹ have shown that correlations between the choline ammonium-charge centre to the HBD (characterised by a broad correlation around 4 Å) and HBD...Cl interactions (around 2.0 Å) were dominant structural features. They also concluded that choline–OH...Cl hydrogen bonding was less pronounced than HBD...Cl hydrogen bonding (consistent with Wagle, Baker, and Mamontov²¹⁶) and that this, therefore, is not a key structural interaction. The systematic loss of short-range (and by implication, strong) choline–OH to chloride correlations in both ChCl:Ur and ChCl:Ox studied here at 338 K is most likely a result of increasing rotational mobility of the choline cation which becomes increasingly a spectator cation as the temperature increases. As such, the hydroxyl group in choline does not appear to be a key structural feature for DES formation, which is consistent with the observation that DES can be readily formed with many symmetric organic salts.¹¹⁸

3.5 ChCl:Ox with dissolved metal oxides

Following the investigations of the neat ChCl:Ur and ChCl:Ox DES, experiments were conducted to probe changes in structure of ChCl:Ox (Figure 3.5-1) and the coordination

environments in the presence of dissolved metal oxides. ZnO and Fe₃O₄ were chosen for investigation due to reports in the literature that both metal oxides could be dissolved into the oxalate DES at relatively high concentrations, especially ZnO.^{177,179,183} The study aimed to establish the speciation of the metal ions dissolved at the high concentration of 0.3M in the DES.

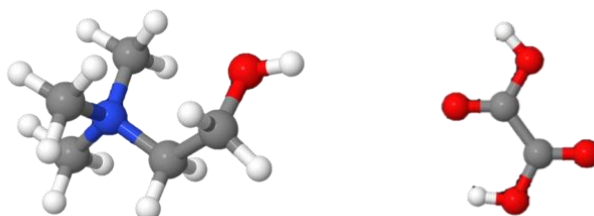


Figure 3.5-1: Stick and ball models of choline (left) and oxalic acid (right)

3.5.1 Experimental

3.5.1.1 Sample preparation

To prepare the dissolved metal oxide solutions, appropriate amounts of ZnO or Fe₃O₄ were added to approximately 3 g of the ChCl:Ox DES in a 25 cm³ round bottom flask which was subsequently stoppered to prepare approximately 0.3M solutions of the metal oxide dissolved in the ChCl:Ox. The mixture was heated at 40 °C for 24 hours, stirring at 500 RPM and then the samples were removed from the heatplate. The samples were placed in 5 cm³ screw cap vials which were closed and sealed with parafilm.

3.5.1.2 Neutron scattering

Experimental data sets were collected at ISIS on the SANDALS beam-line using the methods previously described in chapter 3.2. Data was collected for two independent samples with each metal oxide using protiated materials or deuteriated (methyl-deuterated choline-D₉ and oxalic acid-D₂) giving the following 4 samples; choline-D₉ chloride + oxalic acid-D₂ + ZnO (approximate molar ratio:1:1:0.3), choline-H chloride + oxalic acid-H + ZnO (1:1:0.3), choline-D₉ chloride + oxalic acid-D₂ + Fe₃O₄ (1:1:0.3) and choline-H chloride + oxalic acid-H + Fe₃O₄ (1:1:0.3). The ChCl:Ox used was the same as described in chapter 3.2, ZnO was purchased from Sigma Aldrich (>99% purity).

Data was collected at 75 °C, in $\text{Ti}_{0.68}\text{Zr}_{0.32}$ flat plate cells with internal geometries of $1 \times 35 \times 35$ mm, with a wall thickness of 1 mm. Data was reduced in GUDRUN, calculating self-consistent densities (atoms \AA^{-3}) from averaged differential scattering cross sections (DCS) and sample compositions. For the ZnO containing samples, the calculated density was 1.2 g cm^{-3} (protiated) and for the sample with Fe_3O_4 dissolved, was 1.75 g cm^{-3} (protiated).

Experimental sample compositions (ratio of number of each atom type in the different components in the system), densities and scattering cross sections measured are shown in Table 3.5-1.

Table 3.5-1: Experimental sample compositions, densities and scattering cross sections

		+ZnO		+Fe ₃ O ₄	
		protiated	deuteriated	Protiated	deuteriated
Choline chloride	C	5	5	5	5
	H	14	H ₅ D ₉	14	H ₅ D ₉
	N	1	1	1	1
	O	1	1	1	1
	Cl	1	1	1	1
oxalic acid	C	2	2	2	2
	H	2	D ₂	2	D ₂
	O	4	4	4	4
metal oxide	Zn	0.3	0.3	Fe	0.9
	O	0.3	0.3		1.2
Density /g cm ⁻³		1.20	1.25	1.75	1.75
Atomic density /atoms \AA^{-3}		0.0870327	0.0870327	0.113094	0.109059
Average merged differential scattering cross section /b sr ⁻¹ atom ⁻¹		3.63385	1.38628	3.67378	1.42105
Percentage of expected level /%		99.6	91.1	104.5	95.8

In order to try to analyse the data, two potential models for the zinc(II) speciation after dissolution of ZnO in the DES were considered in which acidic dissolution would produce anionic zincate(II) species as either (i) chlorozincate(II) and (ii) oxalatozincate(II) anions, produced by initial reaction of zinc oxide with the acidic oxalic acid protons, producing $\text{Zn}_{2+(\text{DES})}$ ions and water, followed by coordination with respectively, either chlorides or oxalates.

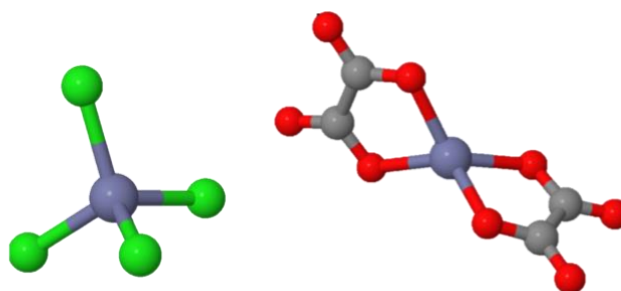


Figure 3.5-2: Ball and stick model of tetrahedral chlorozincate (left) and di(oxalato)zincate (right) anion.

These are discussed below.

3.5.1.3 The chlorozincate(II) model

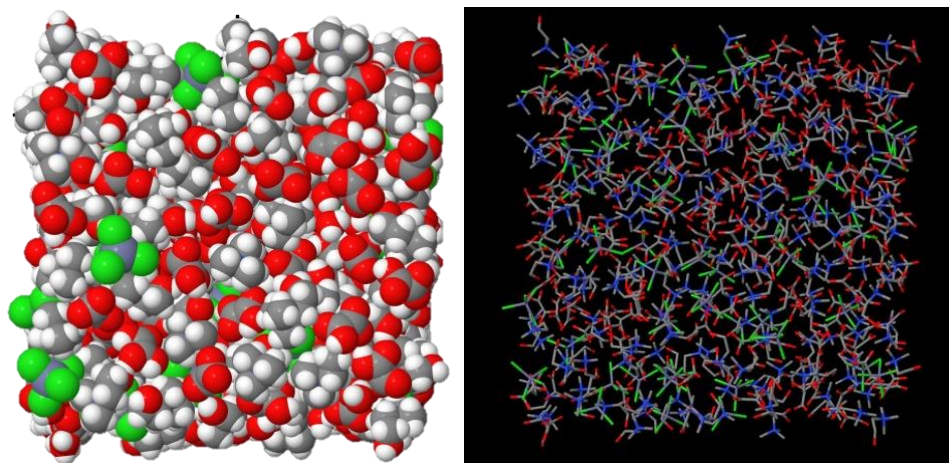


Figure 3.5-3: Chlorozincate simulation with 450 components in a 38.85 Å box.

The tetrachlorozincate(II) model was produced with 450 components in box of dimensions 38.85 Å (Figure 3.5-3) The model constituted of 5 different types of components derived from $\text{ChCl}/\text{oxalic acid}$ (1:1) + 0.25 ZnO reaction $4[\text{Ch}]_+ + [\text{ZnCl}_4]_{2-} + 1.\text{water} + 2[\text{oxalic}]$

acid/oxalates] with 4 ‘oxalate’ fragments, two as free acid and two as deprotonated oxalate anions):

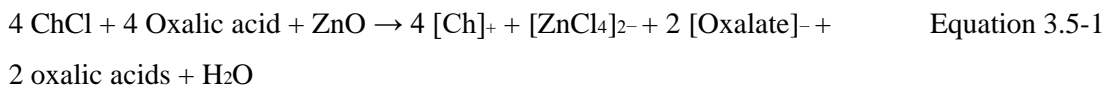


Table 3.5-2: : Lennard-Jones (ϵ and σ) and charge (q) parameters used for the reference potential of the Empirical Potential Structure Refinement model for both plausible ZnO speciation modes derived from the literature, and OPLS-AA.

Atom label	type	ϵ /kJ mol ⁻¹	σ /Å	Charge q/e
N1	N	0.71111	3.2500	0.035500
C1	C	0.27608	3.5000	-0.18677
C2	C	0.27608	3.5000	-0.13090
HM	H	0.12549	2.5000	0.13763
C3	C	0.27608	3.5000	-0.031900
H1	H	0.12549	2.5000	0.13763
O1	O	0.71111	3.0700	-0.34650
H2	H	0.00000	0.0000	0.24460
Zn1	Zn	0.80000	3.200	0.55940
Cl1	Cl	0.80000	3.200	-0.63980
OW1	O	0.65000	3.100	-0.38250
HW1	H	0.00000	0.0000	0.19130
CO1	C	0.29281	3.550	0.30380
OO1	O	0.87843	2.960	-0.49660
OO2	O	0.71111	3.120	-0.31190
HO1	H	0.00000	0.0000	0.19410

Table 3.5-3: Intramolecular bond distance (Å) and bond-angle (°) constraints used to define the basic structure of the components in the initial EPSR simulation model for the ChCl:Ox Des with dissolved ZnO. Oxalic acid was fixed to a planar conformation by defining O-C-C-O dihedral restraints.

Bond lengths	/Å	Bond angles	/°
choline			
N1 C1	1.49430		
N1 C2	1.50641		
C1 HM	1.12263		
C2 C3	1.53085		

C2 H1	1.12801
C3 O1	1.41302
C3 H1	1.12397
O1 H2	0.96683

ZnCl₄

Zn1 Cl	2.29540	Cl-Zn-Cl angle	109.5
--------	---------	----------------	-------

Oxalate/oxalic acid

CO1 OO1	1.22850	OO1-CO1-OO2	116.6
CO1	1.50382	CO1-CO1-OO1	126.3
CO1 OO2	1.35327	CO1-CO1-OO2	117.2
OO2 HO1	0.97363	OO1-CO1-CO1-OO1	dihedral 180

Models were refined against the experimental data over the full data range ($Q = 0.1\text{--}50 \text{ \AA}^{-1}$). Within the EPSR simulation, initial potentials and interatomic distance constraints used to define the basic molecular geometries were obtained from MOPAC with the AM1 model. Atom types were defined in the same manner as used for the neat liquid models (Figure 3.2-2), whilst full rotational flexibility was also enabled. The forcefield parameters (ϵ and σ) and charge (q) of the reference potential used are given in Table 3.5-2, along with interatomic distances and bond angles used to define the basic model geometries are provided in Table 3.5-3.

3.5.1.4 Oxalatozincate model

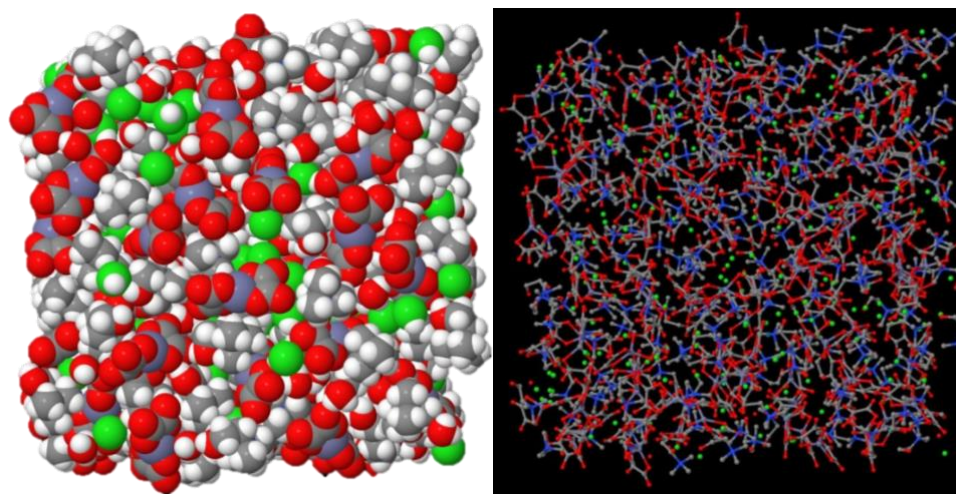
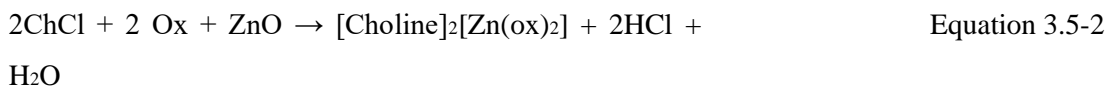


Figure 3.5-4: Oxalatozincate simulation box with 600 components in a 40.70 Å.

The oxalatozincate simulation consisted of 600 components in a 40.70 Å box (Figure 3.5-4), with 4 different types of components present $2[\text{Ch}]^+ + [\text{Zn}(\text{Ox})_2]^{2-} + 2\text{HCl} + \text{H}_2\text{O}$, which were derived from the dissolution and speciation shown in Equation 3.5-2.



The simulation box contained 200 $[\text{Ch}]^+$, 100 $[\text{Zn}(\text{Ox})_2]$, 200 HCl and 100 H_2O . The model was developed using a higher mole fraction of zinc (2:1 to DES, $\chi_{\text{Zn}} = 0.3$) compared to the 4:1 ($\chi_{\text{Zn}} = 0.2$) mix from the chlorozincate model. Additional forcefield parameters (ϵ and σ) and charge (q) of the reference potential and the interatomic distances and bond angles used to define the basic molecular geometry of the $[\text{Zn}(\text{Ox})_2]^{2-}$ are provided in Table 3.5-4 and Table 3.5-5 respectively.

Table 3.5-4: Starting potential parameters for bisoxalatozincate anion for EPSR refinement

atom	Element type	ϵ /kJ mol ⁻¹	σ /Å	Charge q/e
CO1	C	0.80000	3.7000	0.28797
OO1	O	0.65000	3.1000	-0.45960
OO2	O	0.65000	3.1000	-0.49800
Zn1	Zn	0.80000	3.2000	0.67830

Table 3.5-5: Geometry definitions for bisoxalatozincate anion

Bond	/Å	Bond angle	/°
CO1 OO1	1.25020	OO1-CO1-OO2	118.5
CO1 OO2	1.30829	CO1-CO1-OO1	123.00087
CO1	1.53378	OO2-Zn1-OO2	82.68988
OO2 Zn1	2.10687		

3.5.2 Results and discussion

3.5.2.1 Zinc oxide

The aim of the study was to elucidate the speciation of the dissolved metal oxides in the ChCl:Ox DES by using a multi-technique approach. Starting with vibrational spectroscopy (Raman) to probe the local metal environment. Electrospray-MS experiments were then conducted on the ChCl:Ox with dissolved metal oxide, with the aim of detecting and identifying ions corresponding to fragments of the metal centre with coordinated DES species. Finally, to look at the bulk liquid structure liquid-phase neutron diffraction with H/D isotopic substitution and EPSR analysis was conducted to see if any plausible speciation modes could be determined. The results from the techniques are discussed in this section.

3.5.2.2 Spectroscopy

Vibrational spectroscopy – Raman spectra were collected for the DES and the DES containing dissolved ZnO. A screen of chlorozincate/dioxalatozincate bands was then conducted to provide evidence for presence of one or the other (given that chlorozincate speciation will have ‘free’ oxalate anions in the DES, the principle objective here is to try to identify whether any peaks that can be assigned to Zn-X stretches and do they seem most reasonable for Zn-Cl or Zn-O, which given their relative positions in the periodic table might not be too different. In Figure 3.5-5 a peak is observed in the ChCl:Ox with ZnO sample (black) at 285 cm^{-1} , which is not present in the neat DES (red). Literature studies of chlorozincates would suggest that this is not dissimilar to the wavenumber of $[\text{ZnCl}_4]^-$ (275-278 cm^{-1}) in the $[\text{C}_8\text{mimCl}]\text{Cl}/\text{ZnCl}_2$.¹³⁵ This is a possible clue that the dissolution pathway favours chlorozincate formation.

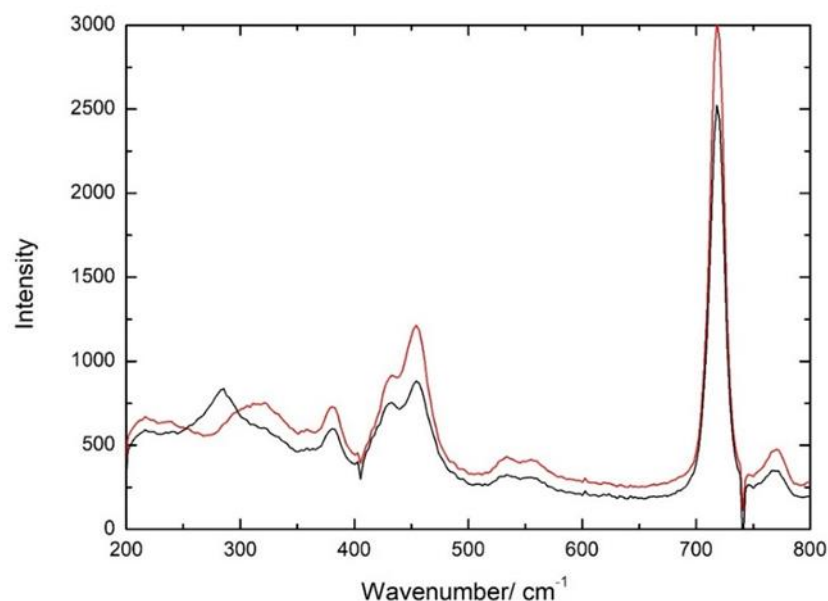


Figure 3.5-5: Raman spectra of ChCl:Ox (red) and ChCl:Ox with dissolved ZnO (black)

Literature about the Raman spectroscopy of oxalatozincate species, was found to date back to the 1960s.²⁴⁰ However, due to the technically limited capabilities of Raman spectrometers of the time, data collection was restricted in the low frequency region of the vibrational spectrum, to wavenumbers greater than 500 cm^{-1} . Hence, whether oxalatozinc species also show a peak in Raman spectra around 280 cm^{-1} could not be confirmed. Therefore, the Raman data collected for the sample is inconclusive given the similarities of position of chlorine and oxygen in the periodic table and Raman spectral data for oxalatozincates not being collected for wavenumbers $<500 \text{ cm}^{-1}$.

Electrospray ionization (ESI) mass spectrometry

Mass spectroscopy has been used to determine metal ion speciation in ionic liquids.^{135,177} The DES containing dissolved metal oxide were examined using ESI mass spectroscopy. Measurements were taken by dissolving small amounts of the DES:metal oxide in methanol and introducing this diluted sample into the Waters Xevo G2-XS Q TOF Mass Spectrometer, the data produced for ESI(+) and ESI(-) can be found in Appendix 2. The ESI(+) shows the presence of the [choline+] at 104 m/z confirming that DES has been detected, however any fragments likely related to the dissolved metal oxide were expected to be found in the ESI(-). The ESI(-) revealed that the [oxalate]⁻ was present at 89 m/z , the largest peak in the ESI(-) scan was found at 282 m/z , this did not however correspond to the known speciation modes for either chlorozincate,¹³⁵ oxalatozincate species²⁴⁰ or plausible mixed

oxalate/chlorozincates. Small peaks are seen between 165-175 m/z this ties in with the values reported by Estager *et al.*¹³⁵ for chlorozincate speciation in ionic liquids, however, given the small size of these peaks these could only be assigned as chlorozincate species in the DES with a low degree of confidence.

The ambiguous results given by ESI mass spectrometry may have been due to the sample being analysed in methanol and that preferential methanol based speciation modes for the ZnO were being observed. Fast atom bombardment mass spectrometry may be a more useful technique for determining the speciation

3.5.2.3 Neutron diffraction

Experimental scattering data from the ChCl:Ox-H/H and ChCl:Ox-D/D DES samples after dissolving zinc oxide are shown in (i) Q -space (inverse Angstrom scattering and (ii) transformed to d -space (\AA) in Figure 3.5-6. The scattering data, $S(Q)$, shows diffraction characteristic of liquids with only small fluctuations in the scattering levels and, transformed to d -space, no sharp diffraction peaks from crystalline material are evident. Hence, dissolution of the zinc oxide in the DES is demonstrated, confirming that the zinc oxide was not present as a dispersion in the DES.

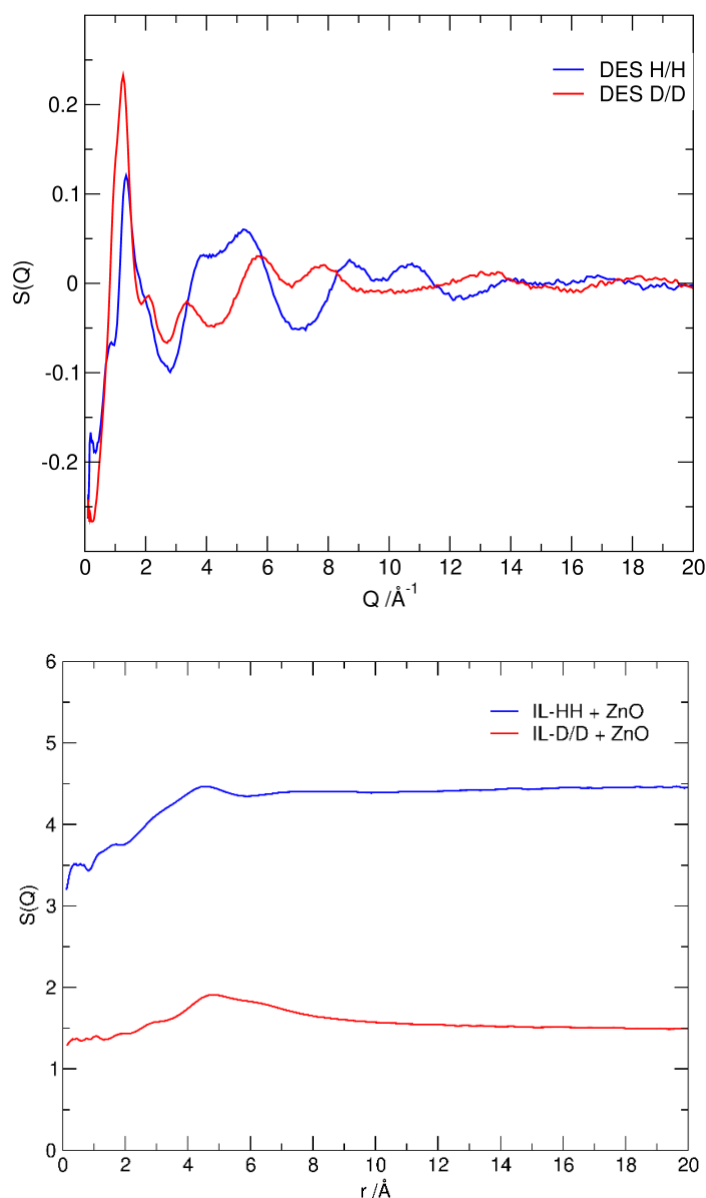
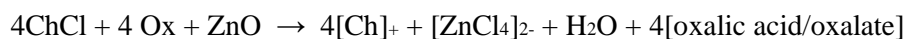


Figure 3.5-6: $S(Q)$ neutron scattering profiles from ChCl-oxalic acid DES containing dissolved ZnO (Top) and the corresponding transformation of $S(Q)$ scattering into d -space (Angstrom) from ChCl-oxalic acid DES containing dissolved ZnO showing the absence of Bragg diffraction peaks that would signify the presence of crystalline solid particles.

Examination of the experimental scattering data, $S(Q)$, shows that the zinc oxide has been dissolved in the DES rather than forming a dispersion of zinc oxide crystalline nanoparticles which would result in a signature in the scattering pattern of sharp Bragg peaks from diffraction from the crystallite lattice. A number of speciation models were proposed as extremes of plausible zinc speciation in the DES following acid assisted dissolution, with

either formation of chlorozincate(II).^{179,180} or oxalatozincate²⁴⁰ anions as shown in Figure 3.5-2

The two proposed equations for speciation of zinc in the DES to generate (i) chlorozincate(II) ($[\text{ZnCl}_4]^{2-}$) and (ii) di(oxalato)zincate(II) ($[\text{Zn}(\text{Ox})_2]^{2-}$) anions based on acid-driven dissolution followed by complexation of the dissolved Zn(II) species by chloride or oxalate are:



It is worth noting that the possible formation of trigonal $[\text{ZnCl}_3]^-$ was not considered as there is now a substantial body of evidence demonstrating that this species is **never formed** in ionic liquid solutions.^{41,135}

3.5.2.4 Chlorozincate model

Simulations were allowed to equilibrate for at least 2500 cycles before applying the empirical potential, then were iterated up to 14,000 cycles. The plot refinement energy and internal pressure of the chlorozincate model (Figure 3.5-7) show that the system is both effectively equilibrated and that the low refinement energy and low internal model pressure indicate that it is also stable.

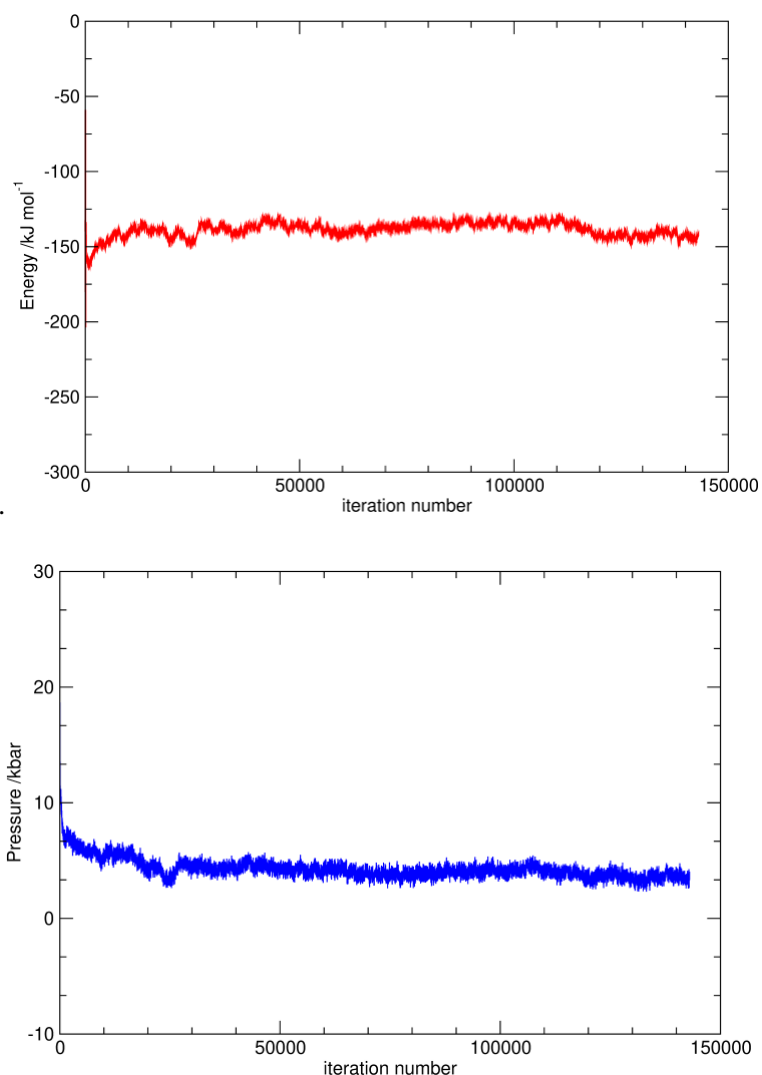


Figure 3.5-7: Plot of refinement energy as a function of iteration number for the chlorozincate EPSR model, showing the stability of the equilibrated simulation (top) Corresponding plot of chlorozincate simulation model internal pressure (bottom).

The fitted and experimental structure factors, $F(Q)$, for the chlorozincate system modelled by EPSR are shown in (Figure 3.5-8). The fitted model (dashed lines) shows a reasonably good correlation with the experimental data (solid lines), especially for the protiated sample (IL-H/H + ZnO). The deuteriated system (IL-D/D + ZnO) shows a higher level of divergence at low Q , whilst in the 5-12 \AA^{-1} range there is also more structure in the EPSR model than experimental data.

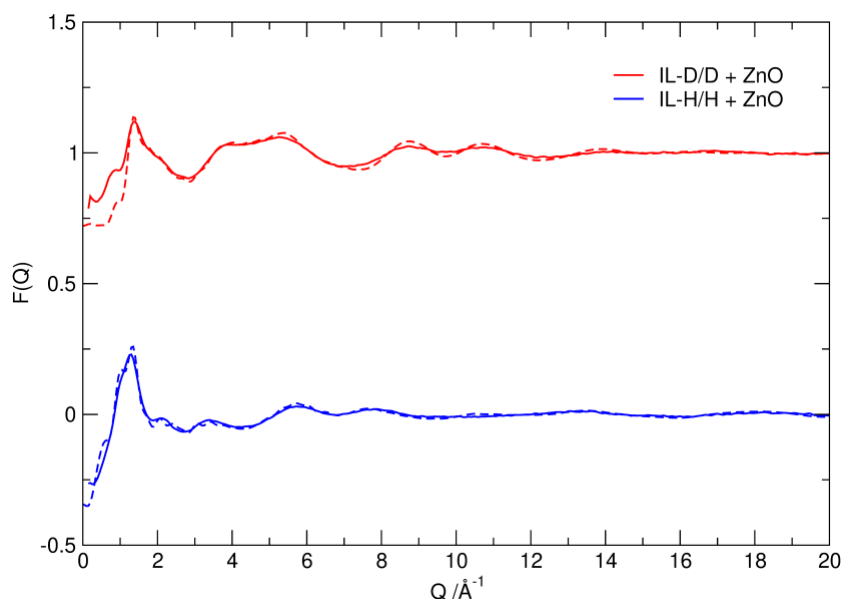


Figure 3.5-8: Comparison of $F(Q)$ scattering correlations between the normalised model (dashed lines) and experimental data (solid lines) for the chlorozincate model of the $\text{ChCl}:\text{Ox} + \text{ZnO}$ DES, showing the relatively good fit to the two data sets with the model:

Once the structural factor $F(Q)$ was converted into real space $f(r)$ (Figure 3.5-9) the over-structuring of the ESPR models become more apparent particularly in the distance correlation of 2-4 Å. This over-structuring indicates that the model is too rigid and inflexible which could potentially be remedied by increasing the temperature in the model simulation.

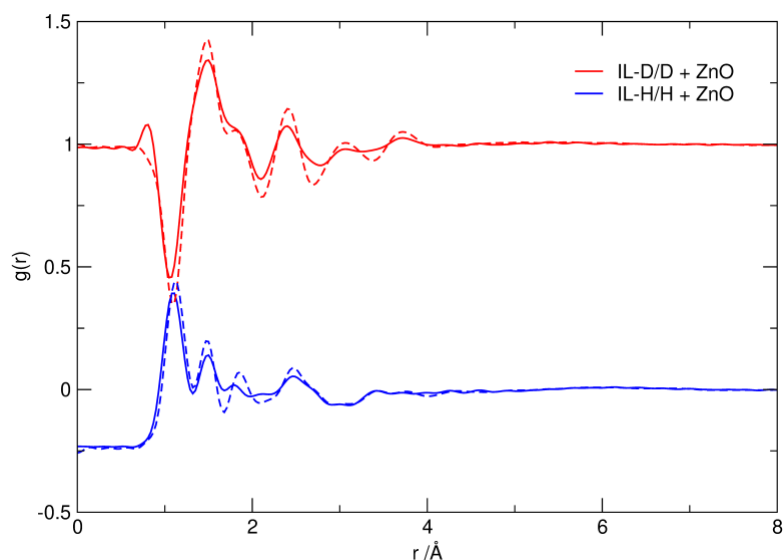


Figure 3.5-9: Comparison of $f(r)$ distance correlations between the normalised model (dashed lines) and experimental data (solid lines) for the chlorozincate model of the $\text{ChCl}:\text{Ox} + \text{ZnO}$ DES, showing a reasonable correlation of the model with the experimental data.

The Centre of Mass (COM) radial distribution functions between the DES components and chlorozincate ions from the ESPR model are shown in Figure 3.5-10. The first shell choline-zincate (cation-anion) and choline-oxalate (cation-anion) association are observed at 4.8 Å. The second shell choline-choline correlation is at 6-7 Å. The zincate anions show a large, defined correlation centred at 8 Å, indicating that this model for the DES has a strong structural correlation.

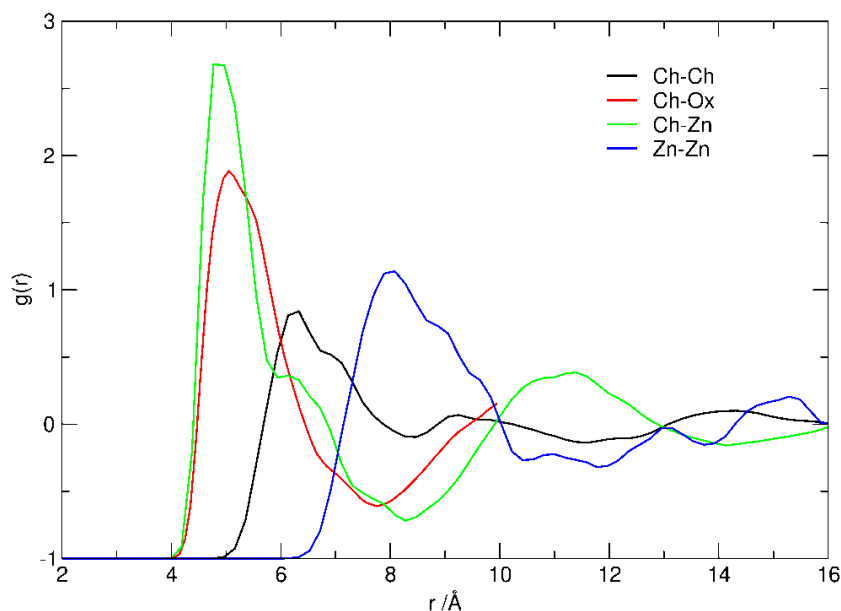


Figure 3.5-10: Centre of Mass (COM) radial distribution functions (average species separations) between choline cations and chlorozincate anions in the EPSR model, showing the first shell choline-zincate (cation-anion) and choline-oxalate (cation-anion) associations at 4.8 Å. These are followed by second shell choline-choline (cation-cation) correlation at 6-7 Å. The zincate anions show a large, defined correlation centred at 8 Å, indicating that this model for the DES has a strong structural correlation.

3.5.2.5 Oxalatozincate model

In analogy to the chlorozincate model, simulations were allowed to equilibrate for at least 2500 cycles before applying the empirical potential, and then were iterated up to 25,000 cycles. Increased cycles were required in order to try and reduce and stabilise the refinement energy in the model, contrastingly internal pressure of the model was found to be low and stable throughout the iterations as seen in Figure 3.5-11.

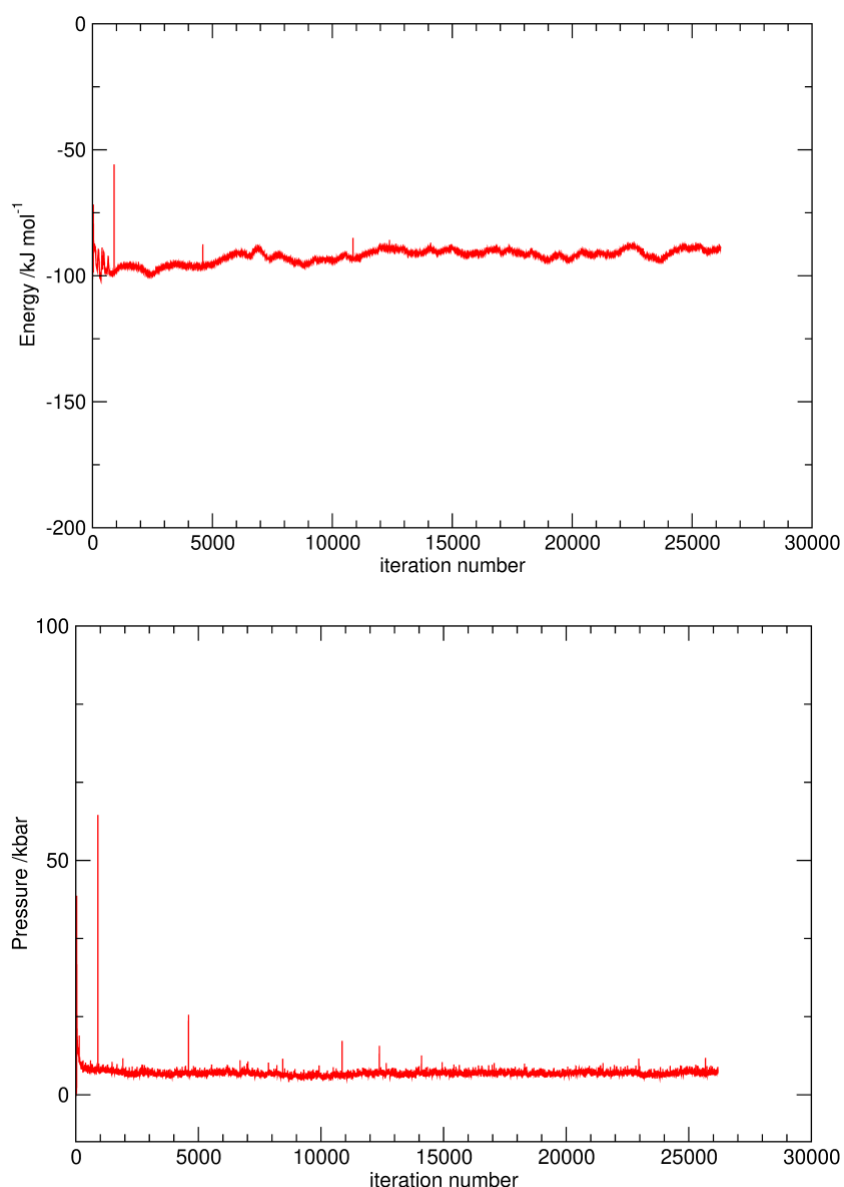


Figure 3.5-11: Simulation internal energy (top) and pressure plots (bottom).

The calculated structure factors, $F(Q)$, for the fitted EPSR model (dashed lines) are compared to the experimental data sets (solid lines) in Figure 3.5-12 and show a reasonable fit for the protiated sample (IL-HH + ZnO) with slight divergence between 3-6 \AA^{-1} . In the deuteriated sample (IL-DD + ZnO) greater divergence is observed, specifically at low Q and in the 7-14 \AA^{-1} .

Comparable to the results for the chlorozincate model once the total structural factors had been transformed into real space $f(r)$ (Figure 3.5-13), the difference in the experimental data (dashed) and EPSR model data becomes more pronounced, specifically in 3-5 \AA region.

Comparing the two models, the chlorozincate model gives a marginally better fit to the experimental data.

The COM radial distribution functions for the oxalatozincate EPSR model (Figure 3.5-14) show that the first shell choline-zinc association at 4.8 Å which is the same value as the choline-zincate (cation-anion) association in the chlorozincate model (Figure 3.5-10). The second shell choline-choline (cation-cation) correlation is present between 6-7 Å. Finally, given that the zincate-zincate (anion-anion) first correlation is exceptionally broad and in the range of 8-12 Å, we can deduce that there is no self-assembly or aggregation of the zincate anions in this model.

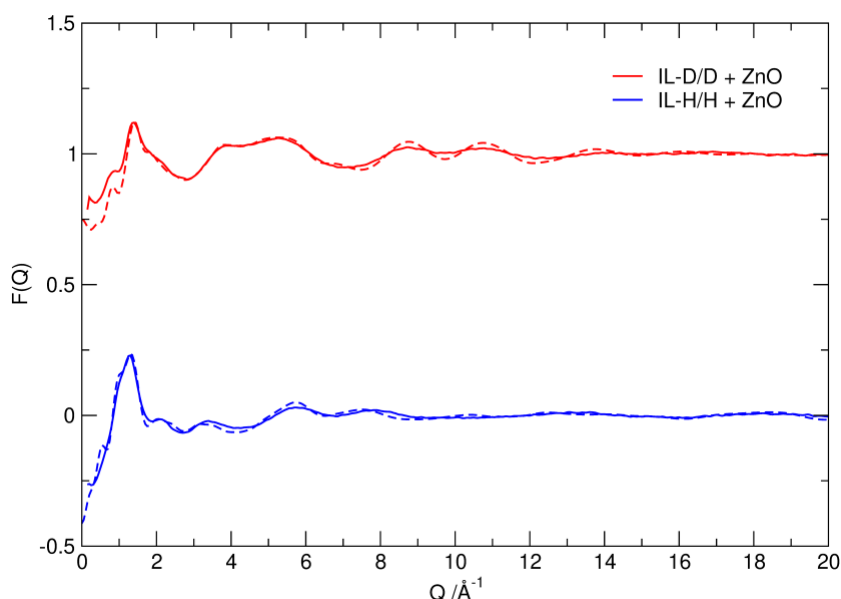


Figure 3.5-12: Comparison of $F(Q)$ scattering correlations between the normalised model and experimental data for the di(oxalato)zincate model, showing the relatively good fit to the two data sets with the model.

In summary, in both models, the experimental data (solid lines) was less structured than the model (dashed lines) seen in the $f(r)$ plots. Indicating that both models are too confined or rigid, which as stated, could be addressed by increasing the simulation temperature, but also suggests that despite reasonable fitting to the limited experimental data available, fail to capture accurately the coordination structure within the liquids. This is also apparent in the $F(Q)$ scattering plots where there is too much structure in the region between $Q = 8-12 \text{ Å}^{-1}$. Since these parts of the data correspond to a combination of intra- and intermolecular structure contributions, this could of course be an indication that the model is not correct for the data, but that this is the best correspondence we'll ever get.

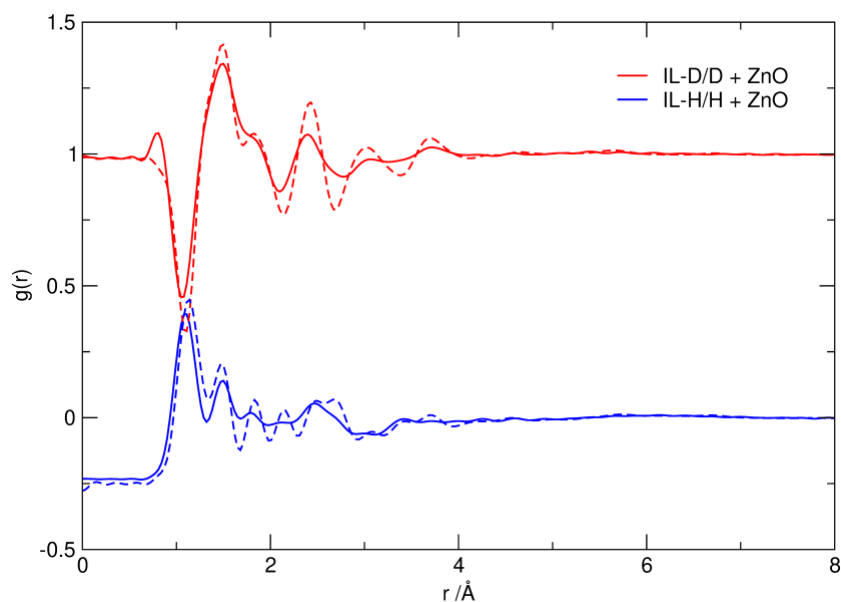


Figure 3.5-13: Comparison of $f(r)$ distance correlations between the normalised model and experimental data for bisoxalatozincate model, showing a reasonable correlation of the model with the experimental data.

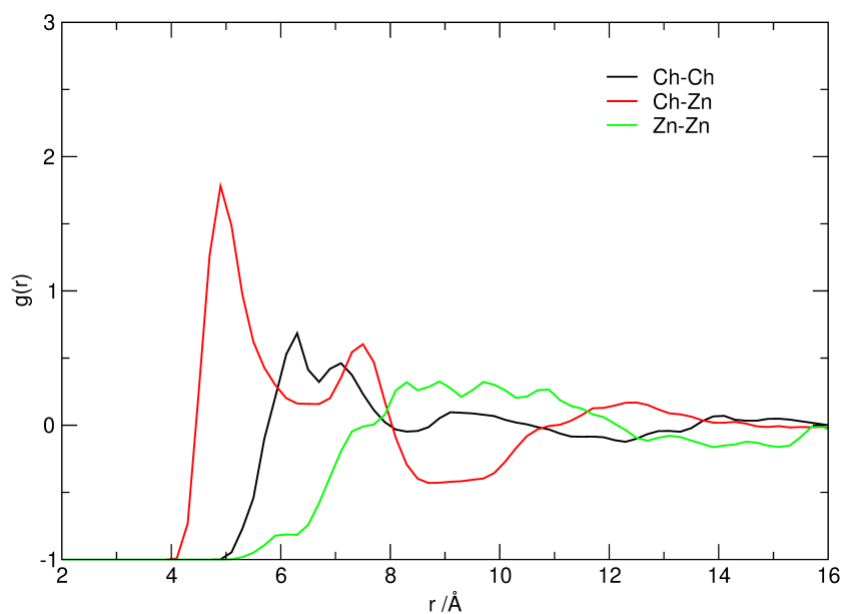


Figure 3.5-14: Centre of Mass (COM) radial distribution functions (average species separations) between choline cations and oxalatozincate anions in the EPSR model.

Attempts to fit the experimental EPSR data using two plausible modules based on different coordination and speciation at the dissolved zinc centres in the DES were made with chloride or with oxalate coordinating to the metal. Both potential anionic species are well characterised in different systems, for example chlorozincate ionic liquids^{41,135} and in oxalatozincate solution state spectroscopy²⁴⁰. Unfortunately, both proposed models – which are based on rational dissolution pathways and coordination chemistry – generated

simulation results that were equally as good as solutions to the limited number of neutron data sets that were collected. It is possible that additional data sets utilising additional H/D-substitution could help with the reliability of the fitting (self-consistent fit to multiple sets of data), however given that the coordination environment of the metal is deficient in hydrogens, this is unlikely to help advance the total structure model sufficiently.

3.5.2.6 Iron oxide

The experimental data sets were collected for the ChCl:Ox H:H and D:D samples containing dissolved Fe₃O₄, after GUDRUN data reduction the S(Q) was plotted for the samples as shown in Figure 3.5-15.

As can be seen, the data shows only small scattering fluctuations, as anticipated for a solution. From this, a first conclusion can be drawn that the iron oxide is not dispersed in the DES as nanoparticles, which are characterised by sharp crystallite diffraction peaks²⁴¹ with corresponding spacings (d values) of the diffraction peaks of 2.968 (220), 2.535 (311), 2.103 (400), 1.719 (422), 1.614 (511), 1.478 (440), and 1.271 (533). Plotting the neutron scattering DCS data in real space (see Figure 3.5-16) confirms the absence of diffraction peaks corresponding to any crystalline nanoparticles.

Further modelling of the liquid structure of this DES was not attempted due to the difficulty in proposing of reasonable ionic species for the complex stoichiometry. Given that technique was not able to elucidate the ZnO in DES speciation which appeared to be a much simpler system it was decided that it was not possible to take the speciation of Fe₃O₄ in DES any further.

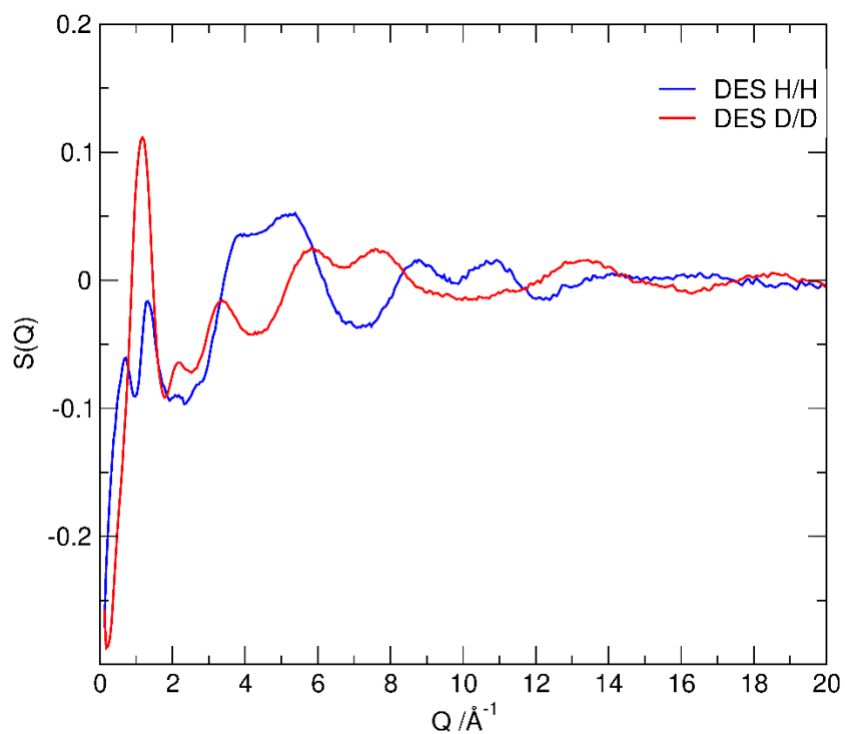


Figure 3.5-15: $S(Q)$ scattering from ChCl/oxalic acid DES with dissolved Fe_3O_4 , for the protiated DES (blue) and the deuterated DES (red).

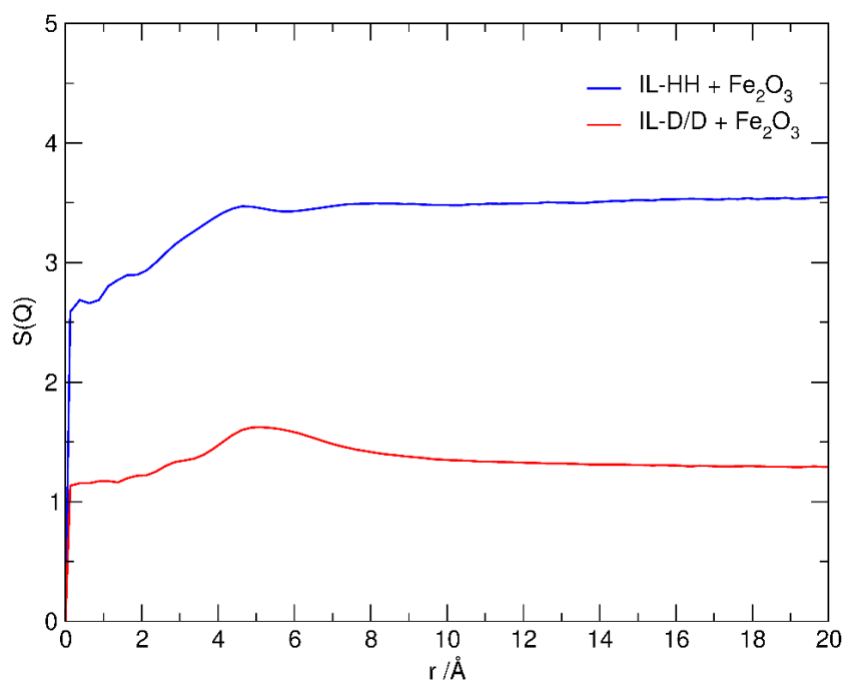


Figure 3.5-16: FT of scattering data into d-space (\AA) from ChCl/oxalic acid DES with dissolved Fe_3O_4 . No evidence of diffraction peaks from Fe_3O_4 nanoparticles are evident in the data.

4 SCREENING STUDY OF DES

A number of potential DES-forming mixtures were examined as part of the work to develop additional, new DES for metal ion dissolution and separation. The selection of components was driven by potential interest in applications for soft acid metal complexation, and by efforts to explore systematic changes in bonding and eutectic formation that could lead to more informed design of next generations of eutectic solvents. Given that the purpose of this piece of work was to rapidly identify and assess potentially interesting mixtures for further study, the rigorous procedures for drying of DES components were not adhered to, and compounds were used in as-received state for screening.

4.1 ChCl:imidazole

The ChCl:Ur DES has shown it has the ability to dissolve metal oxides, especially zinc oxide.¹⁷⁷ This was initially attributed to the complementary nature of the borderline Lewis base/Lewis acid relationship between the *N*-donor in Ur and the Zn_{2+} of the ZnO as explained by Hard Soft Acid Base theory (HSAB).²⁴² Motivated by studying an alternative DES with an *N*-donor, imidazole (Im) was selected as the HBD to be combined with ChCl. This compound was chosen for a number of reasons: (i) Im forms the backbone of the cation in many of the common ionic liquids,^{36,55,56} (ii) biological systems in nature show us that imidazole is extremely effective at coordinating to Zn_{2+} , *viz.* histidine “zinc fingers”,²⁴³ for example, (iii) further potential applications beyond zinc dissolution (imidazolium-based ionic liquids have been shown to be effective for absorption and activation of CO_2 ,¹⁶¹ for which Im-DES could be potentially used).

It has been reported that ChCl:imidazole (ChCl:Im) mixtures form a eutectic at a 3:7 ratio with a melting point of 56 °C.²⁴⁴ However, only limited experimental data was published. In order to more fully understand the phase behaviour of this DES system, and to collect data for comparison with the comparator tetraalkylammonium imidazolate ionic liquids, the melting point phase diagram of the ChCl:Im system was investigated using differential scanning calorimetry.

The ChCl:Im mixtures were prepared using the most common procedure found in the literature, by intimately mixing and then heating mixtures of the two components together at 80-100 °C until a homogenous liquid forms.⁴⁵ However, a number of problems were encountered. At high mole fraction, imidazole sublimed during the heating process resulting uncontrollable composition changes. Conversely, when ChCl was the main component

present, it remained an unreacted solid as heating at 80-100 °C is insufficient to completely melt the mixture reducing the interaction between the two components. Both these observations lead to mixtures with uneven distributions of imidazole and ChCl at the two extremes of the composition space. Nevertheless, a DSC scan for each of the mixtures was conducted (5 °C min⁻¹) and the melting points taken from the DSC data were recorded and plotted to determine if any significant trend for melting point depression could be observed. The phase diagram in Figure 4.1-1 shows that when ChCl was the component in excess a thermal event at around 80 °C (thermal event 2) was present corresponding to the α -ChCl to β -ChCl polymorph transition described in 2.3.2 of this work. Upon the decrease of the ChCl molar fraction this peak in the DSC scan began to decrease in size, however the temperature at which the peak was present stayed relatively constant, as expected. When the Im molar fraction was increased a peak in the DSC scan indicated melting at 56 °C as shown by thermal event 1 in Figure 4.1-1. This increased proportionally to the increase in the concentration of Im present in the mixture. Similarly, to thermal event 2 observed around 80 °C, the temperature at which the peak was present remained largely unaffected by changes in composition of the mixture. The enthalpy of the thermal event 1 was large, as an example it measured 91 J g⁻¹ for $\chi_{\text{ChCl}} = 0.2$ ChCl:Im sample therefore it is caused by a bulk amount of the sample and not an impurity. Unlike ChCl, imidazole is not known to have different polymorphs under ambient pressure,²⁴⁵ ruling this out as a possible cause.

Given the lack of evidence for a significantly depressed eutectic melting peak or glass transition in the DSC scans and observations that across all compositions the samples remained solids to temperatures above 70 °C the work was not proceeded any further as there was not a significant depression from the T_m of pure imidazole (90 °C). Therefore, the advantages to forming these mixtures were not clear.

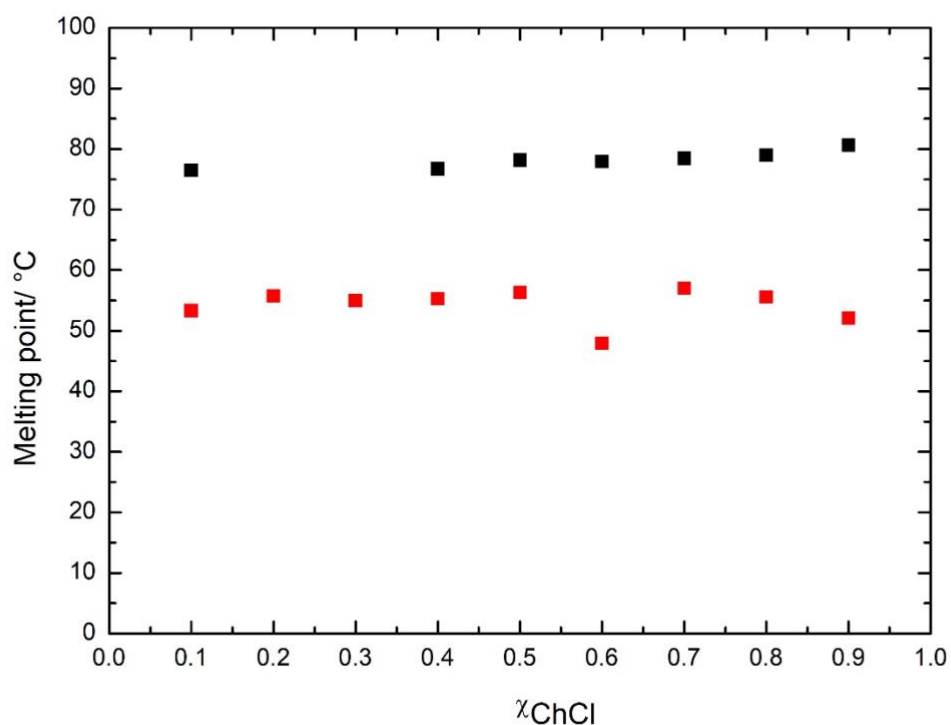


Figure 4.1-1: Phase diagram showing molar fraction of choline chloride (χ_{ChCl}) relative to thermal event temperature (°C) for the ChCl:Im system. Thermal event 1 (■) occurs between 45-60 °C and thermal event 2 (■) at approximately 80 °C.

4.2 DES containing thioureas

This study looked to probe the phase behaviour of the sulfur based analogue of urea, thiourea (Figure 4.2-1) in mixtures with ChCl. In parallel a further study was carried out on the ureas and thioureas shown in Figure 4.2-1 to determine the influence of the hydrogen bond donor sites availability on ureas/thioureas ability to form a DES with ChCl.

A deep eutectic solvent that contains sulfur in its structure could potentially be useful for metal solubilisation. Similarly to the rationale for forming imidazole DES, thiols and thiones are soft Lewis bases²⁴² and therefore favour interactions with softer metals e.g. Hg^{2+} . Consequently, DES incorporating S-based components rather than the corresponding O-based components (i.e. thiourea in contrast to Ur etc) could increase the probability of an interaction between the DES and a similarly soft metal. Expanding the potential number of target metals for an interaction with DES. The first sulfur containing deep eutectic solvent

that was prepared was 1:2 ChCl:thiourea (ChCl:Tu). This was taken as a logical starting point; thiourea is the sulfur containing analogue of Ur and therefore has the potential to display similar properties leading to successful eutectic formation and this system had previously been reported by Abbott *et al.*¹¹⁵

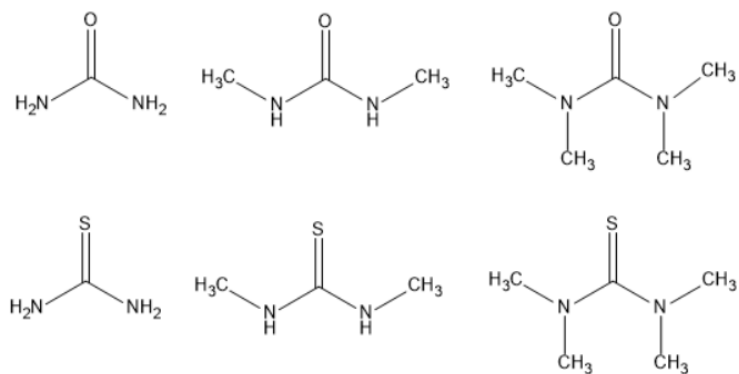


Figure 4.2-1: Chemical structure of studied molecules top left to bottom right: urea, 1,3 dimethylurea, tetramethylurea, thiourea, 1,3 dimethylthiourea and tetramethylthiourea

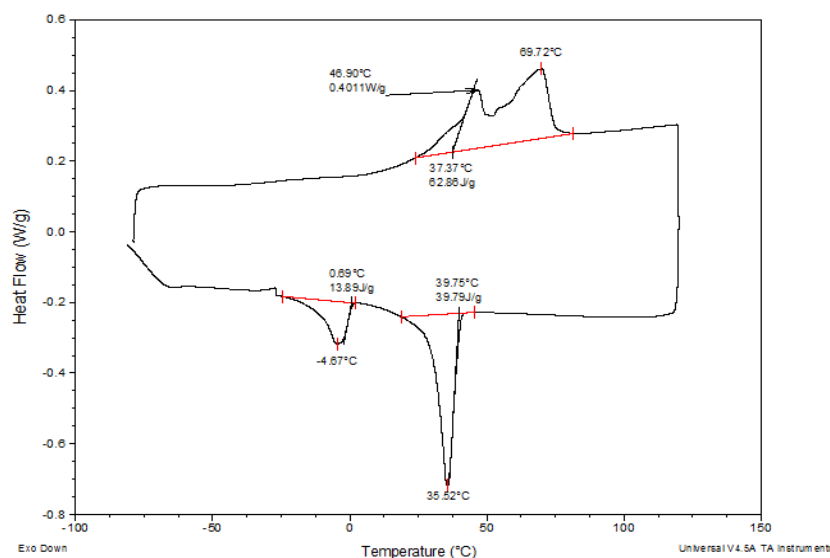


Figure 4.2-2: DSC thermogram for 1:2 ChCl:thiourea

Formation of 1:2 ChCl:Tu was a straightforward procedure, the two components were heated to 80°C and after 30 minutes a colourless liquid had formed, upon cooling to room temperature a white solid was left in the flask. DSC was conducted on the sample (Figure 4.2-2) and revealed two broad overlapping melting points one at 46.9 °C and one at 69.7 °C.

This indicates that the melting points for the components have been significantly depressed by a minimum of 110 °C as neither thiourea (T_m 182 °C) or ChCl (T_m 306 °C) would melt in their pure forms at the low temperatures present. Both melting transitions are reversible, with comparable, but supercooled exothermic transitions at 35.52 °C and -4.67 °C on cooling, it is possible that the peak present at 69.7 °C is caused by the α -ChCl to β -ChCl polymorph transition but is at a lower temperature than reported in chapter 2. The thermal behaviour of this 1:2 ChCl:Tu DES is markedly different to that of the corresponding ChCl:Ur DES where only a single glass transition is observed the temperature of the 1st order transition.

Compared to the ‘classical’ ChCl:Ur DES, ChCl:thiourea systems did not yield as large depressions in the freezing points of the components and do not form room temperature liquids at a 1:2 ChCl:Tu molar ratio. This is a desirable quality as it reduces energy usage as a heating process to keep the deep eutectic solvents in the liquid phase would not be needed. 1,3-Dimethyl-2-thiourea was selected as the next component for the formation of a sulfur containing deep eutectic solvent. The melting point of 1,3-dimethyl-2-thiourea (60 °C) is markedly lower than that of thiourea. It was anticipated that formation of eutectic compositions with ChCl would lead to room temperature liquids because suppression of the 1,3-dimethyl-2-thiourea melting point by only 35 °C is needed to achieve this goal. However, an expected trade off due to methylation of the nitrogen atoms of the Tu is that the ability of 1,3-dimethyl-2-thiourea to form hydrogen bonded networks as a HBD site is likely to be reduced due to replacement of two from four hydrogens with methyl groups.

The mixture of ChCl and 1,3-dimethyl-2-thiourea (1:2) was heated at 80 °C for 30 minutes and formed a straw coloured liquid which remained a liquid after being cooled to 4 °C (in the fridge) for 2 hours. After cooling however, the viscosity was noted to have increased markedly. Interestingly it was found that the 1:2 ChCl:DMT had no crystallisation points across the whole temperature range (Figure 4.2-3) and that only when temperatures as low as -60 °C that an amorphous solid began to form.

The sample had a T_g at -60 °C, as the vitrified solid began to flow. This example has shown that the replacement of hydrogen groups on Tu with methyl groups, hence reducing the amount of hydrogen bond donating groups within the molecule (4 to 2) can have a significant effect on the ability to form a DES and on the resultant properties deep eutectic solvent but importantly did not inhibit liquefaction.

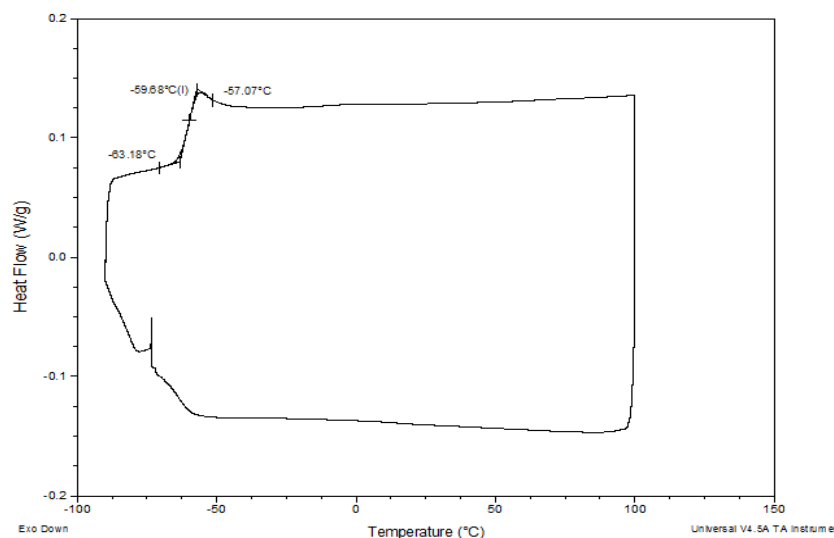


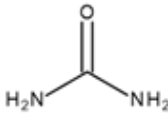
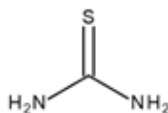
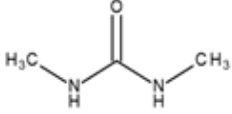
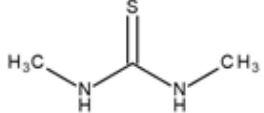
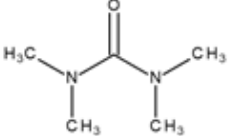
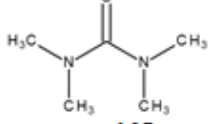
Figure 4.2-3: DSC thermogram for 1:2 ChCl:DMT

Encouraged by this finding modification of hydrogen-bond donor components of DES by N-alkylation, in the case of Urs and thioureas was studied as it was likely to lead to a range of new DESs with intermediate and tunable properties, and can be applied to other systems to allow access to room temperature deep eutectic solvents while incorporating useful functionalities into the DES for roles in metal coordination (for example, adding S-sites for soft metal coordination).

A systematic study of the influence of N-alkylation on Ur/thiourea components of ChCl DES was made, exploring with the changes in magnitude and directionality of hydrogen-bonding and the relative influences of substitution on T_m suppression as a route to achieving DES with desirable (low) melting points and viscosities.

While eutectic formation had been carried out using the substituted Urs and ChCl,²⁴⁶ the substituted thioureas/ChCl systems were yet to be studied and fully characterised. The eutectic point (if any) and the depression in T_m from the starting materials were calculated initially using DSC, followed by a more comprehensive phase diagram construction using POM. This allowed comparisons to be drawn between the two sets of systems in an attempt to determine the importance of the hydrogen bond donating groups on Ur and thiourea for the formation of eutectics with ChCl. The HBDs studied are set out in Table 4.2-1.

Table 4.2-1: HBD ureas/thioureas with associated melting point °C for the pure components (left) and eutectic formation comment and melting point when in a 1:2 ChCl:HBD mixture (right).

Component	Eutectic formation
 mp 134 °C	Yes mp 28 °C (crystalline)
 mp 175 °C	Yes mp 47 °C (crystalline)
 mp 102 °C	Yes mp 40 °C (crystalline)
 mp 63 °C	Yes Room temperature liquid (glass)
 mp -1 °C	No eutectic formation
 mp 76 °C	No eutectic formation

The components that were added to ChCl, as previously discussed were urea/thiourea and their di-substituted and tetra-substituted analogues (Table 4.2-1). Urea was chosen as it has been the most studied hydrogen bond donor to form eutectics with ChCl and most attempts have been made to describe this bonding.^{130,131,137} While some of these components had previously been looked at for the formation of eutectics,¹¹⁵ a systematic study had not yet been conducted to determine how substitution of these hydrogen donations sites on urea with methyl groups affected the formation of the eutectic, i.e. did the species still form a depressed melting point homogenous liquid and how did it affect the long term stability of the eutectic i.e. did the eutectic remain a liquid or did a component in the mixture precipitate out. All original systems studied were made at the 1 ChCl: 2 Ur/Tu molar ratio as this was claimed to be the ratio that gave the largest depression for the systems.¹¹⁵

The mixtures were initially heated together for 30 minutes at 80 °C, DSC experiments were then carried out on the samples (3 scans, -60-100 °C, 5°C min⁻¹) to determine a melting point.

Assessing the data in Table 4.2-1 we see that only the urea/thiourea and their di-substituted analogues formed homogenous liquids below 100 °C. No homogenous liquid formation was noted below 100 °C for either of the tetra-substituted systems. The urea/thiourea systems with ChCl both had the largest depressions in melting point (over 100 °C from their pure components) this is likely attributed to having the largest amount of hydrogen bond donating species present in the system therefore the largest disruption of the crystal lattices of the pure starting components.

Tetra-methylurea which is liquid at room temperature was left to stir overnight at 80 °C with the appropriate amounts of ChCl, however the solid ChCl remained present in reaction vessel and a mass balance calculation concluded that negligible amounts of the ChCl had dissolved. This led to the conclusions that no eutectic forming interaction was taking place. Similarly, ChCl and tetramethylthiourea failed to form a homogenous liquid below 100 °C. This gives insight to the bonding to say that hydrogen bond donation from the hydroxyl group on ChCl alone is not enough for deep eutectic solvent formation with a Ur/Tu type moiety.

1:2 ChCl: 1,3 dimethylurea formed a liquid at 40 °C this is a depression of over 60 °C from the melting point of pure 1,3 dimethylurea. A complementary data set was then produced for ChCl: 1,3 dimethylurea mixtures using POM, the method for measurement was the same as that described in 2.2.4. The data shown in Figure 4.2-4 agrees with the DSC findings that the eutectic mixture is the 1:2 ChCl: 1,3 dimethylurea sample, with a recorded melting point of 39.8 °C. This melting point depression is somewhat lower than the depression of above 90 °C for urea in the 1:2 ChCl:urea eutectic once again reiterating the increased influence of the four available hydrogen bond donation sites present in urea, over the two hydrogen bond donors available in 1,3 dimethylurea.

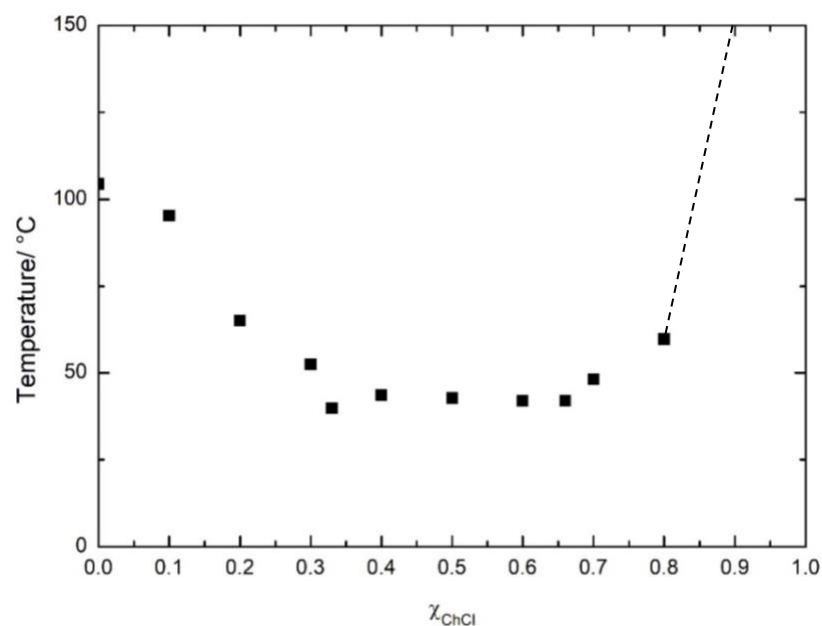


Figure 4.2-4: phase diagram for ChCl: 1,3 dimethylurea mixtures constructed using pom

Interestingly the 1:2 ChCl: 1,3-dimethylthiourea eutectic was found to be a room temperature liquid with a lower viscosity than 1:2 ChCl:urea. Observing the system, it was glassy in nature unlike the more crystalline 1:2 ChCl: urea eutectic. As a result, differing compositions of ChCl: 1,3-dimethylthiourea mixtures were produced and DSC scans were taken for the mixtures to determine where T_g was observed across the composition range. The results in Table 4.2-2 show that indeed T_g s are detected across a broad compositional range ($\chi_{\text{ChCl}} = 0.10$ - 0.60) with the lowest T_g (-59.7) interestingly recorded for the $\chi_{\text{ChCl}} = 0.33$ ChCl: 1,3-dimethylthiourea sample which is the expected eutectic mixture.

Table 4.2-2: T_g for mixtures of ChCl:1,3-dimethylthiourea

χ_{ChCl}	$T_g/^\circ\text{C}$
0.10	-36.59
0.16	-37.49
0.20	-42.82
0.30	-45.88
0.33	-59.68
0.40	-52.64
0.50	-41.49
0.60	-41.07

The formation of a crystalline DES for ChCl:urea/thiourea and an amorphous system for ChCl: 1,3-dimethylthiourea raises an interesting question: why do these very chemically similar systems have very different solid state forms? Recent literature would suggest that this question is not just isolated to DES but many liquids.²⁴⁷

After producing a ChCl:thiourea mixture at the claimed eutectic point of 1:2,¹¹⁵ which melting point of 69 °C using DSC (Figure 4.2-2). The scan shows that while the final endothermic melting event occurs at 69.7 °C, melting is initiated at much lower temperature (45.2 °C) and appears to be a two-step process, with the initial melting process concluding at around 52 °C before the stated second melting point at 69.2 °C. To elucidate the phase behaviour of ChCl:thiourea mixtures in more detail, POM data for melting points was produced across a compositional range for the mixtures Figure 4.2-5.

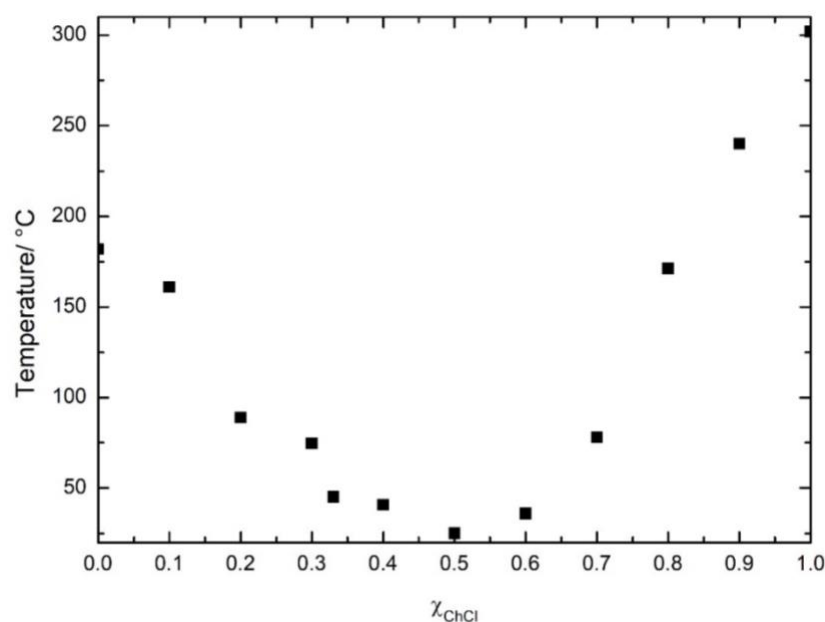


Figure 4.2-5: Phase diagram for ChCl:Tu constructed using POM

Surprisingly it was found that 1:1 ChCl:thiourea ($\chi_{\text{ChCl}} = 0.50$ ChCl:Tu), the sample began to behave as a liquid at 25 °C. This would indicate that eutectic point is formed at the 1:1 composition rather than at 1:2 ChCl:thiourea as previously reported.¹¹⁵ In this way, the ChCl:thiourea system differs from that of the urea analogue, ChCl:urea as studied in section 2.3.2, where the eutectic composition is 1:2. Taking the 1:1 ChCl:thiourea system as the eutectic point, the common trend of increasing melting temperatures moving away from the eutectic point is once again observed as shown in the phase diagram in Figure 4.2-5.

The study has shown that phase diagrams are a critical tool for the characterisation of DES to determine the true eutectic point of a system and that a number of complementary techniques are available (DSC,POM) to aid in the construction of phase diagrams. This resulted in an updated phase diagram being produced for the ChCl:Tu system using POM which recorded the eutectic point to be at the $\chi_{\text{ChCl}} = 0.50$ ChCl:Tu, which is in contrast to the literature.¹¹⁵ The substitution of methyl groups on to the thioamides of thiourea does not necessarily inhibit eutectic behaviour but alters the solidification process causing the liquids to solidify as amorphous glasses instead of crystalline materials.

4.3 ChCl: carboxylic acid DES

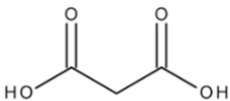
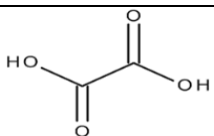
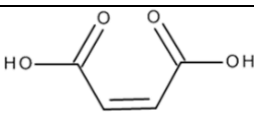
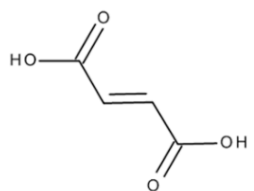
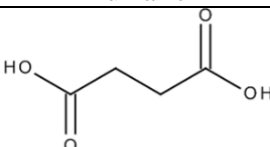
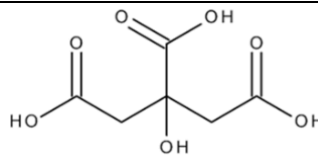
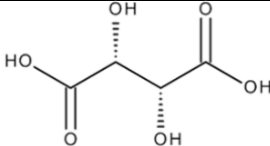
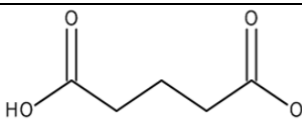
Many dicarboxylic acids have been proven to form stable deep eutectic solvents with ChCl.⁴⁵ A study was carried out to compare the acid dissociation constant of the dicarboxylic acid with the ability of that species to form a eutectic and the molecular ratio of the eutectic (Table 4.3-1). The purpose of the study was to test whether the lability of the acidic proton in the carboxylic acid has any effect on the formation of deep eutectic solvents. The theory being that having more labile protons on the carboxylic acid would aid the deep eutectic formation.

Mixtures of ChCl and a carboxylic acid were added together at specific molar ratios (1:1,1:2 ChCl: carboxylic acid) along with a small portion of dried methanol, the mixtures were stirred for 15 min before solvent was removed using a rotary evaporator at 60 °C for 1 hour.

Examining the dicarboxylic acids tested it appeared that pKa did not have a largely influential effect on the formation of the DESs, nor on what ratio the eutectic point was at. Carboxylic acids with a low 1st pKa such as oxalic acid (pKa=1.23) formed a eutectic at a molar ratio of 1:1 with ChCl, similarly glutartic acid formed a deep eutectic with a higher 1st pKa (pka=4.34) and once again this was at the 1:1 ratio that seems to be the trend for all dicarboxylic acids.

A factor that seemed to be more influential on the formation of deep eutectic solvents was how the size and geometry of the dicarboxylic acid effected the eutectic formation. Comparing two similar molecules which atomistically are identical but are conformationally locked into different positions; maleic acid (*cis*) and fumaric acid (*trans*) we can see that only the maleic acid forms a eutectic liquid at room temperature. This could be attributed to the lower melting point of maleic acid (135 °C) in comparison to fumaric acid (287 °C) as a result of maleic acid intramolecular bonding vs. the intermolecular bonding in fumaric acid.

Table 4.3-1: The pKa values and eutectic formation for a range of carboxylic acids with ChCl. All pKa values taken from “Data compiled by R.Williams”.²⁴⁸

Carboxylic acid	1 st p _{ka} value	2 nd p _{ka} value	Molar ratio	Eutectic point formation
 Malonic	2.83	5.69	1:1 1:2	Yes No
 Oxalic	1.23	4.19	1:1 1:2	Yes No (DSC confirmation)
 Maleic	1.93	6.58	1:1 1:2	Yes No
 Fumaric	3.03	4.54	1:1 1:2	No No
 Succinic	4.29	5.48	1:1 1:2	No No
 Citric	3.09	4.75 3 rd (5.41)	1:1 1:2	Yes Yes Both liquid
 L-Tartaric	2.99	4.40	1:1 1:2	Yes No
 Glutaric	4.34	5.42	1:1 1:2	Yes No (Gel with solid)

4.4 TOPO DES

All the systems previously described in this chapter have a common feature, they are all hydrophilic, water miscible solvents. As eluded to earlier in this work to complement current metal oxide dissolution using DESs which was present in the literature,^{177–182} an alternative strategy was designed in the same theme of recovery of metals from waste sources from DES. But, instead of direct metal oxide dissolution, recovery from acidic aqueous streams was the target, as this negated the need for any high reaction temperatures. For this a low vicious, hydrophobic solvent was needed to carry out biphasic extraction meaning ammonium salts such as, ChCl, which are incredibly hygroscopic were no longer suitable. This led to the development of trioctylphosphine oxide (TOPO, $T_m = 52\text{ }^{\circ}\text{C}$) based DES, a molecule that is both used as an extractant of uranyl ions,^{249,250} and a co-ordinating ligand in the formation of LCCs.^{71,76} Having observed how mixtures of ChCl and carboxylic acid could form DESs in 4.3 and knowing that TOPO was used as an extractant in organic diluents for carboxylic acids from aqueous systems.²⁵¹ It was postulated that the non-ion species TOPO could form hydrophobic DES. The theory was tested by making equimolar mixtures of TOPO with malic acid and phenol.

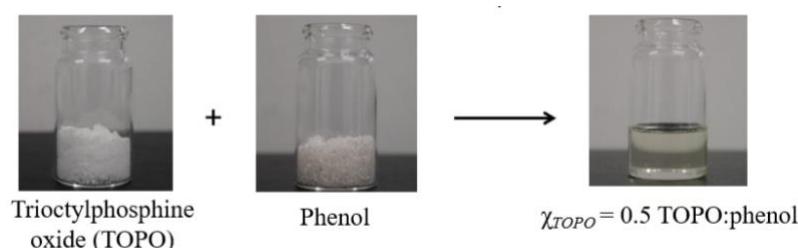
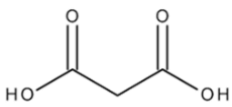
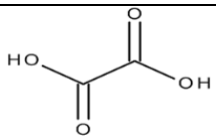
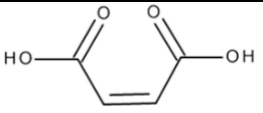
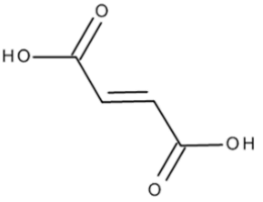
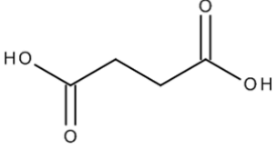


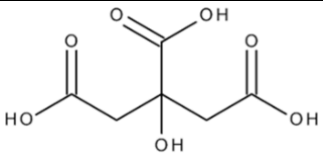
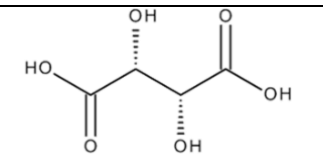
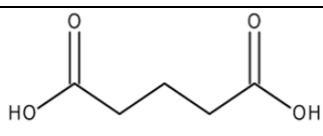
Figure 4.4-1: Formation of TOPO:phenol DES

The mixtures began to liquified upon contact in atmospheric conditions at $25\text{ }^{\circ}\text{C}$ and after further stirring a colourless (Figure 4.4-1), homogenous liquid was formed. Upon the addition of small amounts of water it was found that the DES did indeed form biphasic layers with water.

After forming TOPO:DESs with phenol, a TOPO:carboxylic acid screen (Table 4.4-1) was carried out similar to that for ChCl shown in 4.3.

Table 4.4-1: TOPO:carboxylic acid screen, All pKa values taken from “Data compiled by R.Williams”.²⁴⁸

Carboxylic acid	1 st p _{Ka} value	2 nd p _{Ka} value	Molar ratio	Eutectic point formation
 Malonic	2.83	5.69	1:1 2:1	Yes No (crystals formed in fridge)
 Oxalic	1.23	4.19	1:1 2:1	No Yes
 Maleic	1.93	6.58	1:1 2:1	Yes No (liquid but DSC showed melt/cryst)
 Fumaric	3.03	4.54	1:1 2:1	No Yes
 Succinic	4.29	5.48	1:1 2:1	No Yes

 <p>Citric</p>	3.09	4.75 3 rd (5.41)	1:1 2:1 3:1	No Yes Yes
 <p>L-Tartaric</p>	2.99	4.40	1:1 2:1	No Yes
 <p>Glutaric</p>	4.34	5.42	1:1 2:1	Yes Yes

An in-depth physico-chemical study of TOPO:phenol mixtures along with potential applications is described in Chapter 5.

5 HYDROPHOBIC DES

5.1 Current hydrophobic DES

DES require hydrogen bonding for their formation, this also leads them to be able to readily form hydrogen bonds with water making them water miscible.¹¹⁵ A new group of water immiscible, hydrophobic DES have been reported,¹⁵⁵ which could prove to be useful as their immiscible nature would allow for biphasic extraction of metals from aqueous sources such as the waste streams from red mud production, a similar process of recovering metal salts from aqueous waste streams has already been published.²⁵² In the study long alkyl chain quaternary ammonium salts such as $[N_{8881}]Br$ were used as the hydrogen bond acceptors (HBA) with decanoic acid added as the hydrogen bond donor. As a result of the long chains on the HBA, the DES were hydrophobic in character and with increasing chain length on the HBA the hydrophobic character increased, however there was a trade off as the longer the chain on the HBA present in the DES, the more viscous the DES tended to be, this may lead to difficulties when mixing with engineering wastes.

5.2 Background

The use of DES analogues of hydrophobic ionic liquids^{253,254} as alternatives to hydrophobic organic solvents for organic/aqueous extractions has been scarcely investigated to-date, partially because the multiple competing Coulombic and hydrogen-bonding interactions^{131,137,216,219,220,222,223} that underpin the formation of these liquids also tend to promote miscibility with water.

The first hydrophobic DES, reported by van Osch *et al.*¹⁵⁵ in 2015, combined a carboxylic acid (to provide H-bond donor functionality) with long chain quaternary ammonium salts to enhance hydrophobicity over more usual short chain ammonium or cholinium salts. Following this strategy, other hydrophobic DESs incorporating fatty acids and/or alcohols with organic salts have been described and their use for metal ion²⁵⁵ and natural product^{256,257} extractions demonstrated. However, in common with ionic liquids, the Coulombic interactions between the charge centres result in liquids with relatively high viscosity. This is compounded by the need to introduce large bulky alkyl substituents to impart hydrophobicity competing with the hydrophilic association of typically good hydrogen-bond acceptor anions present with water.

Moving away from ionic DESs, which include a salt (or an ionizable amine component²⁵⁵), Ribeiro *et al.*¹⁵⁶ have shown that hydrophobic eutectic solvents could be prepared from mixtures of DL-menthol with a range of carboxylic acids and used as extractive solvents for caffeine, tryptophan, isophthalic acid, and vanillin from water. Compared to the more usual ionic DES, these liquids have significantly lower viscosity as a result of eliminating the Coulombic charge interactions. The scope for formation of liquid eutectic solvents has subsequently been expanded to a range of terpenes with monocarboxylic acids²⁵⁸ and, interestingly, also to make use of mixtures of carboxylic acids to access eutectic liquid compositions.²⁵⁹

Phosphonium ionic liquids have been thoroughly investigated as solvent systems due to their enhanced properties such as thermal stability over more traditional nitrogen based ionic liquids.²⁶⁰ Building on previous experience using trioctylphosphine oxide (TOPO) as a Lewis basic (hydrogen-bond accepting) ligand to generate liquid coordination complexes^{75,76,84} with tunable Lewis acid properties we were interested in studying whether trioctylphosphine oxide (TOPO) could be used as a hydrogen-bond-accepting component to produce DES and whether a liquid DES formed in this way could be used as an extractant phase containing high phosphine oxide concentrations.

TOPO has many applications as a capping agent for the production of quantum confined nanomaterials,^{261–265} and as an extractant²⁶⁶ for metal ions, and organic acids^{267–270} and phenolic compounds.^{271–273} However, an issue with TOPO is its relatively low solubility in hydrocarbon solvents that are the choice for aqueous–organic liquid–liquid extraction processes. One approach to address this is the use of alternative phosphine oxide formulations, such as Cyanex 923^{274,275} this is a mixture of trialkylphosphine oxides containing hexyl and octyl groups that is a liquid (T_m –5 to 0 °C) and is completely miscible with common industrial diluents (such as kerosene) allowing higher concentrations of extractant to be achieved than with pure TOPO.

To our knowledge, TOPO had not been transformed into an ambient temperature DES, and we reasoned that a DES formed from TOPO containing a high phosphine oxide concentration would overcome some of the challenges faced by the choices of diluent, *viz.*, limiting solubility in non-hazardous solvents such as odourless kerosene or high solubility in hazardous solvents such as dichloromethane or benzene. Based on the initial screen (Chapter 4.4) that showed that TOPO combined with small carboxylic acids formed hydrophobic liquids, the detailed investigation of ambient temperature hydrophobic eutectic liquid formation between TOPO and phenol, as a model hydrogen-bond donor (Figure 5.2-1) was

made. The applicability of the system to metal extraction is demonstrated for the removal of uranyl ($[UO_2]^{2+}$) ions from aqueous nitric acid as an exemplar of the use of these DES for metal ion extraction and recovery was explored.

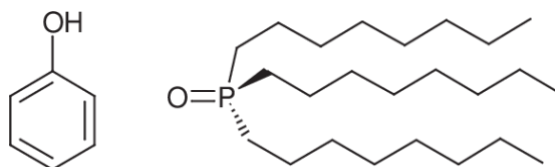


Figure 5.2-1: Phenol (left) and TOPO (right)

5.3 Experimental

5.3.1 Chemicals and methods

Trioctylphosphine oxide (TOPO) was kindly provided by Solvay with a purity $> 90\%$; phenol (99.5%) was purchased from Acros Organics. TOPO:phenol mixtures were prepared by combining appropriate mole fractions of each component in a minimum quantity of methanol, which was then stirred (500 rpm) until a homogeneous, colourless liquid was formed. Methanol was then removed by evaporation in vacuo (3 days, $50\text{ }^{\circ}\text{C}$, 10^{-2} bar) and then allowed to cool to ambient temperature yielding colourless solids ($\chi_{\text{TOPO}} > 0.6$) or liquids ($\chi_{\text{TOPO}} < 0.6$). Materials were stored under an inert atmosphere until used. Composition and purity of the resulting mixtures were confirmed using NMR (Bruker 400 MHz) and FT-IR (PerkinElmer Spectrum 100) spectroscopy.

5.3.2 NMR spectroscopy

^{31}P NMR spectra were recorded on a Bruker Avance DPX 400 MHz spectrometer at 162 MHz using neat liquid samples. A DMSO filled, sealed capillary was used as an external lock, and stability between measurements was confirmed from the invariance of the chemical shift from trace impurities at -0.72 ± 0.13 ppm. Further phosphorus-containing impurities were observed in the supplied TOPO sample, observed as singlet signals at 48.48, 48.78, 51.9, and 53.44 ppm compared to the main TOPO signal at 49.1 ppm for the $\chi_{\text{TOPO}} = 0.60$ liquid. The ^{31}P signals for each of these trace contaminants varied with χ_{TOPO} along with the signal from TOPO as described in section 5.4 Results and discussion.

5.3.3 Density and viscosity

Densities were measured using a Mettler Toledo DM40 density meter over the temperature range 25–90 °C. Viscosity was determined using a Bohlin Gemini cone and plate rheometer (TOPO:phenol, $\chi_{\text{TOPO}} = 0.33$) between 20 and 90 °C, and using an Anton Paar AMVn rolling ball viscometer (TOPO:phenol, $\chi_{\text{TOPO}} = 0.50$) at 20, 25, 40, 50, and 60 °C.

5.3.4 Water content

Water content was measured using a Mettler Toledo C30S coulometric KF titrator; in each case, the initial water content was below the limit of quantification of the titrator, and characteristic signals attributable to water were not observed in the ^1H NMR or FT-IR spectra of the neat $\chi_{\text{TOPO}} = 0.50$ liquid.

5.3.5 TOPO/Phenol Solid–Liquid Phase Diagram

5.3.5.1 DSC

Upper limits for thermal stability of the liquids were measured in the dynamic heating regime using a TA Instruments Q5000 TGA instrument under nitrogen atmosphere. The phase diagram was determined both by visual inspection and by differential scanning calorimetry (DSC). DSC measurements were performed using a TA Instruments DSC Q2000 instrument fitted with RCS 90 cooling system. Samples were loaded into Tzero aluminium pans, and the accurate mass was recorded (± 0.0002 g) in a glovebox under an argon dry atmosphere and then sealed using Tzero hermetic lids before removal and transfer to the DSC. Measurements were taken over three heating/cooling cycles across the temperature range from –90 to +70 °C, with a cooling rate of 5 °C min^{–1} and a heating rate of 1 °C min^{–1}. Between heating and cooling runs, samples were held isothermally for 15 min.

5.3.5.2 Solid-liquid Cell

Visual determination of the solid–liquid equilibrium phase behaviour was made as a function of temperature using samples sealed in a thermostated Pyrex glass solid–liquid equilibrium cell containing a magnetic stir-bar. The cell was then inserted in a thermostated ethanol bath and stirred (400 rpm) and cooled to around –50 °C by addition of liquid nitrogen. After holding at this temperature for 15 min samples were then allowed to warm to –10 °C at a rate of approximately 1–2 °C min^{–1}. Samples with χ_{TOPO} between 0.2 and 0.4 exhibited melting of the quenched glasses around –35 °C, whereas the remainder of the samples (high and low χ_{TOPO}) remained as solids over this temperature range. Above *ca.* –10 °C,

temperature was controlled by a circulating Julabo R32, and samples were held for 20 min at each set-point to ensure equilibrium.

Temperatures were measured using an insulated wire miniature type K thermocouple model 5SC coupled with a HH802U thermocouple thermometer, with an expected measurement uncertainty of ± 1.5 °C. The measurement uncertainty resulting from the visual observation of the phase transitions is expected to be greater than the instrumental error. The melting points were recorded as the temperature at which a colourless homogeneous liquid was formed in the cell. Glass transitions for the non-crystalline mixtures (χ_{TOPO} between 0.2 and 0.4) were defined from the pour points, the lowest temperature at which motion of the stir-bar was possible in the increasingly viscous liquids on cooling. No T_g transitions were observed in the DSC for these samples on cooling to -90 °C. All measurements were carried out in duplicate, with reproducibility to within 1 °C.

5.3.6 Phenol and TOPO Leaching to Aqueous in I/I Mixtures

Leaching of phenol into aqueous hydrochloric acid from the $\chi_{\text{TOPO}} = 0.50$ TOPO:phenol eutectic liquid was determined at room temperature by combining equal amounts (w/w) of the TOPO:phenol sample and aqueous acid (0.00–3.00 M HCl) in a vial which was shaken on a Stuart scientific flask shaker SF1 for 30 min and then left for 18 h to allow complete equilibration and separation of the two layers. The phenol content of the aqueous phase was then analysed using UV–vis spectroscopy (Agilent Technologies Cary 60 UV–vis spectrophotometer) with the concentration of leached phenol determined by comparison of the absorbance at $\lambda_{\text{max}} = 270$ nm to a standard calibration response determined for aqueous phenol.

5.3.7 Liquid–Liquid Extraction of Uranyl ($[\text{UO}_2]_{2+}$) Ions from Aqueous Acid with TOPO: Phenol Eutectic Liquids

All aqueous solutions were prepared with deionized water, purified with a Barnsted deionization system, and polished to $18.3 \text{ M}\Omega \text{ cm}^{-1}$. Aqueous solutions of HNO_3 were prepared as molar concentrations between 0.01 and 3.00 M by transferring a known amount of material to a volumetric flask and diluting to the specified volume with deionized water. Uranyl solutions in water and in nitric acid were prepared by addition of uranyl nitrate hexahydrate to the standard acidic stock solutions to 250 ppm (6.34×10^{-4} M) and, in one case, with 2350 ppm (5.96×10^{-3} M) $[\text{UO}_2]_{2+}$ in 1 M $\text{HNO}_3(\text{aq})$ to examine the effects of uranyl concentration on extraction efficiency.

For uranyl extraction measurements, performed at ambient temperature (*ca.* 20–25 °C), 1 cm³ samples of TOPO:phenol ($\chi_{\text{TOPO}} = 0.5$) pre-equilibrated against the appropriate concentration aqueous nitric acid solution were contacted with 1 cm³ of an acidic 250 ppm uranyl nitrate solution in a 10 cm³ screw top glass vial and mixed for 10 min using a wrist-action shaker (Burrell, model 75). After mixing, the samples were centrifuged (2000g, 2 min), and the aqueous raffinate phase was separated from the DES. The residual uranium concentration in the raffinate (aqueous phase) was determined by UV–vis spectroscopy (Agilent Technologies Cary 60 UV–vis spectrophotometer) after addition of 2-(5-bromo-2-pyridylazo)-5-(diethylamino)phenol (Br-PADAP) to the sample as a spectroscopic probe.²⁷⁵ All measurements were performed in duplicate and gave reproducible results.

Distribution ratios (*D*) were estimated from the difference between the initial and final uranyl concentrations in the aqueous raffinate phase using the following equation:

$$D = ([\text{UO}_{22+}]_{\text{init}} - [\text{UO}_{22+}]_{\text{final}})/[\text{UO}_{22+}]_{\text{final}} \quad \text{Equation 5.3-1}$$

where $[\text{UO}_{22+}]_{\text{init}}$ and $[\text{UO}_{22+}]_{\text{final}}$ are the initial and final uranyl concentrations (mol dm⁻³) in the acidic aqueous phase.

5.4 Results and discussion

Eutectic mixtures composed of TOPO and phenol in different molar ratios were prepared by mixing the two components with a small quantity of methanol, followed by evaporation of the solvent. It was also possible to form liquids by grinding the two components together. Room temperature liquids were obtained over the composition range $\chi_{\text{TOPO}} = 0.1\text{--}0.6$ (Figure 5.4-1) and were colourless, free-flowing and were found to be hydrophobic, forming biphases when mixed with water.

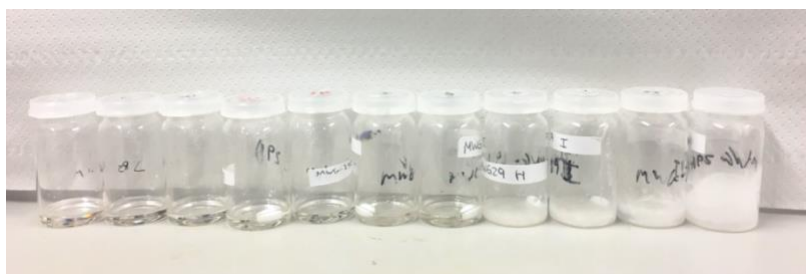


Figure 5.4-1: The appearance of TOPO:phenol mixtures of different compositions at ambient temperature (left to right $\chi_{\text{TOPO}} = 0.1\text{--}0.9$)

Phenol was selected for initial examination based on its mild Brønsted acidity (and corresponding hydrogen-bond donor ability), the use of TOPO-impregnated membranes for

solventless extraction and stripping of phenols from water,^{271,273,276} and the ability of phenol to form biphasic systems with water at moderate concentrations and temperatures.^{277,278} Similarly, there was a synergistic interest in forming hydrophobic eutectics with phenol to complement the application of phenol/tetraalkylammonium chloride DES for recovery of phenols from hydrocarbon oils.¹⁹⁵

The effectiveness of eutectic formation as a strategy to obtain liquefied TOPO with high phosphine oxide concentration for use in separations was then tested for liquid–liquid extraction of $[\text{UO}_2]^{2+}$ from aqueous acid solution.

5.4.1 Thermal Stability

TOPO:phenol mixtures retained a constant composition through heating at 50 °C to remove methanol, as confirmed by integrating and comparing ^1H NMR signals from phenol and TOPO components of the mixtures after drying, and were thermally stable up to *ca.* 90 °C. Compared to the rapid mass loss from pure phenol, the TOPO:phenol liquid mixtures show increased stability, with two distinct events observable by TGA under dynamic heating (Figure 5.4-2). The first of these, loss of phenol through evaporation or sublimation, starts around 100 °C and is complete by 200 °C, in contrast to pure phenol where mass loss started at 50 °C and was complete by 130 °C. In the TOPO:phenol mixtures, this is then followed by loss of TOPO above *ca.* 250 °C. Thus, the stability limit for the TOPO:phenol liquids, defined by loss of phenol from the liquids, is around 90–100 °C, which is comparable with that of the archetypal ChCl/Ur DES¹¹⁵ where decomposition of Ur is initiated from around 70 °C.

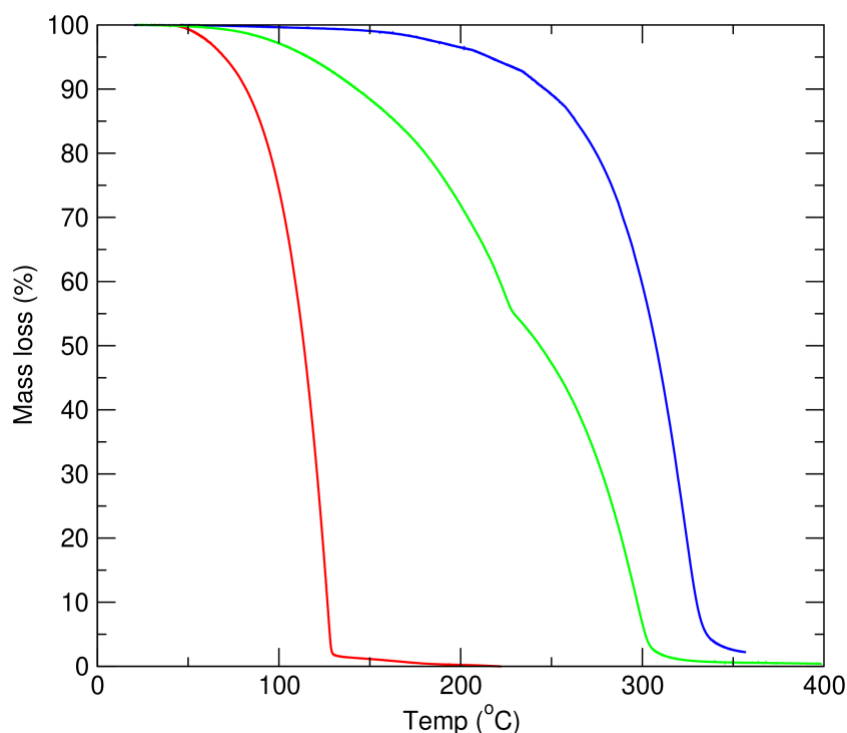


Figure 5.4-2: Mass loss profiles under dynamic TGA conditions for phenol (red), TOPO (blue) and TOPO:phenol ($\chi_{\text{TOPO}} = 0.50$, green) heating at $5\text{ }^{\circ}\text{C min}^{-1}$, showing the increased thermal stability (reduced loss of phenol) in the DES compared to neat phenol.

5.4.2 Melting Point and Phase Composition

A detailed investigation of the solid–liquid phase behaviour of the TOPO:phenol system was made using both visual observation from samples in a solid–liquid cell and by DSC (Figure 5.4-3). Across the intermediate composition range ($\chi_{\text{TOPO}} = 0.20 - 0.40$), free-flowing liquids were obtained that became progressively more viscous on cooling, eventually forming glasses that could not be poured below around *ca.* $-34\text{ }^{\circ}\text{C}$. The cooling and heating profiles in the DSC measurements at these compositions were essentially featureless; no crystallization or glass transition events were observable, either around the solidification points observed visually or scanning to $-80\text{ }^{\circ}\text{C}$.

In contrast, at $\chi_{\text{TOPO}} = 0.10$ and from $\chi_{\text{TOPO}} = 0.50\text{--}1.00$, solid samples were obtained from which melting was observable both visually and from first order transitions in the DSC at comparable temperatures in the two experiments. TOPO:phenol with $\chi_{\text{TOPO}} = 0.10$ extensively supercools in the DSC, undergoing cold-crystallization on heating at *ca.* $-50\text{ }^{\circ}\text{C}$ and is then followed by melting at $27.5\text{ }^{\circ}\text{C}$. This pattern was repeated over three thermal cycles and shows a small depression in melting of the $\chi_{\text{TOPO}} = 0.10$ mixture compared to pure phenol ($T_{\text{m}} = 41\text{ }^{\circ}\text{C}$).

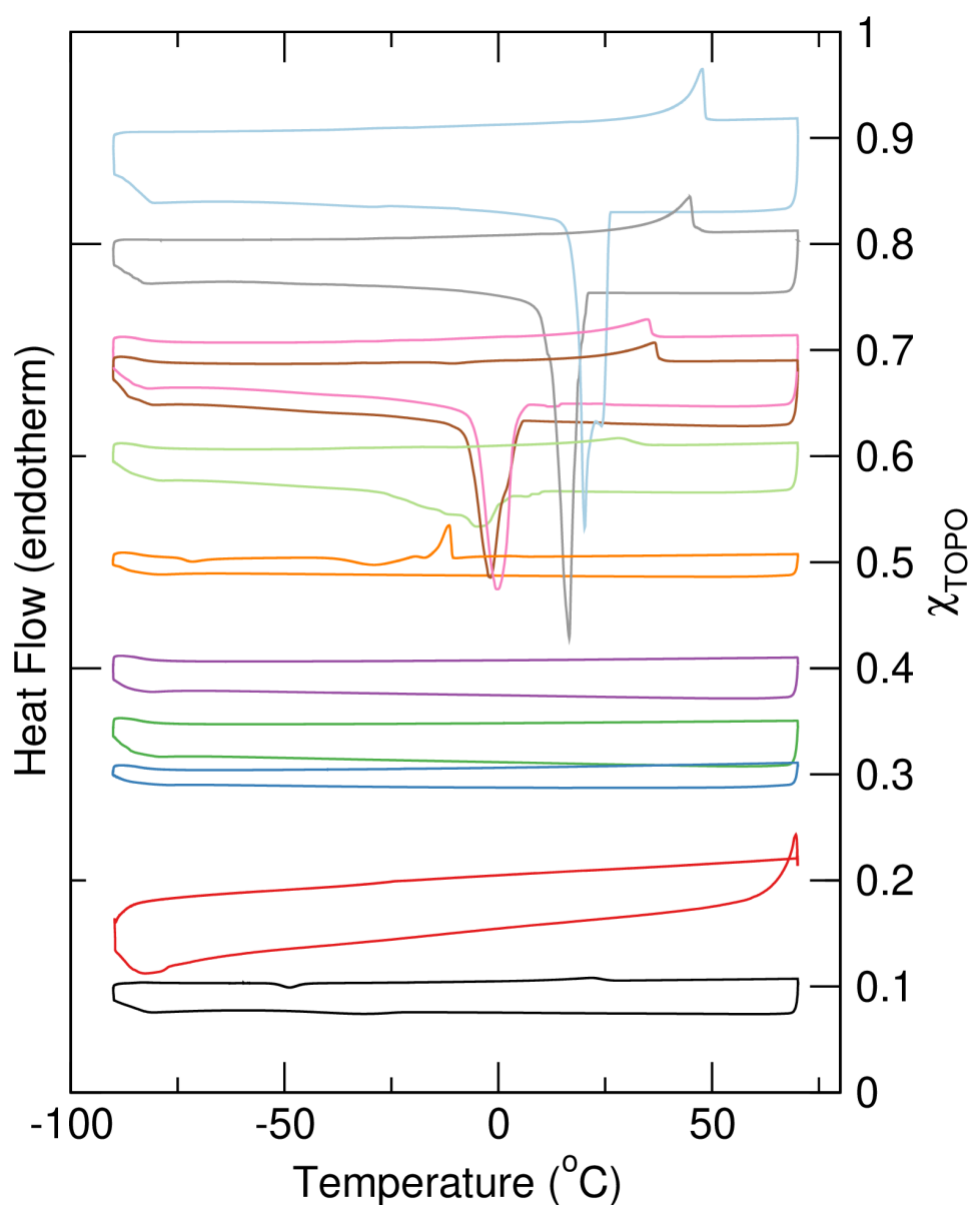


Figure 5.4-3: DES second cooling and heating profiles for TOPO:phenol mixtures offset from the baseline by their corresponding compositions (χ_{TOPO}).

At $\chi_{\text{TOPO}} = 0.50$, in the DSC, the samples supercooled and then, on heating, undergo cold-crystallization with an extremely broad (*ca.* 20 °C) endothermic transition centred at -29 °C. This is followed by a sharp exotherm at -11 °C ($\Delta H = 11.7$ kJ mol $^{-1}$), and a much weaker broad exotherm between -10 and 6 °C.

Table 5.4-1: Thermal data from DSC and observation. Temperatures were measured from the peak positions of the first order transitions in the DSC second heating cycle, and the enthalpy of melting determined from integration of the peak.

χ_{TOPO}	T_m (Obs) / °C	T_m (DSC) / °C	E_m / KJ mol ⁻¹
0.00	41.1	41.0	
0.10	24.2	27.5	1.8
0.20	-33.0 _b		
0.30	-33.5 _b		
0.33	-33.0 _b		
0.40	-36.5 _b		
0.50	-11 _c	5.9	11.7
0.60	30.3	34.6	3.3
0.67	36.4	38.1	6.3
0.70	38.7	36.7	6.9
0.80	42.8	46.2	16.6
0.90	50.3	48.8	23.9
1.00	51.8	51.9	
^a Temperatures were measured from the peak positions of the first order transitions in the DSC second heating cycle, and the enthalpy of melting was determined from integration of the peak. ^b Solidification temperatures for $\chi_{\text{TOPO}} = 0.2\text{--}0.4$ were made by visual observation of the limit in pour point of the liquids: no thermal transitions were observed by DSC. ^c Exothermic transition observed by DSC at -11 °C is followed by a weak, broad event between -10 and 6 °C.			

In the solid–liquid cell, on heating slowly from -40 °C, the mixture was observed to melted to a slurry from *ca.* -10 °C, forming a single homogeneous clear liquid phase at 6 °C. Above $\chi_{\text{TOPO}} = 0.50$, reversible melting and freezing transitions are more readily observed in the TOPO:phenol mixtures, with all samples solidifying at temperatures above 0 °C in both the solid–liquid cell and DSC. Both the crystallization point on cooling and subsequent melting point on heating of the mixtures were systematically reduced by the introduction of phenol, and the melting transition in the DSC becomes increasingly broad, with a long trailing edge indicative of pre-melt disordering of the alkyl-chain regions as is often seen in plastic crystals, particularly from ionic liquid materials.^{279–281}

The melting temperatures (and corresponding enthalpy) of the range of TOPO:phenol compositions are shown in Table 5.4-1, and the mole fraction TOPO:phenol temperature composition phase diagram generated from this data is shown in Figure 5.4-4. In common with many ionic liquids and with the cholinium-based DES examined in the earlier chapters, the TOPO:phenol mixtures proved inherently difficult to crystallize forming amorphous solids on cooling. The reduced melting points of the mixtures, coming from either high TOPO or high phenol composition, can be extrapolated to a eutectic point in the region of $\chi_{\text{TOPO}} = 0.33$ (1:2 TOPO:phenol) with an extensive liquid region down to *ca.* -34°C between $\chi_{\text{TOPO}} = 0.2$ and 0.5 , a reduction of 70°C compared to the melting points of TOPO ($T_{\text{m}} = 52^{\circ}\text{C}$) and phenol ($T_{\text{m}} = 42^{\circ}\text{C}$).

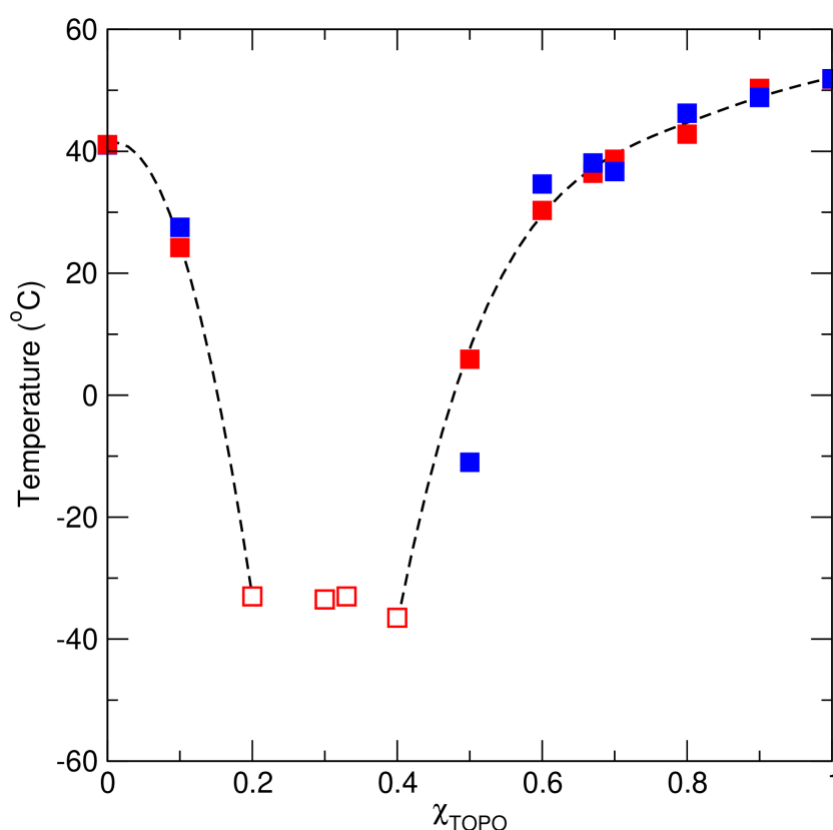


Figure 5.4-4: Phase diagram for TOPO:phenol mixture, constructed from observational solidification points (solid-liquid cell, ■), DSC results (■), and solid-liquid cell glass transitions (□).

^{31}P NMR spectra taken from neat liquid mixtures (at 25°C) at different compositions across the phase diagram are shown in Figure 5.4-5 with the chemical shifts tabulated in Table 5.4-2. The phosphorus signal from TOPO becomes increasingly deshielded, moving downfield as the concentration of phenol in the mixtures is increased (a reduction in χ_{TOPO}) reflecting the increasing addition of the acidic hydrogen-bond component in the liquids.

Between $\chi_{\text{TOPO}} = 0.60$ and 0.50 , the change in ^{31}P chemical shift is only small. Both $\chi_{\text{TOPO}} = 0.50$ and 0.60 liquids gave ^{31}P signals between 49 and 50 ppm, comparable to the value reported²⁸² for TOPO dissolved in CDCl_3 ($\delta_{^{31}\text{P}} = 48.48$ ppm), and higher than that in C_6D_6 ($\delta_{^{31}\text{P}} = 43.93$ ppm). These data points are shown in Figure 5.4-5 for comparison. This suggests that above $\chi_{\text{TOPO}} = 0.50$ (1:1 TOPO:phenol), the liquids have a phosphine oxide environment that resembles that of TOPO dissolved in chloroform, and that all the phenol molecules present are involved in hydrogen-bonding to single P=O sites.

In contrast, on increasing the phenol (acid) content of the liquids (i.e., moving to lower χ_{TOPO}), the change in ^{31}P chemical shift, with the signals moving progressively downfield, reports that the phosphine oxide group is experiencing an increasingly acidic environment. However, $\Delta\delta_{^{31}\text{P}}$ remains approximately constant suggesting that, as additional phenol is added, over the range $\chi_{\text{TOPO}} = 0.5\text{--}0.2$, it contributes directly to changes to the local TOPO environment. In the solid state, trialkylphosphine oxides tend to form two hydrogen-bonds in cocrystals,²⁸³ and it is likely that the observed eutectic minimum around $\chi_{\text{TOPO}} = 0.33$ (2:1 phenol: TOPO stoichiometry) reflects this maximum number of hydrogen-bonding interactions in the liquid mixtures. However, unlike static hydrogen-bonding

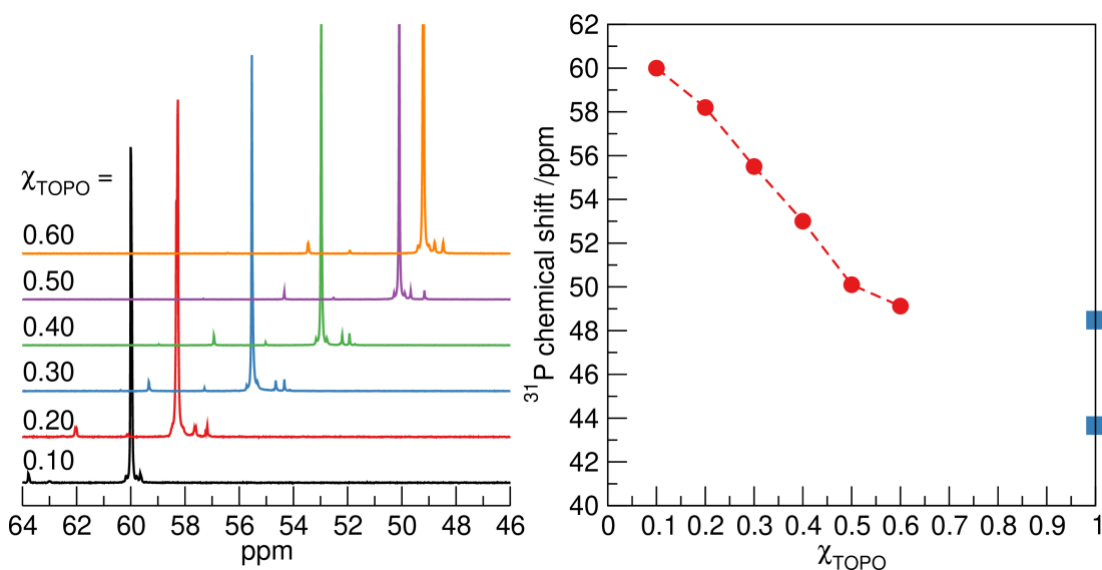


Figure 5.4-5: ^{31}P NMR spectra of TOPO:phenol liquids (left) and the corresponding chemical shift plotted as a function of liquid composition (right). Chemical shifts²⁸² for TOPO in CDCl_3 (43.66 ppm) and in C_6D_6 (48.48 ppm) are shown at $\chi_{\text{TOPO}} = 1$ (blue squares) for comparison.

enabling cocrystal formation, the dynamic nature of hydrogen-bonds here probably leads to disruptive competition with lattice packing forces to induce liquid formation. The ^{31}P NMR study of the TOPO:Phenol mixtures also shows multiple phosphorus environments associated with impurities present in the TOPO starting material. These impurities may have

an impact on the recorded melting points both for TOPO and the TOPO:phenol mixtures. However, the average melting point recorded in this study for TOPO using DSC and observations was 51.9 °C, this is in-keeping with the literature melting point range for high purity (99%) TOPO of 50-52 °C,²⁸⁴ therefore the impurities did not appear to have a large influence on melting point .

Table 5.4-2: ³¹P NMR Chemical Shifts (δ ³¹P/ppm) for TOPO: Phenol Liquids as a Function of Composition (χ_{TOPO})

χ_{TOPO}	³¹ P / ppm
0.10	60.0
0.20	58.2
0.30	55.5
0.40	53.0
0.50	50.1
0.60	49.1

It is worth noting that these changes in chemical shift ($\Delta\delta$ ³¹P = 10-11) are much smaller than have been observed for interactions of TOPO with Lewis acid metal salts forming, for example, liquid coordination complexes⁷⁵ or when TOPO coordinates to hydrated protons,²⁸⁵ where the ³¹P NMR chemical shifts have been reported to change by up to nearly 40 ppm.

5.4.3 Density and Viscosity

Density and viscosity of the $\chi_{\text{TOPO}} = 0.33$ (eutectic) and 0.50 (equimolar) liquids were measured between 20 and 90 °C to explore the eutectic composition with the largest liquid range and to characterize a liquid composition with a higher TOPO content that could be used for liquid–liquid extraction studies. Density and viscosity results are shown in Table 5.4-3 and Figures Figure 5.4-6 and Figure 5.4-7.

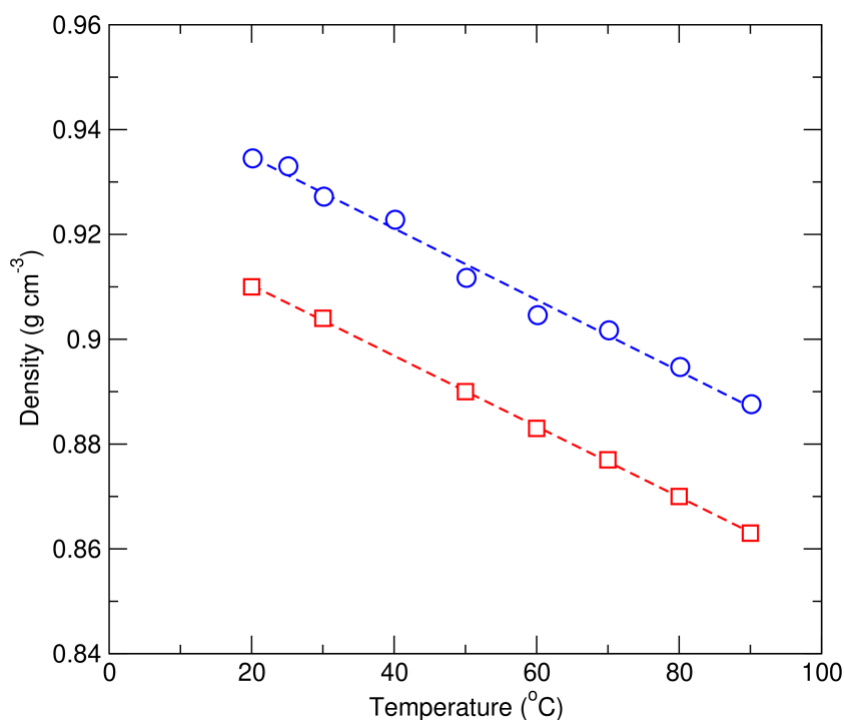


Figure 5.4-6: Density of TOPO:phenol liquids at $\chi_{\text{TOPO}} = 0.33$ (blue \circ) and 0.50 (red \square) showing the linear change in density with temperature, fitted as a function of temperature to $y = 1.1342 - 0.000\ 680\ 67x$ ($\chi_{\text{TOPO}} = 0.33$) and $y = 1.1075 - 0.000\ 673\ 19x$ ($\chi_{\text{TOPO}} = 0.50$). Density of the TOPO:phenol mixtures decreases with increasing TOPO content.

The densities of both compositions (0.935 g cm^{-3} for $\chi_{\text{TOPO}} = 0.33$ at $20\text{ }^{\circ}\text{C}$, and 0.910 g cm^{-3} for $\chi_{\text{TOPO}} = 0.50$) are less than that of water and decrease monotonically with increasing temperature. The density also decreases with increasing TOPO content, consistent with the differences in density of phenol and TOPO (1.07 and 0.88 g cm^{-3} , respectively). The volume expansion coefficient of $ca. 6.75 \times 10^{-4}\text{ cm}^3\text{ K}^{-1}$ is consistent with fluid expansion from liquids containing a large hydrocarbon component, in this case the octyl groups on TOPO.

The viscosities of both the dry $\chi_{\text{TOPO}} = 0.33$ and 0.50 TOPO:phenol liquids are much lower than those of conventional DES containing organic salt components²⁸⁶ and are over an order of magnitude lower than that of the $[\text{N}_{888}]\text{Br}$ decanoic acid DES ($\chi_{[\text{N}_{888}]\text{Br}} = 0.33$),¹⁵⁵ which was reported as 636.36 mPa s at $25\text{ }^{\circ}\text{C}$. For the eutectic TOPO:DES composition ($\chi_{\text{TOPO}} = 0.33$) the viscosity was 12.38 mPa s at $25\text{ }^{\circ}\text{C}$, similar to that of emerging non-ionic fatty acid eutectic liquid mixtures described by Florindo *et al.*²⁵⁹ and ethylene glycol (16.1 mPa s at $25\text{ }^{\circ}\text{C}$). Viscosity decreases with increasing temperature and was fitted with the Vogel–Fulcher–Tammann (VFT) model²⁸⁷ for glass forming liquids. An extrapolated glass transition temperature (T_0) of 209 K was obtained.

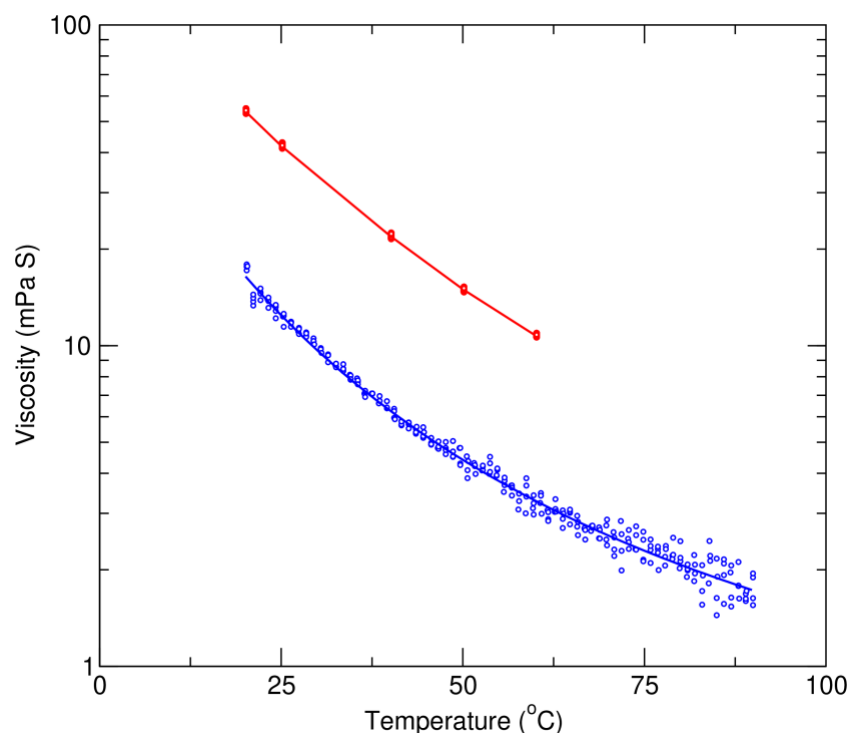


Figure 5.4-7: Viscosity of the TOPO:phenol liquids at $\chi_{\text{TOPO}} = 0.33$ (blue) and 0.50 (red) plotted as a function of temperature. Data at $\chi_{\text{TOPO}} = 0.33$ was fitted to the Vogel–Fulcher–Tammann (VFT) equation, $\eta = A \times e^{B/(T-T_0)}$, where η is viscosity (mPa s), T is temperature (K), and T_0 is the ideal glass transition temperature (K) with parameters of $\ln(A) = -5.234$, $B = 435$, and $T_0 = 209$ K ($r_2 = 0.994\ 568$).

As more TOPO is added, viscosity (and the solidification temperature) increases, but still remains low. At $\chi_{\text{TOPO}} = 0.50$, the viscosity at 25 °C is 42 ± 0.5 mPa s (Figure 5.4-7). Interestingly, this composition has characteristics that are remarkably similar to those of Cyanex 923,²⁷⁴ with a reported viscosity of 40 mPa s at 25 °C and 13.7 mPa s at 50 °C, and a freezing point between -5 to 0 °C.

Table 5.4-3: Density and Viscosity of TOPO: Phenol Mixtures at $\chi_{\text{TOPO}} = 0.33$ and 0.50

Temperature / °C	$\chi_{\text{TOPO}} = 0.33$		$\chi_{\text{TOPO}} = 0.50$	
	Density /g cm ⁻³	Viscosity /mPa s	Density /g cm ⁻³	Viscosity /mPa s
20	0.935	16.47	0.910	54.00
25	0.933	12.38		43.00
30	0.927	9.52	0.904	
40	0.923	6.18		22.00
50	0.912	4.35	0.890	15.02
60	0.905	3.24	0.883	10.76
70	0.902	2.53	0.877	
80	0.895	2.04	0.870	

5.4.4 Miscibility of TOPO:phenol ($\chi_{\text{TOPO}} = 0.50$) with Water

The ability to readily liquefy TOPO, forming mixtures with relatively wide liquid ranges and low viscosity, is an encouraging feature. Furthermore, the ambient temperature liquid TOPO:phenol mixtures all formed liquid–liquid biphases when contacted with water, suggesting that they could be used as a hydrophobic phase in liquid–liquid extraction. The stability of these liquids in contact with aqueous acid was examined. No TOPO was detected in aqueous hydrochloric acid solutions; this is consistent with the very low solubility of TOPO in water of 0.15 mg L^{-1} .^{251,288}

Table 5.4-4: Concentration of Phenol_a Leached to Aqueous Acid after Contacting with an Equal Volume of the TOPO: Phenol Eutectic ($\chi_{\text{TOPO}} = 0.5$) at 25 °C

Aqueous phase /M HCl	[phenol] _{aq} after contact	
	/g L ⁻¹	/mol L ⁻¹
0 (H ₂ O)	1.34	0.0142
0.0375	1.28	0.0136
0.0800	1.10	0.0117
1.5000	1.10	0.0117
3.0000	1.14	0.0121
^a Phenol solubility in water is 82 g L^{-1} . ²⁸⁹		

In contrast phenol was detected in the aqueous phases after contacting the 0.50 mole fraction TOPO:phenol eutectic with aqueous acid across a range of concentrations (0.04–3.00 M HCl), and the results are shown in Table 5.4-4. The aqueous phenol concentration is low in all cases ($1.10\text{--}1.34 \text{ g L}^{-1}$) compared to the high solubility of phenol in water (82 g L^{-1})²⁸⁹ and shows that phenol is preferentially concentrated in the liquid eutectic TOPO phase, with a distribution ratio of phenol to the TOPO eutectic in the order of $D = 75$.

This indicates that the liquefied TOPO could be used as an extractant for phenol from aqueous media, consistent with the reported applications of solventless extraction using TOPO impregnated membranes^{271,273,276} which is likely to be facilitated by the formation of a supported eutectic liquid. This also, intriguingly, raises the possibility to form hydrophobic eutectic liquids with other acidic hydrogen-bond donors such as the carboxylic acids that

have been targeted for extraction from fermentation broths^{267–270,290} using TOPO and also for parallel formation for hydrophobic eutectic liquids.^{155,156,255,258,259,291}

5.4.5 Liquid–Liquid Extraction Studies

The utility of these hydrophobic TOPO:phenol mixtures for liquid–liquid separations was tested using extraction of U(VI) from model acidic aqueous uranyl nitrate solutions as an example.

TOPO is an effective extractant for many metals, and phosphine oxides are ubiquitous components in many extraction processes for both primary processing of nuclear materials and radioactive waste treatment²⁹² including the commercial TRUEX and TRPO processes.²⁹³ Usually TOPO is used in a hydrocarbon diluent such as kerosene²⁹⁴ although the solubility limit of pure TOPO in kerosene of around 0.1–0.2 mol dm^{−3} restricts the extractant concentrations that can be achieved.²⁷² Recently the use of ionic liquid solvents for phosphine oxide-assisted partitioning of U(VI) has also been reported,^{295,296} building on earlier studies using hydrophobic ionic liquids as solvents for actinides and lanthanides.^{297–300}

A significant difference between TOPO dissolved in kerosene (with relatively low solubility limit) and the TOPO:phenol ($\chi_{\text{TOPO}} = 0.50$) system examined here is high TOPO content of *ca.* 80 wt % (1.875 mol L^{−1}). With this high TOPO concentration, we would anticipate a high extraction ratio comparable to that reported for the TRPO process using mixed trialkylphosphine oxides (equivalent to Cyanex 923) at 30 wt % in kerosene.

Uranyl extraction was examined from acidic aqueous uranyl nitrate, contacting 1 cm³ of TOPO:phenol ($\chi_{\text{TOPO}} = 0.50$, preequilibrated against the corresponding aqueous nitric acid solutions) with 1 cm³ of uranyl-containing feeds (shaken, 10 min, ambient temperature) with uranyl nitrate concentrations of 250 and 2350 ppm in nitric acid (0.01–3.00 M). The final concentrations of U(VI) in the aqueous acid after extraction were determined by UV–vis spectroscopic analysis after addition of 2-(5-bromo-2-pyridylazo)-5-(diethylamino)phenol (Br-PADAP) as the spectroscopic probe.²⁷⁵

UV–vis spectra of 5–50 ppm standards and the 250 ppm acidic uranyl nitrate stock solution before and after contact with the TOPO:phenol extractant are shown in Figure 5.4-8 along with a picture showing the appearance of each sample. Analysis was based on the absorbance maxima at 545 and 578 nm in the UV–vis spectra of uranyl-containing samples spiked with Br-PADAP indicator (Figure 5.4-8) and the detection limit for U(VI) estimated to be 0.50 ppm. The distinctive deep purple of the U(VI)-complexed Br-PADAP indicator at

250 ppm uranyl concentration, corresponding to the intense maxima in the UV–vis spectrum at 578 nm, decreases markedly as the uranyl concentration in the solution decreases.

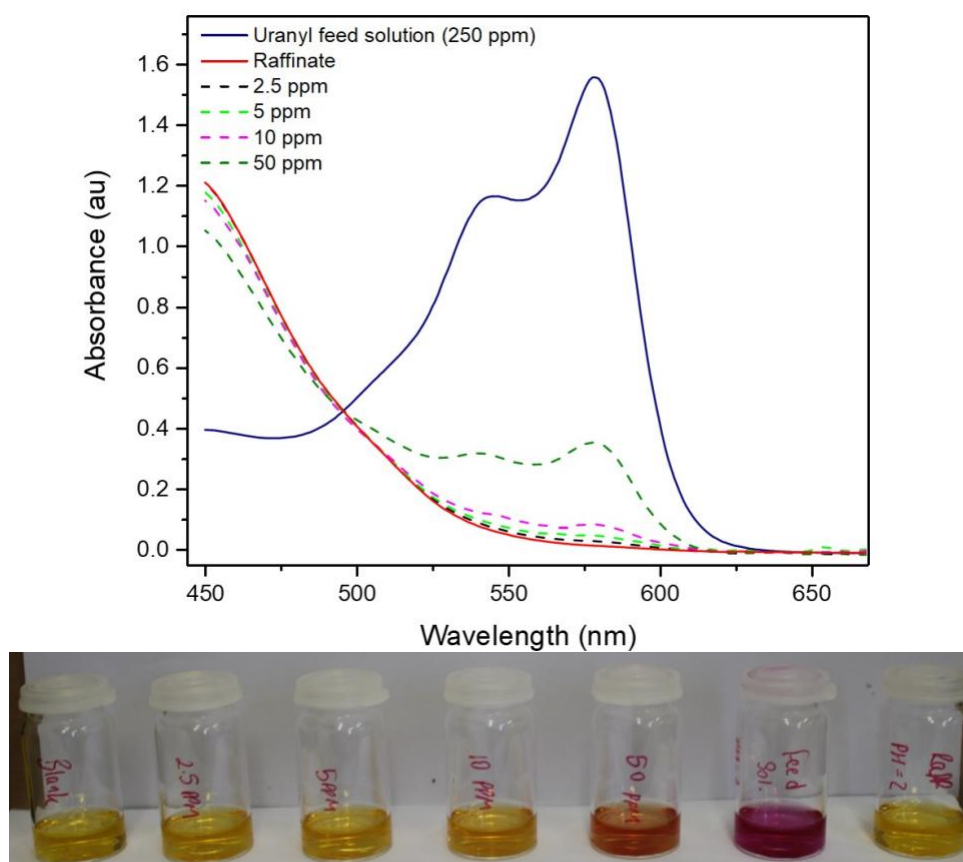


Figure 5.4-8: Transmission spectra (top) from the uranyl feed solution (250 ppm $[\text{UO}_2]_{2+}$) containing Br-PADAP indicator (blue) and the raffinate after contact with TOPO:phenol (red). Standard solutions containing 5–50 ppm uranyl in nitric acid are shown as dashed lines for comparison.

Single contact mixing of uranyl solutions (250 ppm) in 0.01, 1.00, and 3.00 M nitric acid with the TOPO:phenol ($\chi_{\text{TOPO}} = 0.50$) liquid extractant resulted in reduction in uranyl concentrations in the raffinate phase to the detection limit for the measurements in the experiments (Table 5.4-5). The colour and UV–vis spectra of raffinate solutions (spiked with Br-PADAP) after contact with TOPO:phenol were comparable to those of the blank acidic Br-PADAP solution.

When the uranyl concentration was increased 10-fold to 2350 ppm in 1.00 M HNO_3 (the acidity at which TOPO has maximum efficiency) complete extraction of uranyl species was also observed demonstrating the excellent extraction potential of the TOPO:phenol system in comparison to conventional TOPO-based extraction systems.^{297–300}

Table 5.4-5: Performance of TOPO:phenol ($\chi_{\text{TOPO}} = 0.50$) as a liquid extractant for uranyl nitrate from nitric acid at different acid and uranyl concentration in the aqueous feed.

Feed acidity (M)	[UO ₂₂₊] _{init} /ppm	[UO ₂₂₊] _{final} /ppm
0.01	250	<0.50
1.00	250	<0.50
3.00	250	<0.50
1.00	2350	<0.50

a 1cm³ TOPO:phenol ($\chi_{\text{TOPO}} = 0.50$) was pre-equilibrated with nitric acid solution, and then

Distribution ratios could be estimated from the initial and final [UO₂]₂₊ concentrations in the aqueous phase; however, because the final values are all around the limit of detection the results are unreliable. D was estimated to be at least 500 from the 250 ppm uranyl solutions, and from the 2350 ppm solution the corresponding value is *ca.* 5000. This efficient extraction and the estimated distribution ratios are similar to values of 1×10^3 reported for uranium partitioning in the TRPO extraction process²⁹³ from high salt and nitric acid solutions using a 30 wt % mixture of trialkylphosphine oxides in kerosene. In the TRPO process and here, the origin of the high uranyl extraction efficiencies is the high concentration of phosphine oxide in the extracting phase (30 wt % for TRPO and *ca.* 80 wt % in the TOPO:phenol ($\chi_{\text{TOPO}} = 0.50$) system here, which is between 10 and 20 times greater than that usually used in kerosene).²⁶⁶

The presence of phenol does not appear to have a role in the uranyl complexation and extraction, other than in generating the eutectic liquid composition. The UV–vis absorption spectra of uranyl nitrate (0.05 M) in TOPO:phenol ($\chi_{\text{TOPO}} = 0.50$) and 0.30 M TOPO in cyclohexane are shown in Figure 5.4-9. The two spectra are remarkably similar suggesting that the uranyl environments are identical in both solutions. These spectra are also comparable with previous studies from Babecki *et al.*³⁰¹ who identified the presence of two equatorial TOPO molecules and two axial oxygens in uranyl species extracted from nitric acid.

Furthermore, the extraction of uranyl ions to cyclohexane containing TOPO, or TOPO and phenol, was comparable whereas uranyl was not extracted from 1 M HNO₃ into cyclohexane containing only 0–2 M phenol ([UO₂]_{2+init} = 173 ppm, after contact [UO₂]_{2+final} = 172 ± 3.2). These results support the proposition that phenol has a negligible contribution to the uranium coordination environment, and acts solely as the liquefaction component of the TOPO-rich eutectic.

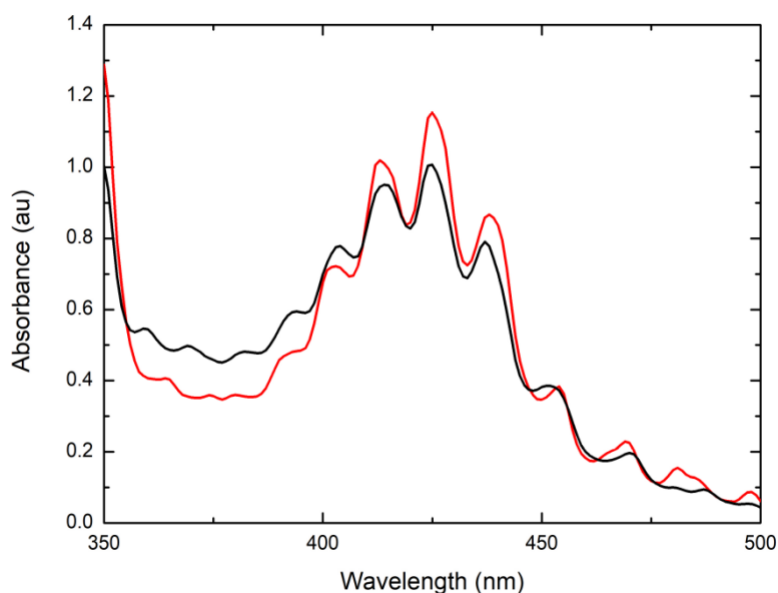


Figure 5.4-9: UV-vis spectra for 0.05 M uranyl nitrate solutions in 0.30 M TOPO/cyclohexane (black) and $\chi_{\text{TOPO}} = 0.5$ TOPO:phenol (red).

5.4.6 Sustainability

The results here are the first examples from a family of new hydrophobic eutectic liquids based on TOPO using phenol here as a hydrogen-bond donor. TOPO:phenol mixtures with TOPO contents between $\chi_{\text{TOPO}} = 0.15$ and 0.55 form liquids at room temperature which have a large melting point suppression. The tendency to form glasses prevents definitive identification of the eutectic point which appears, by extrapolation, to be around $\chi_{\text{TOPO}} = 0.33$ (1:2 TOPO:phenol). These liquids are hydrophobic and have low viscosity (in the range 10–50 mPa s) allowing their use as extraction phases for aqueous liquid–liquid extraction.

TOPO has many applications ranging from metal ion extraction, organic acid extraction, and preparation of metal chalcogenide nanoparticles for use in, among many applications, biomedical imaging.³⁰² The reported LD₅₀ (rat, oral) for TOPO is >2000 mg kg⁻¹,³⁰³ which is 10 times greater (less toxic) than that of Aliquat 336 (methyltriocetylammmonium chloride, LD₅₀ oral (rat) 223 mg kg⁻¹) previously used to form hydrophobic DES.^{155,256} In addition, the low solubility of TOPO in water (0.15 mg L⁻¹)^{288,304} limits bioavailability. As such, TOPO appears to be an interesting candidate to explore further to development of new hydrophobic solvents for extractions.

In comparison to the use of conventional hydrophobic organic solvents, when TOPO is required as an extractant or as a reagent (for example, as a capping agent in nanocrystal synthesis), forming a DES could lead to significant advantages through the reduction in the

volumes of solvents needed as the TOPO concentrations are much greater which can aid process intensification. For example, in the extraction of U(VI) ions from aqueous acid described here, the intrinsically high TOPO content in the liquids, results in liquid extractants that exhibit with high extraction efficiency with uranyl removed from the aqueous acid phase to the limit of detection, and the extraction ratio with an estimated to be at least 5×10^3 , comparable to that reported for optimized commercial TRPO process.²⁹³ This is achieved because the DES contains *ca.* 2 M (>80 wt %) of TOPO, compared to the maximum solubility below 0.5 M in kerosene. Comparably high phosphine oxide concentrations can only be achieved by changes in the formulation (mixed phosphine oxides in Cyanex 923²⁷⁴ and in the TRPO process²⁹³ with associated greater water solubility) or by use of solvents such as dichloromethane or benzene.

However, for use in metal extraction and recovery applications, the DES described here with phenol as the hydrogen-bond donor component is suboptimal due to potential problems with corrosivity and toxicity³⁰⁵ and specifically of relevance to nuclear waste processing,²⁵⁰ the potential to undergo nitration by concentrated nitric acid commonly used as a digestion medium. To address these concerns, more chemical and environmentally compatible hydrogen-bond donor components should be used. The initial screen in Chapter 4.4 highlighted a number of potential hydrogen-bond donor components with markedly lower potential environmental impacts that can be developed further.

Moreover, the generation of hydrophobic liquids on addition of phenol to solid TOPO suggests that liquefaction may have a significant role in the mechanism of extraction of phenol and organic carboxylic acids that can be applied to access lignin-derived phenolic platform chemicals from biooils³⁰⁶ and for the treatment of aqueous effluents from, e.g., coal liquefaction, coal gasification, biorefineries, and petrochemical production using TOPO-based materials,^{267–270,272,290} particularly with solventless solid-supported TOPO.^{271,273,276}

5.5 Conclusions

The first example of a low viscosity, hydrophobic DES based on trioctylphosphine oxide and its application to metal extraction from aqueous acid has been described. The high concentration of TOPO as an active extractant available in the DES enabled exceptional extraction efficiency for $[\text{UO}_2]_{2+}$ from aqueous acid media. Modulation of aqueous solubility of phenol through preferential DES formation was also observed which reveals the possibility for application in extraction of small organic hydrogen-bond donating organic molecules (phenols, alcohols, and carboxylic acids) from aqueous media through DES

formation without requiring additional organic solvents. Further work on TOPO based DES should focus on advancing the development of deep eutectic liquid extractants by developing analogous systems with hydrogen-bond donors characterized by (i) increased hydrophobicity, (ii) higher thermal stability, and (iii) synergistic extraction capabilities.

6 SUMMARY AND CONCLUSIONS

In chapter 2, high purity choline chloride/urea DES systems were re-examined to evaluate their true thermal stability, eutectic temperature and phase behaviour. A phase diagram was produced for the low-moisture content choline chloride:urea DES across the full compositional range using DSC and POM. It revealed a higher than reported melting point (31.8 °C) and a previously unreported phase in the choline chloride rich region of composition space corresponding to the crystal-crystal transformation from α -choline chloride to β -choline chloride. Viscosities and densities of the DES were measured and compared to current literature, finding that moisture content in the DES was the cause for discrepancies between data sets. Finally, a thermal stability study revealed that the DES was not thermally stable at temperatures of less than 100 °C, this is of particular interest as many literature examples use the DES at temperatures greater than this.

In Chapter 3, the liquid structures of ChCl:Ur and ChCl:Ox DES were examined using neutron scattering, identifying that extensive hydrogen-bonding interactions between all the components were present in the liquids and that choline-OH to chloride and to HBD hydrogen-bonding is less important than had been previously supposed based on simulation. Finally, examination of the speciation of zinc in ChCl:Ox from dissolution of ZnO in the DES was attempted however the results were inconclusive and it proved impossible to differentiate between plausible speciation as either $[\text{ZnCl}_4]^{2-}$ or $[\text{Zn}(\text{ox})_2]^{2-}$.

In chapter 4, a number of new potential DES forming systems were examined. Choline-imidazole mixtures were studied, however were found to have low thermal stability and poor melting point depression. A number of 1,3 di- and tetra-substituted ureas and thioureas were mixed with choline chloride and phase analysis of the mixtures was carried out. The literature recorded eutectic point for thiourea is $\chi_{\text{ChCl}} = 0.33$ choline chloride: thiourea, however, after full compositional phase analysis of the DES in this study, the eutectic point was found to be at $\chi_{\text{ChCl}} = 0.50$ choline chloride: thiourea. It was found that 1,3 di-substituted urea and thiourea had depressed melting points when mixed with choline chloride, but the tetra-substituted analogues did not. ChCl: carboxylic acid mixtures were evaluated for DES formation as a function of carboxylic acid pKa and the first case of non-ionic DES containing TOPO were identified.

Chapter 5 describes the detailed phase and property study of hydrophobic TOPO:phenol non-ionic DES and its application to uranyl ion partitioning from aqueous media. The DES were found to have low viscosities in comparison with DES based on quaternary ammonium

salts and the high concentration of TOPO that was present in the DES led to exceptional extraction efficiency of the $[\text{UO}_2]_{2+}$ ion from acidic aqueous media. Modulation of aqueous solubility of phenol through preferential DES formation was also observed opening up the possibility for application in extraction of small organic hydrogen-bond donating organic molecules.

7 BIBLIOGRAPHY

- 1 F. Guthrie, *Philos. Mag.*, 1884, **17**, 462–482.
- 2 W. H. Rodebush, *J. Am. Chem. Soc.*, 1918, **40**, 1204–1213.
- 3 U. Gala, H. Pham and H. Chauhan, *J. Dev. drugs*, 2013, **2**, 1–2.
- 4 P. W. Stott, A. C. Williams and B. W. Barry, *J. Control. release*, 1998, **50**, 297–308.
- 5 H. Hatcher, R. Planalp, J. Cho, F. . Torti and Torti S.V, *Cell. Mol. Sci.*, 2008, **65**, 1631–1652.
- 6 A. J. Rubya, K. D. Babub and K. N. Rajasekharanb, *Cancer Lett.*, 1995, **94**, 79–83.
- 7 L. K. Wolf, *Chem. engineering news*, 2012, **90**, 44–46.
- 8 N. R. Goud, K. Suresh, P. Sanphui and A. Nangia, *Int. J. Pharm.*, 2012, 439, 63–72.
- 9 S. Kim, S. Kim and S. Lee, *Ann. N. Y. Acad. Sci.*, 2009, **1171**, 196–201.
- 10 J. Hwang, Y. Lee, J. Shin and O. Jin, *Ann. N. Y. Acad. Sci.*, 2009, **1171**, 415–420.
- 11 M. Verdrengh, L. V. Collins, P. Bergin and A. Tarkowski, *Microbes Infect.*, 2004, **6**, 86–92.
- 12 M. Landauer, *J. Basic Microbiol.*, 2006, **46**, 329–335.
- 13 J. Xi and R. Guo, *J. Solution Chem.*, 2009, **38**, 1588–1600.
- 14 G. A. Chadwick, *Prog. Mater. Sci.*, 1963, **12**, 99–180.
- 15 H. W. Roberts, D. W. Berzins, B. K. Moore and D. G. Charlton, *J. Prosthodont.*, 2009, **18**, 188–194.
- 16 W. A. Brantley and A. B. Carr, *Int. J. Prosthodont.*, 1991, **4**, 265–275.
- 17 R. N. Lyon, *Liquid-metals handbook*, US Government printing office, Washington, DC, 1950.
- 18 Intellectual Property Office (UK), GB191321689, 1914.
- 19 J. R. Wilson, *Metall. Rev.*, 1965, **10**, 381–590.
- 20 C. Y. Ho and T. . Chu, *Electrical resistivity and thermal conductivity of nune selected AISI stainless steels*, 1977.
- 21 <https://periodic.lanl.gov/87.shtml>, Date accessed: 25/04/2019.
- 22 G. F. Strouse, *Standard Reference Material 1751: Gallium Melting-Point Standard*, 2004.
- 23 United States Patent office, 3,150,901, 1964.
- 24 T. Liu, P. Sen and C.-J. Kim, *J. microelectromechanical Syst.*, 2012, **21**, 2012.
- 25 A. Cao, P. Yuen and L. Lin, *J. Microelectromechanical Syst.*, 2007, **16**, 700–708.
- 26 S. J. Mazlouman, X. J. Jiang, A. N. Mahanfar, C. Menon and R. G. Vaughan, *IEEE T*

- ANTENN PROPAG*, 2011, **59**, 4406–4412.
- 27 K. A. Shaikh, S. Li and C. Liu, *J. Microelectromechanical Syst.*, 2008, **17**, 1195–1203.
 - 28 H. Ma and Æ. J. C. Suhling, 2009, 1141–1158.
 - 29 *EU Directive, 2010, “Restriction of the Use of Certain Hazardous Substances in Electrical and Electronic Equipment*, Brussels, 2010.
 - 30 N. Lee, *Solder. Surf. Mt. Technol.*, 1997, **9**, 65–69.
 - 31 Y. Yao, X. Long and L. M. Keer, *Appl. Mech. Rev.*, 2017, **69**, 040802.
 - 32 H. R. Kotadia, P. D. Howes and S. H. Mannan, *Microelectron. Reliab.*, 2014, **54**, 1253–1273.
 - 33 L. Zhang, C. W. He, Y. H. Guo, J. G. Han, Y. W. Zhang and X. Y. Wang, *Microelectron. Reliab.*, 2012, **52**, 559–578.
 - 34 K. R. Seddon, *Kinet. Catal.*, 1996, **37**, 693.
 - 35 K. R. Seddon, *J. Chem. Technol. Biotechnol.*, 1997, **68**, 351–356.
 - 36 T. Welton, *Chem. Rev.*, 1999, **99**, 2071–2083.
 - 37 P. Wasserscheid and T. Welton, *Ionic liquids in Synthesis*, Wiley-VCH, Weinheim, 2002, vol. 7.
 - 38 M. S. Miran, T. Yasuda and M. Watanabe, *Phys. Chem. Chem. Phys.*, 2012, **14**, 5178–5186.
 - 39 M. Yoshizawa, W. Xu and C. A. Angell, *J. Am. Chem. Soc.*, 2003, **125**, 15411–15419.
 - 40 S. P. Kelley, A. Narita, J. D. Holbrey, K. D. Green, W. M. Reichert and R. D. Rogers, *Cryst. growth Des.*, 2013, **13**, 956–975.
 - 41 J. Estager, J. D. Holbrey and M. Swadźba-Kwaśny, *Chem. Soc. Rev.*, 2014, **43**, 37–39.
 - 42 J. P. Hallett and T. Welton, *Chem. Rev.*, 2011, **111**, 3508–3576.
 - 43 Q. Zhang, K. De Oliveira Vigier, S. Royer and F. Jérôme, *Chem. Soc. Rev.*, 2012, **41**, 7108–7146.
 - 44 D. R. Macfarlane, A. L. Chong and M. Forsyth, *Faraday Discuss.*, 2018, **206**, 9–28.
 - 45 A. P. Abbott, D. Boothby, G. Capper, D. L. Davies and R. K. Rasheed, *J. Am. Chem. Soc.*, 2004, **126**, 9142–9147.
 - 46 J. S. Wilkes, *Green Chem.*, 2002, **4**, 73–80.
 - 47 W. Ramsey, *Philos. Mag.*, 1876, **11**, 269.
 - 48 P. Walden, *Bull. St. Petersburg. Imp. Acad. Sci.*, 1914, **8**, 405–422.
 - 49 C. L. Hussey, *Adv. Molten Salt Chem.*, 1983, **5**, 185.
 - 50 T. Welton, *Biophys. Rev.*, 2018, **10**, 691–706.

- 51 F. H. Hurley and T. P. Wier, *J. Electrochem. Soc.*, 1951, **98**, 203–206.
- 52 https://pubchem.ncbi.nlm.nih.gov/compound/aluminium_chloride, Date accessed: 07/05/2019.
- 53 J. Robinson and R. A. Osteryoung, *J. Am. Chem. Soc.*, 1979, **101**, 323–327.
- 54 C. L. Hussey, *Pure Appl. Chem.*, 1988, **60**, 1763–1772.
- 55 A. A. Fannin, D. A. Floreani, L. A. King, J. S. Landers, B. J. Piersma, D. J. Stech, R. L. Vaughn, J. S. Wilkes and J. L. Williams, *J. Phys. Chem.*, 1984, **88**, 2614–2621.
- 56 J. D. Holbrey and K. R. Seddon, *Clean Prod. Process. 1*, 1999, **1**, 223–236.
- 57 R. T. Carlin and J. S. Wikes, *Chemistry and Speciation in Room- Temperature Chloroaluminate Molten Salts*, VCH Publisher Inc., New York, Chemistry., 1994.
- 58 J. Yoke, J. Weiss and G. Tollin, *Inorg. Chem.*, 1962, **2**, 1210–1216.
- 59 F. N. Jones, *J. Org. Chem.*, 1967, **32**, 1667–1668.
- 60 G. W. Parshall, *J. Am. Chem. Soc.*, 1972, **94**, 11–14.
- 61 J. F. Knifton, *J. Mol. Catal.*, 1987, **43**, 65–77.
- 62 E. J. House, *Inorganic Chemistry*, Academic Press, Oxford, 2nd edn., 2012.
- 63 C. Hardacre, A. R. W. Murphy, A. K. R. Seddon, G. Srinivasan and M. Swad, *Aust. J. Chem.*, 2010, **63**, 845–848.
- 64 J. Yang, P. Tian, W. Xu, B. Xu and S. Liu, *Thermochim. Acta*, 2004, **412**, 1–5.
- 65 M. K. Carpenter and M. W. Verbrugge, *J. Mater. Res.*, 1994, **9**, 2584–2591.
- 66 S. P. Wicelinski, R. J. Gale, K. M. Pamidimukkala and R. A. Laine, *Anal. Chem.*, 1988, **60**, 2228–2232.
- 67 R. J. Gale and B. Rouge, *Spectrochim. Acta*, 1989, **45**, 759–762.
- 68 S. P. Wicelinski, R. J. Gale and J. S. Wilkes, *Thermochim. Acta*, 1988, **126**, 255–263.
- 69 S. P. Wicelinski, R. J. Gale and J. S. Wilkes, *J. Electrochem. Soc.*, 1983, **134**, 262–263.
- 70 Y. Lin and I. Sun, *Electrochim. Acta*, 1999, **44**, 2771–2777.
- 71 F. Coleman, G. Srinivasan and M. Swadzba-Kwasny, *Angew. Chem - Int. Ed.*, 2013, **52**, 12582–12586.
- 72 I. Krossing, J. M. Slattery, C. Daguenet, P. J. Dyson, A. Oleinikova, H. Weinga, D.-Freiburg, S. Inge, Ä. P. Fe, C.- Lausanne, P. Chemistry and R. V Bochum, *J. Am. Chem. Soc.*, 2006, **128**, 13427–13434.
- 73 P. M. Dean, J. M. Pringle, D. R. Macfarlane and P. M. Dean, *Phys. Chem. Chem. Phys.*, 2010, **12**, 9144–9153.
- 74 M. Lijewski, J. M. Hogg, M. Swadźba-kwaśny, P. Wasserscheid and M. Haumann, *RSC Adv.*, 2017, **7**, 27558.
- 75 J. M. Hogg, L. C. Brown, K. Matuszek, P. Latos, A. Chrobok and M. Swadźba-

- kwaśny, *Dalt. Trans.*, 2017, **46**, 11561.
- 76 J. M. Hogg, F. Coleman, A. Ferrer-Ugalde, M. P. Atkins and M. Swadźba-Kwaśny, *Green Chem.*, 2015, **17**, 1831–1841.
 - 77 K. Matuszek, A. Chrobok, J. Hogg, F. Coleman and M. Swadźba-Kwaśny, *Green Chem.*, 2015, **17**, 4255–4262.
 - 78 S. Coffie, J. M. Hogg, L. Cailler, A. Ferrer-ugalde, R. W. Murphy, J. D. Holbrey, F. Coleman and M. Swadz, *Angew. Chem - Int. Ed.*, 2015, **54**, 14970.
 - 79 K. Matuszek, S. Coffie and A. Chrobok, *Catal. Sci. Technol.*, 2017, **7**, 1045–1049.
 - 80 J. L. Atwood and W. R. Newberry, *J. Organomet. Chem.*, 1972, **42**, 77–79.
 - 81 J. L. Atwood and J. D. Atwood, in *Advances in Chemistry*, Amrican Chemical Society, Washington, DC, 1976, pp. 112–127.
 - 82 D. R. Bond, G. E. Jackson, H. C. Jogo, M. N. Hofmeyr, T. A. Modro and L. R. Nassimbeni, *J. Chem. Soc. Chem. Commun.*, 1989, **24**, 1910–1911.
 - 83 H. M. A. Abood, A. P. Abbott, D. Ballantyne and K. S. Ryder, *Chem. Commun.*, 2011, **47**, 3523–3525.
 - 84 F. Coleman, G. Srinivasan and M. Swadzba-Kwasny, *Angew. Chem - Int. Ed.*, 2013, **52**, 12582–12586.
 - 85 D. R. Macfarlane and K. R. Seddon, *Aust. J. Chem.*, 2007, **60**, 3–5.
 - 86 T. L. Greaves, A. Weerawardena, C. Fong, I. Krodkiewska and C. J. Drummond, *J. Phys. Chem. B*, 2006, **110**, 22479.
 - 87 T. L. Greaves and C. J. Drummond, *Chem. Mater.*, 2008, **108**, 206.
 - 88 S. Gabriel and J. Weiner, *S. Ber*, 1888, **21**, 2669.
 - 89 D. R. Macfarlane, M. Forsyth, E. I. Izgorodina, A. P. Abbott and K. Fraser, *PCCP*, 2009, **11**, 4962–4967.
 - 90 W. Xu, E. I. Cooper and C. A. Angell, *J. Phys. Chem. B*, 2003, **107**, 6170–6178.
 - 91 C. A. Angell, N. Byrne and J. Belieres, *Acc. Chem. Res.*, 2007, **40**, 1228–1236.
 - 92 W. A. Adams and K. J. Laidler, *Can. J. Chem.*, 1968, **46**, 1978.
 - 93 A. N. Campbell and E. T. Van der Kouwe, *Can. J. Chem.*, 1968, **46**, 1968.
 - 94 C. Zhao, G. Burrell, A. A. J. Torriero, F. Separovic, N. F. Dunlop, D. R. Macfarlane and A. M. Bond, *J. Phys. Chem. B*, 2008, **112**, 6923–6936.
 - 95 M. Yoshizawa, W. Xu and C. A. Angell, *J. Am. Chem. Soc.*, 2003, **125**, 15411–15419.
 - 96 K. M. Johansson, E. I. Izgorodina, M. Forsyth, D. R. Macfarlane and K. R. Seddon, *PCCP*, 2008, **10**, 2972–2978.
 - 97 J. Stoimenovski, E. I. Izgorodina and D. R. Macfarlane, *PCCP*, 2010, **12**, 10341–10347.

- 98 J. A. Mccune, A. H. Turner, F. Coleman, C. M. White, S. K. Callear, T. G. A. Youngs, M. Swadźba-Kwaśny and J. D. Holbrey, *Phys. Chem. Chem. Phys.*, 2015, **17**, 6767.
- 99 P. M. Bayley, A. S. Best, D. R. Macfarlane and M. Forsyth, *PCCP*, 2011, **13**, 4632–4640.
- 100 K. Fujita, R. Macfarlane and M. Forsyth, *Chem. Commun.*, 2005, 4804–4806.
- 101 D. Constatinescu, C. Herrmann and H. Weingartner, *Phys. Chem. Chem. Phys.*, 2010, **12**, 1756–1763.
- 102 M. Seter, A. M. J. Thomson, B. A. Chong, D. R. Macfarlane and M. F. A, *Aust. J. Chem.*, 2013, **66**, 921–929.
- 103 S. Theivaprakasam, D. R. Macfarlane and S. Mitra, *Electrochim. Acta*, 2015, **180**, 737–745.
- 104 M. Francisco, A. van den Bruinhorst and M. C. Kroon, *Angew. Chem - Int. Ed.*, 2013, **52**, 3074–3085.
- 105 E. L. Smith, A. P. Abbott and K. S. Ryder, *Chem. Rev.*, 2014, **114**, 11060–11082.
- 106 A. P. Abbott, R. C. Harris, F. Holyoak, G. Frisch, J. Hartley and G. R. T. Jenkin, *Green Chem.*, 2015, **17**, 2172–2179.
- 107 N. López-Salas, D. Carriazo, M. C. Gutiérrez, M. L. Ferrer, C. O. Ania, F. Rubio, A. Tamayo, J. L. G. Fierro and F. Del Monte, *J. Mater. Chem. A*, 2016, **4**, 9146–9159.
- 108 H. G. Liao, Y. X. Jiang, Z. Y. Zhou, S. P. Chen and S. G. Sun, *Angew. Chem - Int. Ed.*, 2008, **47**, 9100–9103.
- 109 M. C. Gutiérrez, D. Carriazo, C. O. Ania, J. B. Parra, M. L. Ferrer and F. Del Monte, *Energy Environ. Sci.*, 2011, **4**, 3535–3544.
- 110 O. S. Hammond, K. J. Edler, D. T. Bowron and L. Torrente-murciano, *Nat. Commun.*, 2017, **8**, 1–7.
- 111 H. C. Hu, Y. H. Liu, B. Le Li, Z. S. Cui and Z. H. Zhang, *RSC Adv.*, 2015, **5**, 7720–7728.
- 112 Y. Liu, J. B. Friesen, J. B. Mcalpine, D. C. Lankin, S. Chen and G. F. Pauli, *J. Nat. Prod.*, 2018, **81**, 679.
- 113 H. G. Morrison, C. C. Sun and S. Neervannan, *Int. J. Pharm.*, 2009, **378**, 136–139.
- 114 Q. Zhang, K. Vigier and S. Royer, *Chem. Soc. Rev.*, 2012, **41**, 7108–7146.
- 115 A. P. Abbott, G. Capper, D. L. Davies, R. K. Rasheed and V. Tambyrajah, *Chem. Commun. (Camb)*, 2003, **1**, 70–71.
- 116 A. P. Abbott, G. Capper, D. L. Davies and R. K. Rasheed, *Chem. - Eur. J.*, 2004, **10**, 3769–3774.
- 117 A. P. Abbott, K. S. Ryder and U. König, *Trans. IMF*, 2008, **86**, 196–204.

- 118 A. P. Abbott, G. Capper, D. L. Davies, H. L. Munro, R. K. Rasheed and V. Tambyrajah, *Chem. Commun.*, 2001, 2010–2011.
- 119 J. Pierre, S. Mitallrques, U. E. R. De Chlmre, C. D. S. Charles and N. Ki, *Thermochim. Acta*, 1988, **127**, 223–236.
- 120 P. Gaune, M. Nabavian, M. Gaune-Escard and J. Bros, *Thermochim. Acta*, 1987, **111**, 37–47.
- 121 <http://www.webofknowledge.com>, Date accessed: 07/02/2019.
- 122 A. Paiva, R. Craveiro, I. Aroso, M. Martins, R. L. Reis and A. R. C. Duarte, *Sustain. Chem. Eng.*, 2014, **2**, 1063–1071.
- 123 D. A. Alonso, R. Chinchilla, I. M. Pastor and D. J. Ramón, *European J. Org. Chem.*, 2016, 612–632.
- 124 R. D. Rogers and G. Gurau, *PNAS*, 2018, **115**, 10999.
- 125 A. Banerjee, K. Ibsen, T. Brown, R. Chen, C. Agatemor and S. Mitragotri, *PNAS*, 2018, **115**, 7296.
- 126 M. A. R. Martins, S. P. Pinho and J. A. P. Coutinho, *J. Solution Chem.*, 2019, **48**, 962.
- 127 A. P. Abbott, J. C. Barron, K. S. Ryder and D. Wilson, *Chem. - Eur. J.*, 2007, **13**, 6495–6501.
- 128 M. A. Kareem, F. S. Mjalli, M. A. Hashim and I. M. Al Nashef, *J. Eng. Chem. Data*, 2010, **55**, 4632–4637.
- 129 X. Baokou and M. Anouti, *J. Phys. Chem. C*, 2015, **119**, 970–979.
- 130 S. Zahn, B. Kirchner and D. Mollenhauer, *ChemPhysChem*, 2016, **17**, 3354–3358.
- 131 M. Gilmore, L. M. Moura, A. H. Turner, M. Swadźba-kwaśny, S. K. Callear, A. Jade, O. A. Scherman, J. D. Holbrey, M. Gilmore, L. M. Moura, A. H. Turner and M. Swad, *J. Chem. Phys.*, 2018, **148**, 193823.
- 132 J. M. Hogg, PhD Thesis, Queen’s University Belfast, 2017.
- 133 P. Hu, R. Zhang, X. Meng, H. Liu, C. Xu and Z. Liu, *Inorg. Chem.*, 2016, **55**, 2374.
- 134 M. Hog, M. Schneider, G. Studer, S. A. Fçhrenbacher, H. Scherer and I. Krossing, *Chem. - A Eur. J.*, 2017, **23**, 11054.
- 135 J. Estager, P. Nockemann, K. R. Seddon, M. Swadźba-Kwaśny and S. Tyrrell, *Inorg. Chem.*, 2011, **50**, 5258–5271.
- 136 J. S. Wilkes, *J. Mol. Catal. A*, 2004, **214**, 11–17.
- 137 O. S. Hammond, D. T. Bowron and K. J. Edler, *Green Chem.*, 2016, **18**, 2736.
- 138 M. Gilmore, E. N. Mccourt, F. Connolly, P. Nockemann and J. D. Holbrey, *ACS Sustain. Chem. Eng.*, 2018, **6**, 17323.
- 139 D. C. Apperley, C. Hardacre, P. Licence, R. W. Murphy, N. V Plechkova, K. R.

- Seddon, G. Srinivasan and M. Swad, *Dalton Trans.*, 2010, **39**, 8679–8687.
- 140 J. D. Holbrey and K. R. Seddon, *J. Chem. Soc. Dalt. Trans.*, 1999, 2133–2139.
- 141 X. Meng, K. Ballerat-Busserolles, P. Husson and J.-M. Andanson, *New J. Chem.*, 2016, **40**, 4492–4499.
- 142 P. G. Debenedetti and F. H. Stillinger, *Nature*, 2001, **410**, 259–267.
- 143 K. L. J. B.M, M. Vis, A. van den Bruinhorst, A. C. C. Esteves and R. Tuinier, *Chem. Commun.*, 2018, **54**, 13351–13354.
- 144 A. P. Abbott, *ChemPhysChem*, 2004, **5**, 1242.
- 145 A. P. Abbott, G. Capper and S. Gray, *ChemPhysChem*, 2006, **7**, 803.
- 146 J. . Segur and H. . Oberstar, *Ind. Eng. Chem. Res.*, 1951, **43**, 2117.
- 147 A. Reza and R. Buchner, *J. Mol. Liq.*, 2017, **225**, 689–695.
- 148 A. Zhu, T. Jiang, B. Han, J. Zhang, Y. Xie and X. Ma, *Green Chem.*, 2007, **9**, 169–172.
- 149 J. A. Sirviö, M. Visanko and H. Liimatainen, *Green Chem.*, 2015, **17**, 3401–3406.
- 150 A. P. Abbott, G. Frisch, S. J. Gurman, A. R. Hillman, J. Hartley, F. Holyoak and K. S. Ryder, *Chem. Commun. (Camb)*, 2011, **47**, 10031–10033.
- 151 J. Chang, H. Chen, S. Xu and M. C. Lin, *J. Phys. Chem.*, 2007, **111**, 6789–6797.
- 152 T. Kakumoto, K. Sai and A. Imamura, *J. Phys. Chem.*, 1987, **91**, 2366.
- 153 J. P. Chen and K. Isa, *J. Mass Spectrom. Soc. Japan*, 1998, **46**, 299.
- 154 P. M. Schaber, J. Colson, S. Higgins, D. Thielen, B. Anspach and J. Brauer, *Thermochim. Acta*, 2004, **424**, 131–142.
- 155 D. J. G. P. van Osch, L. F. Zubeir, A. van den Bruinhorst, M. A. A. Rocha and M. C. Kroon, *Green Chem.*, 2015, **17**, 4518–4521.
- 156 B. D. Ribeiro, C. Florindo, L. C. Iff, M. A. Z. Coelho and I. M. Marrucho, *ACS Sustain. Chem. Eng.*, 2015, **3**, 2469–2477.
- 157 W. C. Su, D. Shan, H. Wong and M. H. Li, *J. Chem. Eng. Data*, 2009, **54**, 1951–1955.
- 158 D. Shah and F. S. Mjalli, *Phys. Chem. Chem. Phys.*, 2014, **16**, 23900.
- 159 S. K. Shukla and J. Mikkola, *Phys. Chem. Chem. Phys.*, 2018, **20**, 24591–24601.
- 160 Y. Zhang, X. Ji and X. Lu, *Renew. Sustain. Energy Rev.*, 2018, **97**, 436–455.
- 161 C. Cadena, J. L. Anthony, J. K. Shah, T. I. Morrow, J. F. Brennecke and E. J. Maginn, *J. Am. Chem. Soc.*, 2004, **126**, 5300.
- 162 X. Li, M. Hou, B. Han, X. Wang and L. Zou, *J. Chem. Eng. Data*, 2008, **53**, 548–550.
- 163 W. Li, Z. Zhang, B. Han, S. Hu, J. Song, Y. Xie and X. Zhou, *Green Chem.*, 2008, **10**, 1142–1145.

- 164 L. M. Moura, T. Moufawad, M. Ferreira, H. Bricout, S. Tilloy, E. Monflier, M. F. Costa Gomes, D. Landy and S. Fourmentin, *Environ. Chem. Lett.*, 2017, **15**, 747–753.
- 165 J. Garcia-Alvarez, *Eur. J. Inorg. Chem.*, 2015, **31**, 5147–5157.
- 166 P. Liu, J. Hao, L. Mo and Z. Zhang, *RSC Adv.*, 2015, **5**, 48675–48704.
- 167 N. Azizi and M. Alipour, *J. Mol. Liq.*, 2015, **206**, 268–271.
- 168 W. Li, Z. Cao and W. He, *ACS Sustain. Chem. Eng.*, 2019, **7**, 2169–2175.
- 169 A. Selenols and Q. Chemical, *Chem. - A Eur. J.*, 2004, **10**, 3649–3656.
- 170 P. Maity, B. Paroi and B. C. Ranu, *Org. Lett.*, 2017, **19**, 5748–5751.
- 171 D. V Wagle, H. Zhao and G. A. Baker, *Acc. Chem. Res.*, 2014, **47**, 2299.
- 172 C. Letters, N. G. Catalysts, C. Monoxide, M. Haruta, T. Kobayashi, H. Sano and N. Yamada, *Chem. Lett.*, 1987, **16**, 405–408.
- 173 H. Liao, Y. Jiang, Z. Zhou, S. Chen and S. Sun, *Angew. Chem - Int. Ed.*, 2008, 9100–9103.
- 174 L. Duan, L. Dou, L. Guo, P. Li and E. Liu, *ACS Sustain. Chem. Eng.*, 2016, **4**, 2405–2411.
- 175 M. W. Nam, J. Zhao, M. S. Lee, J. H. Jeong and J. Lee, *Green Chem.*, 2015, **17**, 1718–1727.
- 176 C. G. González and E. G. Wilson, *Flavour Fragr J*, 2018, **33**, 91–96.
- 177 A. P. Abbott, G. Capper, D. L. Davies, P. Shikotra, G. Capper, D. L. Davies, P. S. Processing, A. P. Abbott, G. Capper, D. L. Davies and P. Shikotra, *Trans. Inst. Min. Met. C*, 2013, **115**, 15–18.
- 178 G. R. T. Jenkin, A. Z. M. Al-Bassam, R. C. Harris, A. P. Abbott, D. J. Smith, D. A. Holwell, R. J. Chapman and C. J. Stanley, *Miner. Eng.*, 2015, Ahead of Print.
- 179 A. P. Abbott, G. Capper, D. L. Davies, K. J. McKenzie and S. U. Obi, *J. Chem. Eng. Data*, 2006, **51**, 1280–1282.
- 180 A. P. Abbott, G. Capper, D. L. Davies, R. K. Rasheed and P. Shikotra, *Inorg. Chem.*, 2005, **44**, 6497–6499.
- 181 A. P. Abbott, G. Frisch, J. Hartley and K. S. Ryder, *Green Chem.*, 2011, **13**, 471.
- 182 A. P. Abbott, J. Collins, I. Dalrymple, R. C. Harris, R. Mistry, F. Qiu, J. Scheirer and W. R. Wise, *Aust. J. Chem.*, 2009, **62**, 341–347.
- 183 A. P. Abbott, G. Frisch, J. Hartley and K. S. Ryder, *Green Chem.*, 2011, **13**, 471.
- 184 T. Phuong, T. Pham, C. Cho and Y. Yun, *Water Res.*, 2010, **44**, 352–372.
- 185 D. Zhao, Y. Liao, Z. Zhang and I. Liquids, *Clean*, 2007, **35**, 42–48.
- 186 K. Shahbaz, F. S. Mjalli, M. a. Hashim and I. M. Alnashef, *Thermochim. Acta*, 2011, **515**, 67–72.
- 187 Z. Liu and H. Li, *Hydrometallurgy*, 2015, **155**, 29–43.

- 188 A. Seidel and Y. Zimmels, *Chem. Eng. Sci.*, 1998, **53**, 3835–3852.
- 189 S. V. Gladyshev, A. Akcil, R. A. Abdulvaliyev, E. A. Tastanov, K. O. Beisembekova, S. S. Temirova and H. Deveci, *Miner. Eng.*, 2015, **74**, 91–98.
- 190 I. Tsuboi, S. Kasai, E. Kunugita and I. Komasaawa, *J. Chem. Eng. Japan*, 1991, **24**, 15–20.
- 191 United States Patent office, 4,559,216, 1985.
- 192 A. P. Abbott, K. El Ttaib, G. Frisch, K. J. Mckenzie and K. S. Ryder, *Phys. Chem. Chem. Phys.*, 2009, **11**, 4269.
- 193 G. Garcia, S. Aparicio, R. Ullah and M. Atilhan, *Energy & Fuels*, 2015, **29**, 2616–2644.
- 194 W. Guo, W. Wu, S. Ren, S. Tian and K. N. Marsh, *Green Chem.*, 2013, **15**, 226–229.
- 195 K. Pang, Y. Hou, W. Wu, W. Guo and K. N. Marsh, *Green Chem.*, 2012, **14**, 2398.
- 196 T. M. Seddon K, Stark A, in *Clean Solvents*, 2002, pp. 34–49.
- 197 U. N. Yadav and G. S. Shankarling, *J. Mol. Liq.*, 2014, **195**, 188–193.
- 198 E. R. Cooper, C. D. Andrews, P. S. Wheatley, P. B. Webb, P. Wormald and R. E. Morris, *Nature*, 2004, **430**, 1012–1016.
- 199 E. R. Parnham, E. A. Drylie, P. S. Wheatley, A. M. Z. Slawin and R. E. Morris, *Angew. Chem - Int. Ed.*, 2006, **45**, 4962–4966.
- 200 D. Carriazo, M. C. Guti, M. L. Ferrer and F. Monte, *Chem. - A Eur. J.*, 2010, **22**, 6146–6152.
- 201 H. Liao, Y. Jiang, Z. Zhou, S. Chen and S. Sun, *Angew. Chem*, 2008, **120**, 9240–9243.
- 202 H. Zhao, G. A. Baker and S. Holmes, *Journal Mol. Catal. B, Enzym.*, 2011, **72**, 163–167.
- 203 F. Messa, S. Perrone, M. Capua, F. Tolomeo, L. Troisi and A. Salomone, *Chem. Commun.*, 2018, **4**, 8100–8103.
- 204 V. . Mirnyi, V. . Prisyazhnii and U. . Pushkarev, *Ukr. Khimicheskii Zhurnal (Russian Ed.)*, 1987, **53**, 1027.
- 205 V. Petrouleas and R. M. Lemmon, *Jorunal Phys. c*, 2017, **2243**, 1–5.
- 206 J. Jacquemin, P. Husson, A. A. H. Padua and V. Majer, *Green Chem.*, 2006, **8**, 172.
- 207 A. Yadav and S. Pandey, *J. Chem. Eng. Data*, 2014, **59**, 2221–2229.
- 208 Y. Xie, H. Dong, S. Zhang, X. Lu and X. Ji, *J. Chem. Eng. Data*, 2014, **59**, 3344–3352.
- 209 N. Delgado-mellado, M. Larriba, P. Navarro, V. Rigual, M. Ayuso, J. García and F. Rodríguez, *J. Mol. Liq.*, 2018, **260**, 37–43.
- 210 W. H. R. Shaw and J. J. Bordeaux, *J. Am. Chem. Soc.*, 1955, **77**, 4729.

- 211 S. P. Simeonov and C. A. M. Afonso, *RSC Adv.*, 2016, **6**, 5485–5490.
- 212 D. E. Crawford, L. A. Wright, S. L. James and A. P. Abbott, *Chem. Commun.*, 2016, **52**, 4215–4218.
- 213 A. P. Abbott, R. C. Harris, K. S. Ryder, C. D’Agostino, L. F. Gladden and M. D. Mantle, *Green Chem.*, 2011, **13**, 82–90.
- 214 C. D. Agostino, R. C. Harris, A. P. Abbott, F. Gladden and M. D. Mantle, *Phys. Chem. Chem. Phys.*, 2011, **13**, 21383–21391.
- 215 O. Russina, S. De Santis and L. Gontrani, *RSC Adv.*, 2016, **6**, 34737.
- 216 D. V Wagle, G. A. Baker and E. Mamontov, *J. Phys. Chem. Lett.*, 2015, **6**, 2924.
- 217 O. S. Hammond, D. T. Bowron, A. J. Jackson, T. Arnold, A. Sanchez-Fernandez, N. Tsapatsaris, V. Garcia Sakai and K. J. Edler, *J. Phys. Chem. B*, 2017, **121**, 7473.
- 218 S. Zahn, *Phys. Chem. Chem. Phys.*, 2017, **19**, 4041–4047.
- 219 R. Stefanovic, M. Ludwig, G. B. Webber, R. Atkin and A. J. Page, *Phys. Chem. Chem. Phys.*, 2017, **19**, 3297.
- 220 C. R. Ashworth, P. A. Hunt, T. Welton and R. P. Matthews, *Phys. Chem. Chem. Phys.*, 2016, **18**, 18145–18160.
- 221 D. V. Wagle, C. A. Deakyne and G. A. Baker, *J. Phys. Chem. B*, 2016, acs.jpcc.6b04750.
- 222 S. L. Perkins, P. Painter and C. M. Colina, *J. Chem. Eng. Data*, 2014, **59**, 3652.
- 223 C. . Arauo, J. A. . Coutinho, M. . Nolasco, S. . Parker, P. J. . Ribeiro-Claro, S. Rudic, B. I. . Soares and P. D. Vaz, *Phys. Chem. Chem. Phys.*, 2017, **19**, 17998.
- 224 A. H. Turner and J. D. Holbrey, *J. Solution Chem.*, 2015, **44**, 621.
- 225 C. Hardacre, J. D. Holbrey, C. L. Mullan, M. Nieuwenhuyzen, T. G. A. Youngs, D. T. Bowron and S. J. Teat, *Phys. Chem. Chem. Phys.*, 2010, **112**, 1842.
- 226 N. Lopez-Salas, D. Carriazo, M. C. Gutiérrez, M. L. Ferrer, C. O. Ania, F. Rubio, A. Tamayo, J. L. G. Fierro and F. Del Monte, *J. Mater. Chem. A*, 2016, **4**, 9146.
- 227 M. C. Gutiérrez, D. Carriazo, C. O. Ania, J. B. Parra, M. Luisa Ferrer and F. Del Monte, *Energy Environ. Sci.*, 2011, **4**, 3535–3544.
- 228 S. E. Lappi, B. Smith and S. Franzen, *Spectrochim acta A*, 2004, **60**, 2611–2619.
- 229 A. K. Soper, *RAL Technical Report No. RAL-TR-201*, 2011.
- 230 A. K. Soper, *Chem. Phys.*, 1996, **202**, 295.
- 231 A. K. Soper, *Mol. Phys.*, 2001, **99**, 1503–1516.
- 232 A. K. Soper, *Mol. Phys.*, 2009, **107**, 1667.
- 233 C. Hardacre, J. D. Holbrey, M. Nieuwenhuyzen and T. G. A. Youngs, *Acc. Chem. Res.*, 2007, **40**, 1146.
- 234 A. Pandey, R. Rai, M. Pal and S. Pandey, *Phys. Chem. Chem. Phys.*, 2014, **16**, 1559.

- 235 S. Imberti and D. T. Bowron, *J. Phys. Condens. Matter*, 2010, **22**, 404212.
- 236 P. Gale, T. Gunnlaugsson, V. Amendola, L. Fabbrizzi and L. Mosca, *Chem. Soc. Rev.*, 2010, **39**, 3889.
- 237 V. Amendola, D. Esteban-go, Ä. Mez, L. Fabbrizzi, M. Licchelli and C. Generale, *Acc. Chem. Res.*, 2006, **39**, 343.
- 238 S. A. Blair and A. J. Thakkar, *Chem. Phys. Lett.*, 2010, **495**, 198–202.
- 239 O. S. Hammond, D. T. Bowron and K. J. Edler, *Angew. Chem - Int. Ed.*, 2017, **56**, 9782.
- 240 E. C. Gruen and R. A. Plane, *Inorg. Chem.*, 1967, **6**, 1123.
- 241 D. Chen, Q. Tang, X. Li, X. Zhou, J. Zang, W. Xue, J. Xiang and C. Guo, *Int. J. Nanomedicine*, 2012, **7**, 4973.
- 242 R. G. Pearson, *J. Chem. Educ.*, 1968, **45**, 581.
- 243 J. Miller, A. D. McLachlan and A. Klug, *EMBO J.*, 1985, **4**, 1609–1614.
- 244 Y. Hou, Y. Gu, S. Zhang, F. Yang, H. Ding and Y. Shan, *J. Mol. Liq.*, 2008, **143**, 154–159.
- 245 D. Paliwoda, K. F. Dziubek and A. Katrusiak, *Cryst. growth Des.*, 2012, **12**, 10.
- 246 D. A. Alonso, A. Baeza, R. Chinchilla, G. Guillena, I. M. Pastor and D. J. Ramón, *European J. Org. Chem.*, 2016, 612–632.
- 247 S. Golde, T. Palberg and H. J. Schöpe, *Nat. Phys.*, 2016, **12**, 712.
- 248 R. Williams, *Res. psu.edu/brpgroup/pKa_compilation.pdf*, 2011.
- 249 T. Sato and M. Yamatake, *J. Inorg. Nucl. Chem.*, 1969, **31**, 3633–3642.
- 250 T. Sato, T. Nishida and M. Yamatake, *J. Appl. Chem. Biotechnol.*, 1973, **23**, 909–917.
- 251 J. M. Warden and C. J. King, *J. Chem. Eng. Data*, 1978, **23**, 144.
- 252 D. Parmentier, S. J. Metz and M. C. Kroon, *Green Chem.*, 2012, 205–209.
- 253 J. G. Huddleston, H. D. Willauer, R. P. Swatloski, A. E. Visser and R. D. Rogers, *Chem. Commun.*, 1998, 1765–1766.
- 254 J. G. Huddleston, W. M. Reichert, H. D. Willauer, G. A. Broker and R. D. Rogers, *Green Chem.*, 2001, **3**, 156.
- 255 D. J. G. P. van Osch, D. Parmentier, C. H. J. . Dietz, A. van den Bruinhorst, R. Tuiner and Kroon, *Chem. Commun.*, 2016, **52**, 11987–11990.
- 256 J. Cao, M. Yang, F. Cao, J. Wang and E. Su, *ACS Sustain. Chem. Eng.*, 2017, **5**, 3270–3278.
- 257 J. Cao, L. Chen, M. Li, F. Cao, L. Zhao and E. Su, *Green Chem.*, 2018, **20**, 1879.
- 258 A. R. Martins, E. A. Crespo, P. V. A. Pontes, L. P. Silva, M. Bu, G. J. Maximo, E. A. C. Batista and C. Held, *ACS Sustain. Chem. Eng.*, 2018, **6**, 8836–8846.

- 259 C. Florindo, L. Romero, I. Rintoul, C. Branco and I. M. Marrucho, *ACS Sustain. Chem. Eng.*, 2018, **6**, 3888–3895.
- 260 K. J. Fraser and D. R. MacFarlane, *Aust. J. Chem.*, 2009, **62**, 309–321.
- 261 T. Cassagneau, T. E. Mallouk, J. H. Fendler, V. Uni, U. V Park, V. Pennsylv, V. Ad, M. Processing, C. U. V, P. O. Box and N. York, *J. Am. Chem. Soc.*, 1998, **120**, 7848–7859.
- 262 I. Mekis, D. V Talapin, A. Kornowski, M. Haase and H. Weller, *J. Phys. Chem.*, 2003, **107**, 7454–7462.
- 263 T. Trindade, P. O'Brien and X. Zhang, *Chem. Mater.*, 1997, **9**, 523–530.
- 264 F. V Mikulec, M. Kuno, M. Bennati, D. A. Hall, R. G. Griffin and M. G. Bawendi, *J. Am. Ceram. Soc.*, 2000, **122**, 2532–2540.
- 265 A. A. Guzelian, J. E. B. Katari, A. V Kadavanich, U. Banin, K. Hamad, E. Juban, A. P. Alivisatos, R. H. Wolters, C. C. Arnold and J. R. Heath, *J. Phys. Chem.*, 1996, **100**, 7212–7219.
- 266 E. K. Watson and W. A. Rickelton, *Solvent Extr. Ion Exch.*, 1992, **10**, 37–41.
- 267 P. O. Saboe, L. P. Manker, W. E. Michener, D. J. Peterson, D. G. Brandner, S. P. Deutch, M. Kumar, R. M. Cywar, G. T. Beckham and E. M. Karp, *Green Chem.*, 2018, **20**, 1791.
- 268 M. Matsumoto, S. Uenoyama, T. Hano, M. Hirata and S. Miura, *J. Chem. Technol. Biotechnol.*, 1996, **67**, 260–264.
- 269 T. Brouwer, M. Blahusiak, K. Babic and B. Schuur, *Sep. Purif. Technol.*, 2017, **185**, 186–195.
- 270 G. Kim, S. Park and B. Um, *Ind. Crop. Prod.*, 2016, **89**, 34–44.
- 271 P. Praveen and K. Loh, *Chemosphere*, 2016, **153**, 405–413.
- 272 E. K. Watson, W. A. Rickelton, A. J. Robertson and T. J. Brown, *Solvent Extr. Ion Exch.*, 1988, **6**, 207–220.
- 273 P. Praveen and K. Loh, *J. Memb. Sci.*, 2013, **437**, 1–6.
- 274 Cytec Industries Inc., *Cytec Ind. Inc.*, 2008, 16.
- 275 S. Biswas, P. N. Pathak and S. B. Roy, *Spectrochim. Acta - Part A Mol. Biomol. Spectrosc.*, 2012, **91**, 222–227.
- 276 P. Praveen and K. Loh, *Chem. Eng. J.*, 2014, **255**, 641–649.
- 277 F. H. Rhodes and A. L. Markley, *J. Phys. Chem.*, 1920, **25**, 527–534.
- 278 J. B. Ferguson, *J. Phys. Chem.*, 1927, **31**, 757.
- 279 J. M. Chem, V. Armel, D. Velayutham, J. Sun, P. C. Howlett, M. Forsyth, D. R. Macfarlane and J. M. Pringle, *J. Mater. Chem.*, 2011, **21**, 7640–7650.
- 280 S. Forsyth, J. Golding, D. R. Macfarlane and M. Forsyth, *Electrochim. Acta*, 2001,

- 46**, 1753–1757.
- 281 J. D. Holbrey, W. M. Reichert, R. P. Swatloski, G. A. Broker, W. R. Pitner, K. R. Seddon and R. D. Rogers, *Green Chem.*, 2002, **4**, 407–413.
- 282 C. R. Hilliard, N. Bhuvanesh, J. A. Gladysz and J. Bl, *Dalt. Trans.*, 2012, **41**, 1742.
- 283 E. Y. Tupikina, M. Bodensteiner, P. M. Tolstoy, G. S. Denisov and I. G. Shenderovich, *J. Phys. Chem. C*, 2018, **122**, 1711.
- 284 <https://www.sigmaaldrich.com/catalog/product/aldrich/223301?lang=en®ion=GB>, Date accessed: 02/09/2019.
- 285 E. Makrl, J. Budka and P. Van, *J. Phys. Chem. A*, 2009, **113**, 5896.
- 286 C. Ruß and B. König, *Green Chem.*, 2012, **14**, 2969–2982.
- 287 J. C. Mauro, Y. Yue, A. J. Ellison, P. K. Gupta and D. C. Allan, *PNAS*, 2009, **106**, 19780.
- 288 G. Ghersini, in *Extraction chromatography*, eds. T. Braun and G. Ghersini, Elsevier, 1975, pp. 68–129.
- 289 G. . Southworth and J. . Keller, *Water, Air Soil Pollut.*, 1986, **28**, 239.
- 290 E. Alkaya, S. Kaptan, L. Ozkan, S. Uludag-demirer and G. N. Demirer, *Chemosphere*, 2009, **77**, 1137–1142.
- 291 N. Schaeffer and A. R. Martins, *Chem. Commun.*, 2018, **54**, 8104–8107.
- 292 C. Bayliss and K. Langley, *Nuclear Decommissioning, Waste Management, and Environmental Site Remediation*, Elsevier, 2003.
- 293 W. Jianchen and S. Chongli, *Solvent Extr. Ion Exch.*, 2001, **19**, 231–242.
- 294 M. Krea and H. Khalaf, *Hydrometallurgy*, 2000, **58**, 215–225.
- 295 A. Rout and K. Binnemans, *Dalt. Trans.*, 2015, **44**, 1379–1387.
- 296 L. Yuan, M. Sun, X. Liao, Y. Zhao, Z. Chai and W. Shi, *Sci. China Chem.*, 2014, **57**, 1432–1438.
- 297 V. A. Cocalia, M. P. Jensen, J. D. Holbrey, S. K. Spear, D. C. Stepinski and R. D. Rogers, *Dalton Trans.*, 2005, 4–9.
- 298 P. S. Barber, S. P. Kelley and R. D. Rogers, *RSC Adv.*, 2012, **2**, 8526–8530.
- 299 C. Gaillard, M. Boltoeva, I. Billard, D. S. Georg and A. Ouadi, *RSC Adv.*, 2016, **6**, 70141–70151.
- 300 D. R. Prabhu, P. K. Mohapatra, D. R. Raut and I. Billard, *Solvent Extr. Ion Exch.*, 2017, **35**, 423–438.
- 301 R. Babecki, A. W. . Platt and J. C. Tebby John, *Polyhedron*, 1989, **8**, 1357–1360.
- 302 F. Pinaud, D. King, H. Moore and S. Weiss, *J. Am. Chem. Soc.*, 2004, **126**, 6115–6123.
- 303 Sigma Aldrich Chemical SDS, <https://www.sigmaaldrich.com/saftey-center.html>,

Date accessed: 02/05/2019.

- 304 J. Wardell and C. King, *J. Chem. Eng. Data*, 1978, **23**, 144–148.
- 305 H. Babich and D. L. Davis, *Regul. Toxicol. Pharmacol.*, 1981, **1**, 90.
- 306 L. Xiao, S. Wang, H. Li, Z. Li, Z. Shi, L. Xiao, R. Sun, Y. Fang and G. Song, *ACS Catal.*, 2017, **7**, 7535–7542.
- 307 Y. Liu and R. Naidu, *Waste Manag.*, 2014, **34**, 2662–2673.
- 308 R. Zhang, S. Zheng, S. Ma and Y. Zhang, *J. Hazard. Mater.*, 2011, **189**, 827–835.
- 309 M. T. Ochsenku, K. S. Hatzilyberis, L. N. Mendrinis and C. E. Salmas, *Ind. Eng. Chem. Res.*, 2002, **41**, 5794–5801.
- 310 R. A. Abdulvaliyev, A. Akcil, S. V. Gladyshev, E. A. Tastanov, K. O. Beisembekova, N. K. Akhmadiyeva and H. Deveci, *Hydrometallurgy*, 2015, **157**, 72–77.
- 311 J. Obhodas, D. Sudac, L. Matjacic and V. Valkovic, *2011 2nd Int. Conf. Adv. Nucl. Instrumentation, Meas. Methods their Appl.*, 2011, **59**, 1–5.
- 312 B. Kutchko and A. Kim, *Fuel*, 2006, **85**, 2537–2544.
- 313 N. K. Koukoulas, R. Zeng, V. Perdikatsis, W. Xu and E. K. Kakaras, *Fuel*, 2006, **85**, 2301–2309.
- 314 N. Moreno, X. Querol, J. Andres, K. Stanton, M. Towler, H. Nugteren, M. Janssen-Jurkovicova and R. Jones, *Fuel*, 2005, **84**, 1351–1363.
- 315 F. Zheng, Z. Fang and H. D. Gesser, *Hydrometallurgy*, 1996, **41**, 187–200.
- 316 W. S. Seames, *Fuel Process. Technol.*, 2003, **81**, 109–125.
- 317 Y. Liu, C. Lin and Y. Wu, *J. Hazard. Mater.*, 2007, **146**, 255–261.
- 318 H. Sutar, S. C. Mishra, S. K. Sahoo, A. Prasad and H. S. Maharana, *Am. Chem. Sci. J.*, 2014, **4**, 255–279.

8 APPENDIX 1

8.1 Engineering wastes

8.1.1 Red mud

Red mud is the waste material produced from processing of aluminium ore (bauxite) during the Bayer process. The raw ore is mixed with a sodium hydroxide solution and heated, dissolving the aluminium silicate³⁰⁷ the remaining undissolved alumina-silicate matrices along with other metal oxides are the main components of red mud.³⁰⁸ The addition of the basic sodium hydroxide leaves the red mud with a high pH of around 12.³⁰⁹ This high pH and insoluble nature of red mud makes it expensive to store and a potential environmental hazard. Currently around 120 million tonnes of red mud are produced annually with a global inventory around 3 Billion tonnes.³¹⁰ Characterisation of different samples of red mud has shown that it contains between 60-90 mg/kg of gallium³⁰⁷ and around 6.2% w/w SiO₂.³¹¹ The high concentration of valuable resources present in the red mud and with the vast quantities of red mud globally make this waste stream a valuable source of materials.

8.1.2 Coal fly ash

Coal fly ash is the waste by-product from the combustion of coal used to produce electricity. Annually in the USA alone 100 million tonnes of fly ash was produced³¹² and around 160million tonnes in China.³¹³ This is a large source of waste that, again, has potential to be a valuable resource. Similarly, to red mud the fly ash is also reasonably basic due to the presence of CaO which is converted into Ca(OH)₂ when in solution. Therefore, disposing the waste once again poses a challenge. Coal fly ash contains 192-268 g/kg of Si predominantly in the form of amorphous SiO₂.³¹² The level of Ga reported in fly ash samples however vary greatly from under 1 µg/g³¹⁴ to 230 µg/g,¹⁹⁰ therefore the raw source of the fly ash largely influences the quantity of gallium present. An interesting observation with fly ash is that gallium concentration increases as the particle size of the fly ash decreases, an explanation for this has been put forward stating that it is likely due to the gallium being vaporised during the combustion of coal and then condensing on the surface of the fly ash³¹⁵ therefore an increase in surface area would lead to an increase in Ga concentration.

8.2 Scanning electron microscopy for PFA and red mud samples

Scanning electron microscopy was used to characterise the surface of the red mud and PFA pre- and post- treatment with 1:2 ChCl:Ur DES.

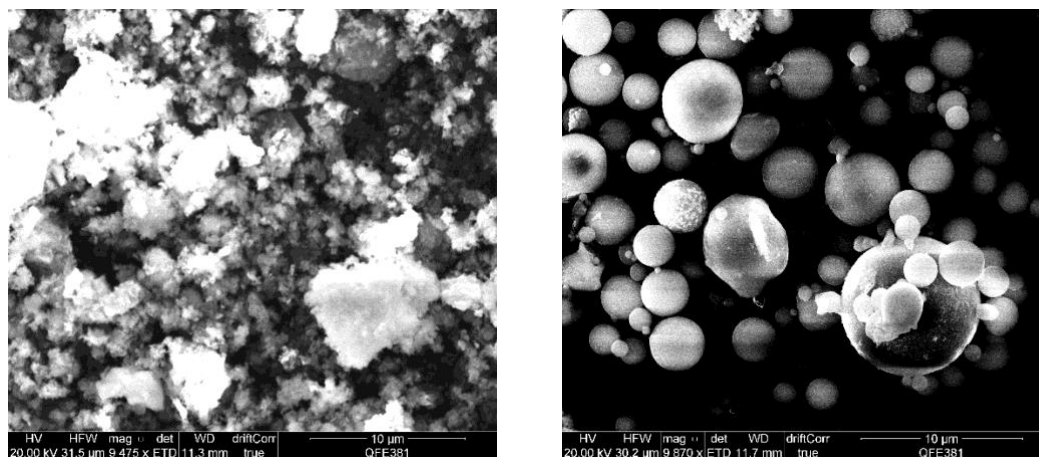


Figure 8.2-1: SEM image of red mud (left) and PFA (right)

Upon magnification of PFA samples it was observed that spherical particulates³¹² were present, ranging in different sizes from under 1 micron to 9 microns (). The specific spherical shape adopted by PFA is due to the high temperatures that the sample is subjected to during the combustion of coal.³¹⁶ The temperatures reached are high enough to liquefy the sample and upon cooling the droplet shape is adopted. At higher magnification, abrasions on the surface of PFA indicate that pressure may have been applied to the sample.

SEM images of pre-treatment red mud samples revealed that it has an amorphous shape(Figure 8.2-1),³¹⁷ it has not been expose to the high temperature process which causes liquefaction of the PFA and upon cooling the formation of the samples distinct shape.

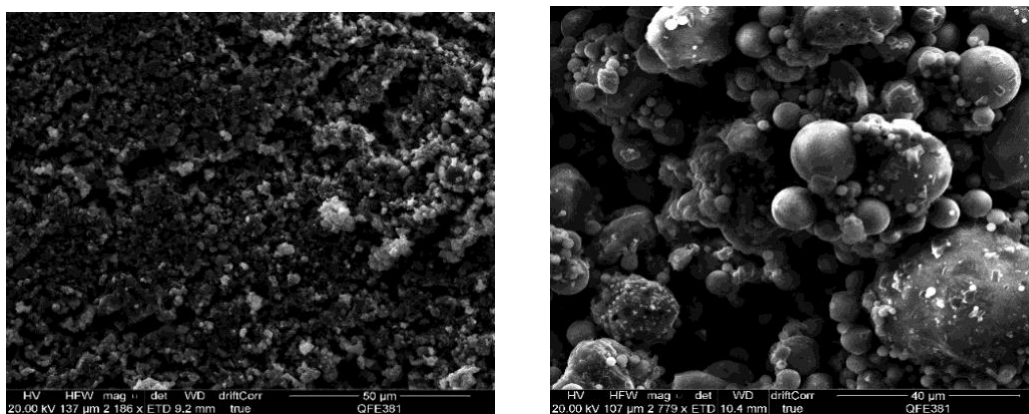


Figure 8.2-2: Scanning electron microscopy image of pulverised fly ash (left) and red mud (right) after treatment with 1:2 choline chloride:Ur.

Post-treatment samples of both wastes were studied with samples being mixed with 1:2 ChCl:Ur DES for 18hrs. They were washed in methanol to remove DES and left to dry. The images shown in Figure 8.2-2 revealed that the spheres present in the pre-treated samples of PFA had lost their shape and in places there were signs of fusion between the spheres. This indicates that the DES has interacted with the PFA and caused the structure to become destabilised, possibly due to the dissolution of a metal oxide within the framework.

8.3 Treatment of engineering wastes using DES

An experiment was conducted to examine the chemical interaction between a common deep eutectic solvent and waste samples. Red mud₃₁₈ and PFA₃₁₃ samples were introduced in to a 1:2 ChCl:Ur deep eutectic solvent and reacted overnight at 80 °C.

After the sample had been worked-up to remove any undissolved matter, a visual observation of colour was recorded for the 1:2 ChCl:Ur with dissolved metal oxides. The DES reacted with red mud remained colourless; in contrast the DES reacted with PFA changed from colourless to a red colour. ICP-MS was conducted on the PFA/DES sample to determine the type of oxides dissolved into the DES along with the extraction %.

Table 8.3-1: showing the relative % difference in amount of each metal present in the sample with respect to Al between the pulverised fly ash sample and the post treatment 1:2 ChCl Ur sample. % dissolved for each element present in the PFA sample.

Element	Relative % difference	% dissolved
Al	0.0	0.50
As	0.3	1.49
B	1.0	0.75
Ba	0.4	0.97
Ca	1090.5	11.88
Cd	0.3	3.12
Co	0.5	3.12
Cr	0.8	4.47
Cu	2.5	9.06
Fe	72.9	1.22
Mg	40.6	1.43
Mn	4.3	3.97
Ni	0.5	3.12
P	18.3	2.50
Pb	0.1	0.97
Sb	0.2	3.12
Se	0.4	3.12
Si	37.7	1.47
Sn	0.2	3.12
Sr	2.2	2.33
Ti	1.6	0.92
V	3.4	5.28
Zn	0.6	1.98

Table 8.3-1 shows the relative difference of an element present with respect aluminium to pre- and post-treatment was determined as a percentage by calculating the number of moles of each element present in the sample dividing this value by the amount of aluminium present and multiplying the value by 100. The values for pre-treatment were then subtracted from the values for post-treatment. This gave an idea of the selectivity that the solvent possesses for specific metal oxides. The solvent was highly selective towards calcium, it being over 1000% more selective towards the Ca as opposed to Al notwithstanding the greater quantity of Al present in the starting material. Iron was also found to be reasonably selective with an increase of 70% against the Aluminium.

The % dissolved for metal oxides in the 1:2 ChCl: Ur was also calculated, again Ca was found to be the best performing element with a dissolved % value of 12% followed by Cu of

which around 9% had dissolved into the deep eutectic solvent. The worst performing element was the Al with only 0.5% being dissolved into the solvent, this property may be a useful one as dissolving more valuable metals selectively over Al would mean that most of the sample would remain undissolved and allow for more simple extraction of these precious metals as the Al which made up the bulk of the samples was no longer present.

While the dissolution selectivity for specific metal oxides such as Ca was extremely high using 1:2 Ch:Ur, the values generated for overall % dissolution were all less than 13%. The work conducted provides more evidence that deep eutectic solvents have the ability to dissolve metal oxides but highlights the importance of selecting the appropriate DES to carry out selective high yielding separations and extractions. Looking to progress on this initial finding, DES will be selected where one of the components in the solvent has previously shown the potential for metal dissolution. Attempting to maintain the high selectivity for particular metal oxides that was shown in the 1:2 ChCl:Ur system, whilst obtaining higher yields for the metal extraction.

9 APPENDIX 2

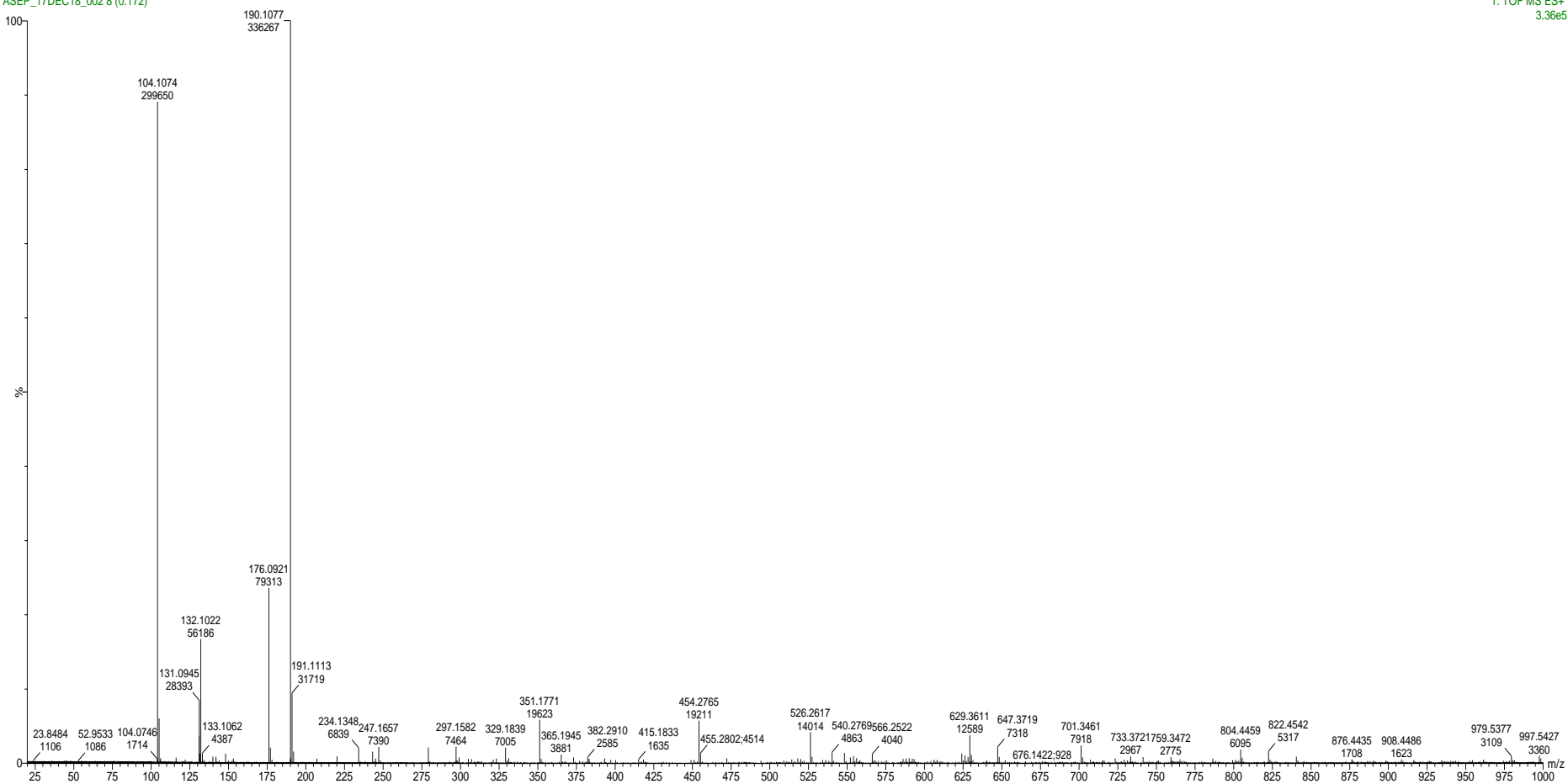
ESI(+)-MS of ChCl:Ox with dissolved ZnO

MWG-ZnOxChCl

ASEP_17DEC18_002 8 (0.172)

1: TOF MS ES+

3.36e5



ESI(-)-MS of ChCl:Ox with dissolved ZnO

